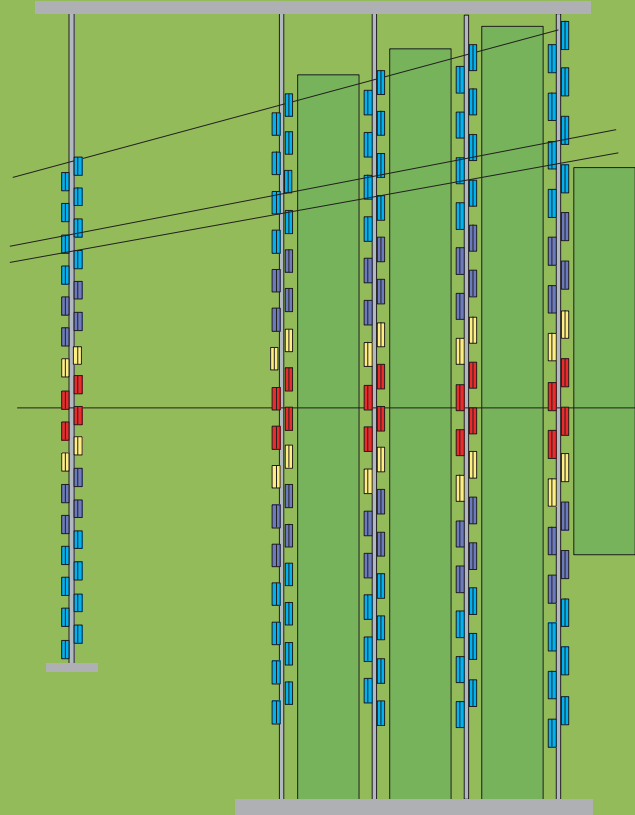


LHCb Muon System



Technical Design Report

LHCb

Muon System Technical Design Report

Printed at CERN
Geneva, 2001
ISBN 92-9083-180-4

The LHCb Collaboration¹

Brasilian Center for particles physics, CBPF, Rio de Janeiro, Brasil

P.R.Barbosa Marinho, I.Bediaga, G.Cernicchiaro, A.França Barbosa, J.Magnin, J.Marques de Miranda, A.Massafferri, A.Reis, R.Silva

University of Rio de Janeiro, UFRJ, Rio de Janeiro, Brasil

S.Amato, P.Colrain, T.da Silva, J.R.T.de Mello Neto, L.de Paula, M.Gandelman, J.H.Lopes, B.Marechal, D.Moraes, E.Polycarpo

University of Clermont-Ferrand II, Clermont-Ferrand, France

Z.Ajaltouni, G.Bohner, V.Breton, R.Cornat, O.Deschamps, A.Falvard¹⁾, P.Henrard, J.Lecoq, P.Perret, C.Rimbault, C.Trouilleau, A.Ziad

CPPM Marseille, Aix University-Marseille II, Marseille, France

E.Aslanides, J.P.Cachemiche, R.Le Gac, O.Leroy, P.L.Liotard, M.Menouni, R.Potheau, A.Tsaregorodtsev, B.Viaud

University of Paris-Sud, LAL Orsay, Orsay, France

G.Barrand, C.Beigbeder-Beau, D.Breton, T.Caceres, O.Callot, Ph.Cros, B.D'Almagne, B.Delcourt, F.Fulda Quenzer, A.Jacholkowska¹⁾, B.Jean-Marie, J.Lefrançois, F.Machefert, V.Tocut, K.Truong, I.Videau

Technical University of Dresden, Dresden, Germany

R.Schwierz, B.Spaan

Max-Planck-Institute for Nuclear Physics, Heidelberg, Germany

C.Bauer, D.Baumeister, N.Bulian, H.P.Fuchs, T.Glebe, W.Hofmann, K.T.Knöpfle, S.Löchner, M.Schmelling, B.Schwingenheuer, F.Sciacca, E.Sexauer²⁾, U.Trunk

Physics Institute, University of Heidelberg, Heidelberg, Germany

S.Bachmann, P.Bock, H.Deppe, F.Eisele, M.Feuerstack-Raible, S.Henneberger, P.Igo-Kemenes, R.Rusnyak, U.Stange, M.Walter, D.Wiedner, U.Uwer

Kirchhoff Institute for Physics, University of Heidelberg, Heidelberg, Germany

V.Lindenstruth, R.Richter, M.W.Schulz, A.Walsch

Laboratori Nazionali dell'INFN, Frascati, Italy

M.Anelli, G.Bencivenni, C.Bloise, F.Bossi, P.Campana, G.Capon, P.DeSimone, C.Forti, A.Franceschi, F.Murtas, L.Passalacqua, V.Patera(1), A.Saputi, A.Sciubba(1)

(1) also at Dipartimento di Energetica, University of Rome, "La Sapienza"

University of Bologna and INFN, Bologna, Italy

M.Bargiotti, A.Bertin, M.Bruschi, M.Capponi, I.D'Antone, S.de Castro, P.Faccioli, L.Fabbri, D.Galli, B.Giacobbe, U.Marconi, I.Massa, M.Piccinini, M.Poli, N.Semprini-Cesari, R.Spighi, V.Vagnoni, S.Vecchi, M.Villa, A.Vitale, A.Zoccoli

¹This list includes additional colleagues who made particular contributions to the work presented in this TDR.

University of Cagliari and INFN, Cagliari, Italy

S.Cadeddu, A.Cardini, M.Caria, A.Lai, D.Marras, D.Pinci, B.Saitta(1)

(1) also at CERN

University of Ferrara and INFN, Ferrara, Italy

V.Carassiti, A.Cotta Ramusino, P.Dalpiaz, F.Evangelisti, A.Gianoli, R.Malaguti, M.Martini, F.Petrucci, M.Savrié

University of Florence and INFN, Florence, Italy

A.Bizzeti, M.Calvetti, G.Collazuol, E.Iacopini, G.Passaleva, M.Veltri

University of Genoa and INFN, Genoa, Italy

S.Cuneo, F.Fontanelli, V.Gracco, P.Musico, A.Petrolini, M.Sannino

University of Milano-Bicocca and INFN, Milano, Italy

M.Alemi, T.Bellunato(1), M.Calvi, C.Matteuzzi, M.Musy, P.Negri, M.Paganoni

(1) also at CERN

University of Rome, “La Sapienza” and INFN, Rome, Italy

G.Auriemma(1), L.Benussi, V.Bocci, C.Bosio, G.Chiodi, D.Fidanza(1), A.Frenkel, K.Harrison, I.Kreslo, S.Mari(1), G.Martellotti, S.Martinez, G.Penso, G.Pirozzi(1), R.Santacesaria, C.Satriano(1), A.Satta

(1) also at Università della Basilicata, Potenza

University of Rome, “Tor Vergata” and INFN, Rome, Italy

G.Carboni, D.Domenici, G.Ganis, M.Gatta, R.Messi, L.Pacciani, L.Paoluzi, E.Santovetti

NIKHEF, The Netherlands

G.van Apeldoorn(1,3), N.van Bakel(1,2), T.S.Bauer(1,4), J.van den Brand(1,2), H.J.Bulten(1,2), M.Doets(1), R.van der Eijk(1), I.Gouz(1,5), V.Gromov(1), R.Hierck(1), L.Hommels(1), E.Jans(1), T.Ketel(1,2), S.Klous (1,2), B.Koene(1), M.Merk(1), M.Needham(1), H.Schuijlenburg(1), T.Sluijk(1), J.van Tilburg(1), H.de Vries(1), L.Wiggers(1)

(1) Foundation of Fundamental Research of Matter in the Netherlands,

(2) Free University Amsterdam,

(3) University of Amsterdam,

(4) University of Utrecht,

(5) on leave from Protvino

Institute of High Energy Physics, Beijing, P.R.C.

C.Gao, C.Jiang, H.Sun, Z.Zhu

Research Centre of High Energy Physics, Tsinghua University, Beijing, P.R.C.

M.Bisset, J.P.Cheng, Y.G.Cui, Y.Gao, H.J.He, Y.P.Kuang, Y.J.Li, Q.Li, Y.Liao, J.P.Ni, B.B.Shao, J.J.Su, Y.R.Tian, Q.Wang, Q.S.Yan

Institute for Nuclear Physics and University of Mining and Metalurgy, Krakow, Poland

E.Banas, J.Blocki, K.Galuska, L.Hajduk, P.Jalocha, P.Kapusta, B.Kisielewski, W.Kucewicz, T.Lesiak, J.Michalowski, B.Muryn, Z.Natkaniec, W.Ostrowicz, G.Polok, E.Rulikowska-Zarebska, M.Stodulski, M.Witek, P.Zychowski

Soltan Institute for Nuclear Physics, Warsaw, Poland

M.Adamus, A.Chlopik, Z.Guzik, A.Nawrot, M.Szczekowski

Horia Hulubei-National Institute for Physics and Nuclear Engineering (IFIN-HH), Bucharest-Magurele, Romania

D.V.Anghel³⁾, C.Coca, A.Cimpean, G.Giolu, C.Magureanu, S.Popescu, T.Preda, A.M.Rosca(1), V.L.Rusu⁴⁾

(1) also at Humbolt University, Berlin

Institute for Nuclear Research (INR), Moscow, Russia

V.Bolotov, S.Filippov, J.Gavrilov, E.Guschin, V.Kloubov, L.Kravchuk, S.Laptev, V.Laptev, V.Postoev, A.Sadovskii, I.Semenioui

Institute of Theoretical and Experimental Physics (ITEP), Moscow, Russia

S.Barsuk, I.Belyaev, A.Golutvin, O.Gouchtchine, V.Kiritchenko, G.Kostina, N.Levitski, A.Morozov, P.Pakhlov, D.Roussinov, V.Rusinov, S.Semenov, A.Soldatov, E.Tarkovski

Budker Institute for Nuclear Physics (INP), Novosibirsk, Russia

K.Beloborodov, A.Bondar, A.Bozhenok, A.Buzulutskov, S.Eidelman, V.Golubev, S.Oreshkin, A.Poluektov, S.Serednyakov, L.Shekhtman, B.Shwartz, Z.Silagadze, A.Sokolov, A.Vasiljev

Institute for High Energy Physics (IHEP-Serpukhov), Protvino, Russia

L.A.Afanassieva, I.V.Ajinenko, K.Beloous, V.Brekhovskikh, S.Denissov, A.V.Dorokhov, R.I.Dzhelyadin, A.Kobelev, A.K.Konoplyannikov, A.K.Likhoded, V.D.Matveev, V.Novikov, V.F.Obratsov, A.P.Ostankov, V.I.Rykalin, V.K.Semenov, M.M.Shapkin, N.Smirnov, A.Sokolov, M.M.Soldatov, V.V.Talanov, O.P.Yushchenko

Petersburg Nuclear Physics Institute, Gatchina, St.Petersburg, Russia

M.Borkovsky, B.Botchine, S.Guetz, V.Lazarev, N.Saguidova, E.Spiridenkov, I.Velitchko, A.Vorobyov, An.Vorobyov

University of Barcelona, Barcelona, Spain

R.Ballabriga(1), S.Ferragut, Ll.Garrido, D.Gascon, S.Luengo(1), R.Miquel⁵⁾, D.Peralta, M.Rosello(1), X.Vilasis(1)

(1) also at departament d'Engineria Electronica La Salle, Universitat Ramon Llull, Barcelona

University of Santiago de Compostela, Santiago de Compostela, Spain

B.Adeva, P.Conde, F.Gomez, J.A.Hernando, A.Iglesias, A.Lopez-Aguera, A.Pazos, M.Plo, J.M.Rodriguez, J.J.Saborido, M.J.Tobar

University of Lausanne, Lausanne, Switzerland

P.Bartalini, A.Bay, B.Carron, C.Currat, O.Dormond, F.Dürrenmatt, Y.Ermoline, R.Frei, G.Gagliardi, G.Haefeli, J.P.Hertig, P.Koppenburg, T.Nakada(1), J.P.Perroud, F.Ronga, O.Schneider, L.Studer, M.Tareb, M.T.Tran

(1) also at CERN, on leave from PSI, Villigen

University of Zürich, Zürich, Switzerland

R.Bernet, E.Holzschuh, P.Sievers, O.Steinkamp, U.Straumann, D.Wyler, M.Ziegler

Institute of Physics and Technologies, Kharkiv, Ukraine

S.Maznichenko, O.Omelaenko, Yu.Ranyuk

Institute for Nuclear Research, Kiev, Ukraine

V.Aushev, V.Kiva, I.Kolomiets, Yu.Pavlenko, V.Pugatch, Yu.Vasiliev, V.Zerkin

University of Bristol, Bristol, U.K.

N.H.Brook, J.E.Cole, R.D.Head, A.Phillips, F.F.Wilson

University of Cambridge, Cambridge, U.K.

K.George, V.Gibson, C.R.Jones, S.G.Katvars, C.Shepherd-Themistocleous, C.P.Ward, S.A.Wotton

Rutherford Appleton Laboratory, Chilton, U.K.

C.A.J.Brew, C.J.Densham, S.Easo, B.Franek, J.G.V.Guy, R.N.J.Halsall, J.A.Lidbury, J.V.Morris, A.Papanestis, G.N.Patrick, F.J.P.Soler, S.A.Temple, M.L.Woodward

University of Edinburgh, Edinburgh, U.K.

S.Eisenhardt, A.Khan, F.Muheim, S.Playfer, A.Walker

University of Glasgow, Glasgow, U.K.

A.J.Flavell, A.Halley, V.O'Shea, F.J.P.Soler

University of Liverpool, Liverpool, U.K.

S.Biagi, T.Bowcock, R.Gamet, P.Hayman, M.McCubbin, C.Parkes, G.Patel, S.Walsh, V.Wright

Imperial College, London, U.K.

G.J.Barber, D.Clark, P.Dauncey, A.Duane, M.Girone(1), J.Hassard, R.Hill, M.J.John⁶⁾, D.R.Price, P.Savage, B.Simmons, L.Toudup, D.Websdale

(1) also at CERN

University of Oxford, Oxford, U.K

M.Adinolfi, G.Damerell, J.Bibby, M.J.Charles, N.Harnew, F.Harris, I.McArthur, J.Rademacker, N.J.Smale, S.Topp-Jorgensen, G.Wilkinson

CERN, Geneva, Switzerland

J.André, F.Anghinolfi, F.Bal, M.Benayoun(1), W.Bonivento(2), A.Braem, J.Buytaert, M.Campbell, A.Cass, M.Cattaneo, E.Chesi, J.Christiansen, R.Chytracsek⁷⁾, J.Closier, P.Collins, G.Corti, C.D'Ambrosio, H.Dijkstra, J.P.Dufey, M.Ferro-Luzzi, F.Fiedler, W.Flegel, F.Formenti, R.Forty, M.Frank, C.Frei, I.Garcia Alfonso, C.Gaspar, G.Gracia Abril, T.Gys, F.Hahn, S.Haider, J.Harvey, B.Hay⁸⁾, E.van Herwijnen, H.J.Hilke, G.von Holtey, D.Hutchcroft, R.Jacobsson, P.Jarron, C.Joram, B.Jost, A.Kashchuk(3), I.Korolko(4), R.Kristic, D.Lacarrère, M.Laub, M.Letheren, J.F.Libby, R.Lindner, C.Lippmann, M.Losasso, P.Mato Vila, H.Müller, N.Neufeld, J.Ocariz⁹⁾, S.Ponce, F.Ranjard, W.Riegler, F.Rohner, T.Ruf, S.Schmeling, B.Schmidt, T.Schneider, A.Schopper, W.Snoeys, V.Souvorov(3),

W.Teyssey, F.Teubert, J.Toledo Alarcon, O.Ullaland, A.Valassi, P.Vazquez Regueiro, F.Vinci do Santos(5), P.Wertelaers, A.Wright¹⁰⁾, K.Wyllie

- (1) on leave from Université de Paris VI et VII (LPNHE), Paris
- (2) on leave from INFN Cagliari, Cagliari
- (3) on leave from PNPI Gatchina, St.Petersburg
- (4) on leave from ITEP, Moscow
- (5) on leave from UFRJ, Rio de Janeiro

- ¹⁾ now at Groupe d’Astroparticules de Montpellier (GAM), Montpellier, France
- ²⁾ now at Dialog Semiconductor, Kirchheim-Nabern, Germany
- ³⁾ now at Oslo University, Oslo, Norway
- ⁴⁾ now at Pennsylvania University, Philadelphia, USA
- ⁵⁾ now at LBNL, Berkeley, USA
- ⁶⁾ now at Collège de France, Paris, France
- ⁷⁾ now at IT Division, CERN, Geneva, Switzerland
- ⁸⁾ now at SWX Swiss Exchange, Geneve, Switzerland
- ⁹⁾ now at Université de Paris VI et VII (LPNHE), Paris, France
- ¹⁰⁾ now at Lancaster University, Lancaster, UK

Acknowledgements

The LHCb Muon group would like to express its gratitude to many people, at CERN and in the home institutes, who have participated at various stages to the design, testing and prototype activities presented in this report. We are aware that the successful construction and commissioning of the LHCb muon system will also in the future depend on their skills and commitment.

We would like to thank A.Mazzari, V.Brunner, M.Grygiel and in particular N.Grüb for their help in the preparation of this proposal and the related LHCb Notes.

Contents

1	Introduction	1
1.1	Physics requirements	1
1.2	General detector structure	2
1.2.1	Logical layout	2
1.2.2	Physical layout	2
1.3	Evolution since the Technical Proposal	4
1.3.1	Modifications to the logical layout	4
1.3.2	Modifications to the detector technologies	4
1.4	Structure of this document	5
2	Detector Requirements and Specifications	6
2.1	Background environment	6
2.2	Muon system technologies	7
2.2.1	MWPC detectors	8
2.2.2	RPC detectors	9
2.2.3	Technology studies for the inner part of station M1	11
2.3	Electronics	11
2.4	Detector layout	12
2.4.1	Overview	12
2.4.2	Chamber arrangement	13
3	Physics Performance	16
3.1	Simulation procedure	16
3.1.1	Event generation	16
3.1.2	Tracking of particles	16
3.1.3	Background and spillover	16
3.1.4	Digitisation	18
3.1.5	Future developments	19
3.2	Level-0 muon trigger	19
3.2.1	Trigger design	19
3.2.2	Trigger performance	20
3.3	Muon identification	23
3.4	Reconstruction of muonic final states	25
3.4.1	$B_d^0 \rightarrow J/\psi (\mu^+ \mu^-) K_S^0$	25
3.4.2	$B_s^0 \rightarrow \mu^+ \mu^-$	26
3.5	Muon tagging	27
4	Prototype Studies	28
4.1	MWPC studies	28
4.1.1	Front-end electronics	28
4.1.2	Results of MWPC prototype tests	30
4.1.3	Ageing	33
4.2	RPC studies	34
4.2.1	Front-end electronics	34
4.2.2	Results of RPC prototype tests	36
4.2.3	Ageing	38

5	Technical Design	40
5.1	The MWPC detector	40
5.1.1	Detector overview and requirements	40
5.1.2	Chamber components and design	40
5.1.3	Chamber construction and tooling	43
5.1.4	HV and FE interfaces	46
5.1.5	Quality control and testing	47
5.2	The RPC detector	48
5.2.1	Detector overview and requirements	48
5.2.2	Chamber design	49
5.2.3	Chamber construction	51
5.2.4	Quality control and testing	51
5.2.5	Front-end electronics	52
5.3	Readout electronics	52
5.3.1	Overview	52
5.3.2	Front-end boards	53
5.3.3	Intermediate boards	55
5.3.4	ECS interface	55
5.3.5	Service boards	56
5.3.6	Off-Detector Electronics boards	57
5.3.7	System synchronisation	57
5.3.8	Radiation levels	59
5.3.9	Cooling of the FE-electronics	59
5.4	Service systems	59
5.4.1	Gas system	59
5.4.2	High-Voltage system	61
5.5	Chamber support structures and muon filter	62
5.5.1	Chamber support structures	64
5.5.2	Muon filter	65
5.5.3	Beam pipe shielding	67
5.6	Safety aspects	67
6	Project Organisation	68
6.1	Schedule and Milestones	68
6.1.1	Chambers	68
6.1.2	Electronics	68
6.1.3	Infrastructure	70
6.1.4	Installation and commissioning	70
6.2	Costs	70
6.3	Division of responsibilities	70

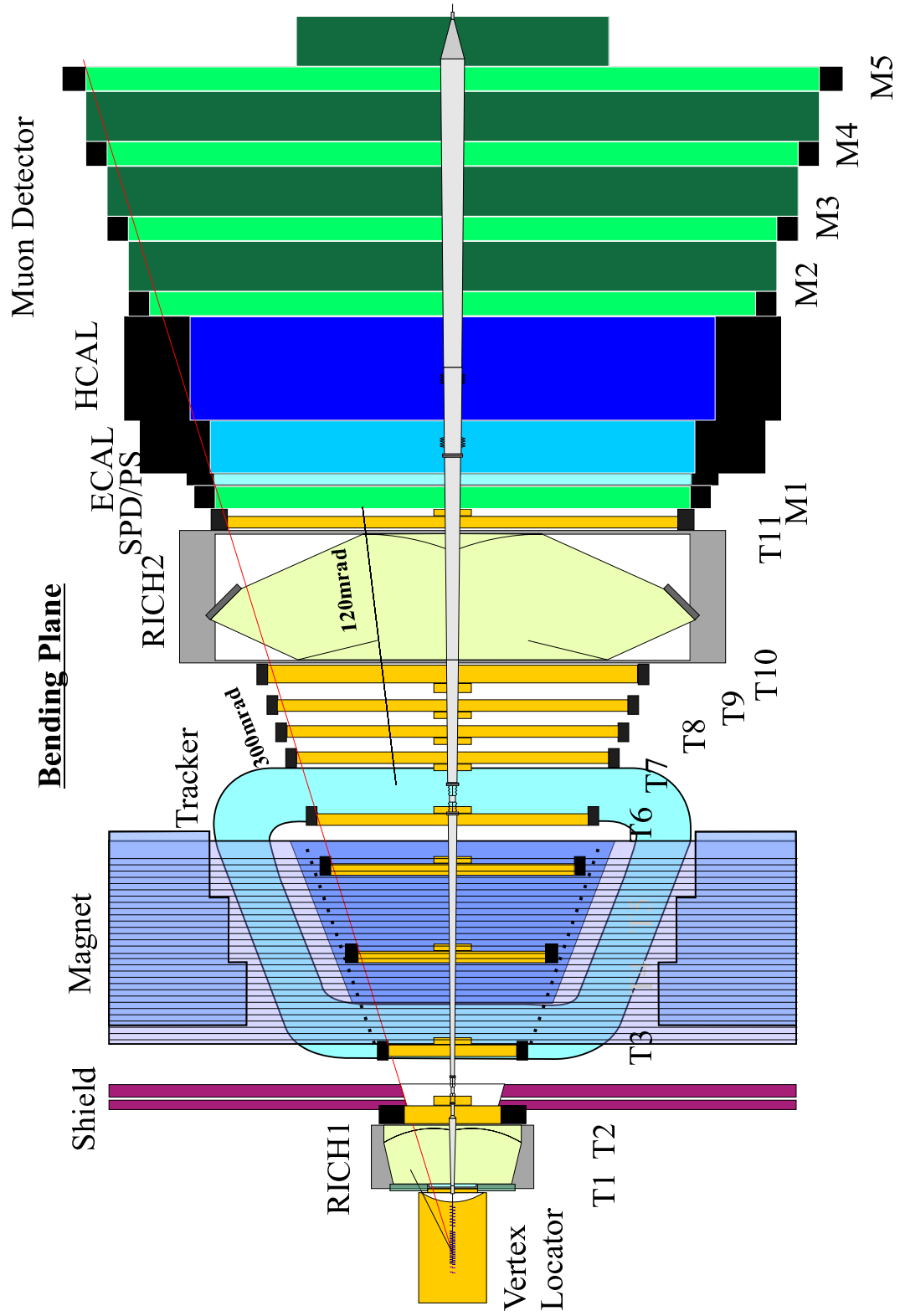


Figure 1 The LHCb spectrometer seen from above (cut in the bending plane), showing the location of the five Muon Stations.

1 Introduction

Muon triggering and offline muon identification are fundamental requirements of the LHCb experiment. Muons are present in the final states of many CP-sensitive B decays, in particular the two “gold-plated” decays, $B_d^0 \rightarrow J/\psi(\mu^+\mu^-)K_S^0$ and $B_s^0 \rightarrow J/\psi(\mu^+\mu^-)\phi$. Moreover, muons from semi-leptonic b decays provide a tag of the initial state flavour of accompanying neutral B mesons. In addition, the study of rare B decays such as the flavour-changing neutral current decay, $B_s^0 \rightarrow \mu^+\mu^-$, may reveal new physics beyond the Standard Model.

The LHCb muon detector uses the penetrative power of muons to provide a robust muon trigger. The heavy-flavour content of triggered events is enhanced by requiring the candidate muons to have high transverse momentum, p_T . The same unique properties are utilised offline, to accurately identify muons reconstructed in the tracking system and to provide a powerful B-meson flavour tag.

In this introduction, the physics requirements are discussed and an overview of the muon detector system is presented. A brief summary of the evolution since the Technical Proposal is then given, followed by an outline of the rest of the document.

1.1 Physics requirements

The main requirement for the muon detector is to provide a high- p_T muon trigger at the earliest trigger level (Level-0). The effective LHCb Level-0 input rate is about 10 MHz, on average, at $\mathcal{L} = 2 \times 10^{32} \text{ cm}^{-2} \text{ s}^{-1}$, assuming a non-diffractive inelastic p-p cross-section of 55 mb. This input rate must be reduced to 1 MHz within a latency of $4.0 \mu\text{s}$, while retaining good efficiency for events containing interesting B decays. The muon trigger provides between 10% and 30% of this trigger rate. In addition, the muon trigger must unambiguously identify the bunch crossing, requiring a time resolution better than 25 ns.

The muon detector consists of five muon tracking stations placed along the beam axis and interspersed with a shield to attenuate hadrons, elec-

trons and photons. The muon trigger is based on a stand-alone muon track reconstruction and p_T measurement with a resolution of 20%. To trigger, a muon must hit all 5 muon stations, giving a lower momentum threshold for efficient muon triggering of about $5 \text{ GeV}/c$. Hits in the first two stations are used to calculate the p_T of the candidate muon.

The polar angle and momentum of particles are correlated, such that high-momentum tracks tend to be closer to the beam axis. Multiple scattering in the absorber increases with the distance from the beam axis, limiting the spatial resolution of the detector. The granularity of the detector varies such that its contribution to the p_T resolution is approximately equal to the multiple-scattering contribution. The various contributions to the p_T resolution are shown in Figure 2.

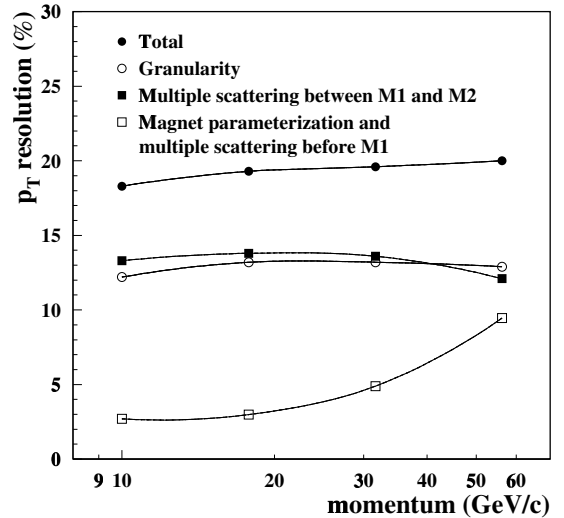


Figure 2 Contributions to the transverse-momentum resolution as a function of the muon momentum, averaged over the full acceptance. The p_T resolution is defined as $|p_T^{rec} - p_T^{true}|/p_T^{true}$, and is shown for muons from semi-leptonic b decay having a reconstructed p_T close to the trigger threshold, between 1 and 2 GeV/c.

The muon system must also provide offline muon identification. Muons reconstructed in the high-precision tracking detectors with momenta down to $3 \text{ GeV}/c$ must be correctly identified with an efficiency of above 90%, while keeping the pion misidentification probability below 1.5%. Efficient muon identification with low contamination is required both for tagging and for the clean reconstruction of muonic final state B decays.

Table 1 The logical pad size in the four regions of each station projected to M1 (scaled as z_{M1}/z_{Mi}). This indicates the exact projectivity in y between stations and the doubling of size in both directions between regions. The region inner dimensions of M1 are also shown.

	Pad Dimensions at M1 (cm ²)					Region Inner Dimensions at M1 (cm ²)
	M1	M2	M3	M4	M5	
R1	1×2.5	0.5×2.5	0.5×2.5	2×2.5	2×2.5	24×20
R2	2×5	1 ×5	1 ×5	4×5	4 ×5	48×40
R3	4×10	2×10	2×10	8×10	8×10	96×80
R4	8×20	4×20	4×20	16×20	16×20	192 ×160

1.2 General detector structure

The positions of the muon stations within LHCb can be seen in Figure 1, which shows a top view of the experiment. The first station (M1) is placed in front of the calorimeter preshower, at 12.1 m from the interaction point, and is important for the transverse-momentum measurement of the muon track used in the Level-0 muon trigger. The remaining four stations are interleaved with the muon shield at mean positions of 15.2 m (M2), 16.4 m (M3), 17.6 m (M4) and 18.8 m (M5). The shield is comprised of the electromagnetic and hadronic calorimeters and three iron filters and has a total absorber-thickness of 20 nuclear interaction-lengths. The chambers within the filter are allocated about 40 cm of space and are separated by three shields of 80 cm thickness. The inner and outer angular acceptances of the muon system are 20 (16) mrad and 306 (258) mrad in the bending (non-bending) plane, similar to that of the tracking system. This provides a geometrical acceptance of about 20 % for muons from b decays relative to the full solid angle. The total detector area is about 435 m².

1.2.1 Logical layout

The logical layout describes the x and y logical pad granularity in each region of each muon station, as seen by the muon trigger and offline reconstruction. The physical implementation of the logical layout is presented in the next subsection. Given the different granularity requirements and the large variation in particle flux in passing from the cen-

tral part, close to the beam axis, to the detector border, each station is subdivided into four regions with different logical-pad dimensions (Figure 3). Region and pad sizes scale by a factor two from one region to the next. The logical layouts in the 5 muon stations are projective in y to the interaction point.

The x dimensions of the logical pads in stations M1 – M3 are determined primarily by the precision required to obtain good muon p_T resolution for the Level-0 trigger. The pad y dimensions in all five stations are determined by the required rejection of background triggers which do not point to the interaction region. The resulting logical pad y/x aspect ratios are 2.5 in station M1 and 5 for stations M2 and M3. Stations M4 and M5, which are used to confirm the presence of penetrating muons, have aspect ratios of 1.25. The logical pad dimensions are summarized in Table 1. The total number of logical pads in the muon system is 55,296.

1.2.2 Physical layout

The physical layout refers to the physical implementation of the logical pad layout described above. Starting from the logical pads, two steps in the implementation can be distinguished:

1. Logical pads – logical channels:

Logical pads are obtained from the crossing of horizontal and vertical strips wherever possible. These strips, referred to as logical channels, are formed from the front-end channels. This allows a reduction in the number of channels to be handled by the off-

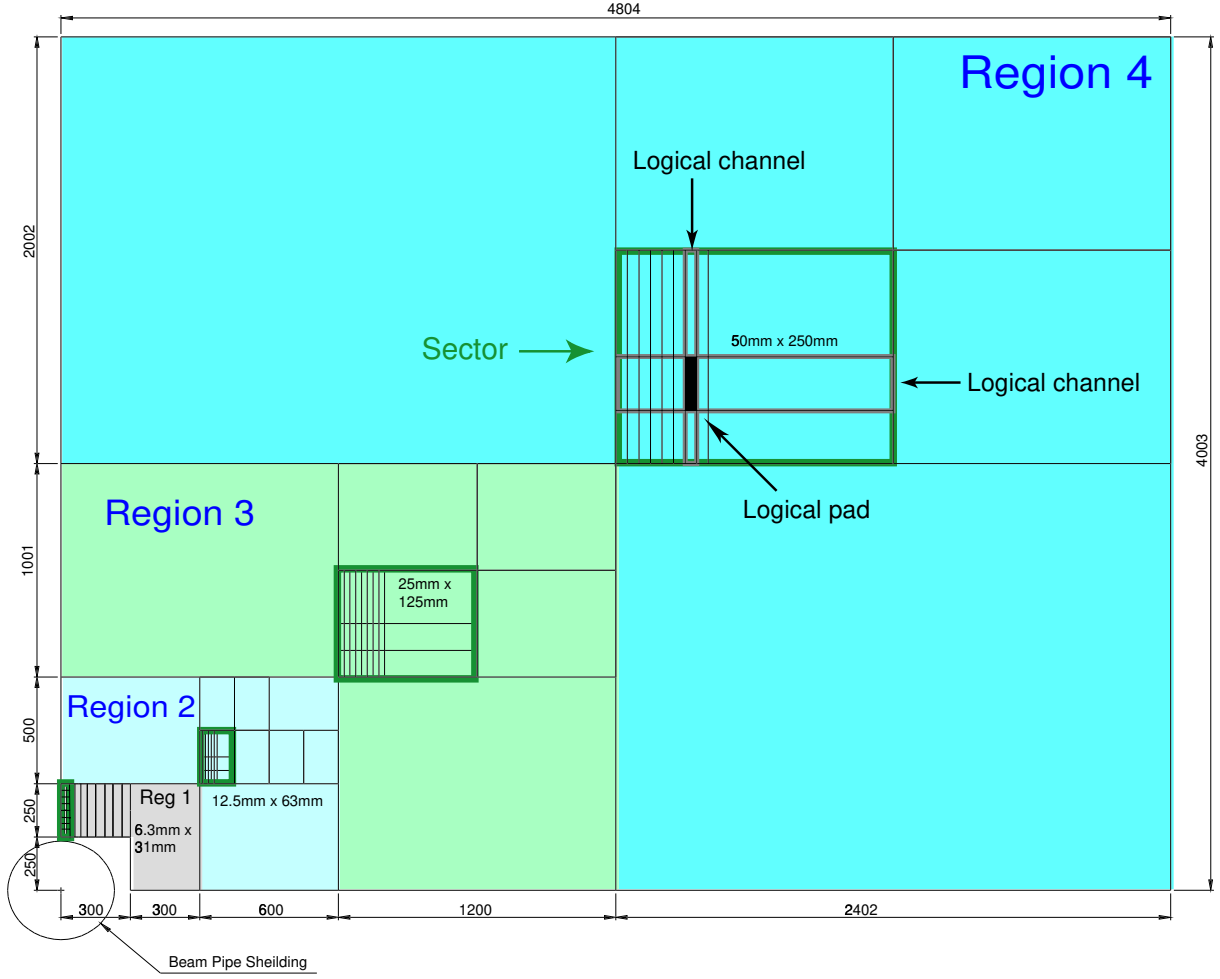


Figure 3 Front view of one quadrant of muon station 2, showing the dimensions of the regions. Inside each region is shown a sector, defined by the size of the horizontal and vertical strips. The intersection of the horizontal and vertical strips, corresponding to the logical channels, are logical pads. The region and channel dimensions scale by a factor two from one region to the next.

chamber electronics and the trigger processor from 55,296 to 25,920. The crossing of the strips is performed by the trigger processor. Strips are employed in stations M2–M5. The dimensions of the horizontal and vertical strips are limited by the logical channel occupancy.

Because of the very high particle rates in station M1, strip readout is not possible there. Similarly, in region R1 of stations M4 and M5 the intermediate step of strips is not realized, as the reduction in logical channels would be insignificant.

2. *Logical channels – physical channels:*

The chamber element readout by one front-end channel is referred to as physical channel in the following. The maximum size of the physical channels is constrained by the requirements for efficient operation of the chambers, discussed in Section 2. Therefore in general physical channels are smaller than logical channels. Physical pad readout providing a space point is preferred, where possible, as this does not require the additional logical AND of the two coordinates in an x and y strip readout of the chamber and subsequent loss of efficiency. This scheme is

followed in most of the regions.

As an exception, regions R1 and R2 of stations M2 and M3 are characterized by a y/x aspect ratio of 5 and high granularity in the bending plane (cf. Table 1). Therefore, $x-y$ readout has been chosen in this regions and the logical channels are formed from independent physical channels.

Redundancy is ensured by having two detector layers with independent readout per station. The signals of corresponding physical channels in the two layers are logically OR-ed on the chambers. The total number of physical channels in the system is about 120,000.

The readout scheme outlined above had an important impact on the detector design. Ease of construction and minimization of the number of different chamber sizes and types were other considerations in the choice of the detector layout. As a consequence, the chamber sizes are rather small, varying from $\sim 0.1 \text{ m}^2$ in region R1 to $\sim 0.5 \text{ m}^2$ in region R4. Each region of each station is implemented with chambers of one size, all using the same readout, resulting in a total of 20 different chamber types in the whole muon system.

1.3 Evolution since the Technical Proposal

With respect to the Technical Proposal [1] the muon detector has retained its basic structure, namely five measuring stations. However, many modifications have been made to the design. Some of these changes are minor, such as an increase in the absorber dimensions from 70 cm to 80 cm, and the removal of the first absorber of 30 cm thickness behind the hadron calorimeter. Others have been introduced as a consequence of a careful layout optimization study [2] and extensive R&D work on detector technologies.

1.3.1 Modifications to the logical layout

The most important changes to the logical layout are the following:

- The dimensions of the four regions have been modified in order to minimise the num-

ber of different chamber types required. The granularity in the bending plane has been drastically improved for muon stations M2 (by 100%) and M3 (by 200%), while the granularity in the non-bending plane has been reduced by 25% everywhere.

- The original logical layout, based on pads, has been replaced by a layout based on vertical and horizontal strips in stations M2 to M5, as outlined before. In addition, only two detector readout layers are envisaged per station, instead of four layers considered in the Technical Proposal for some parts of the system. This allowed a substantial reduction of the number of physical channels, from 236,000 to 120,000. Moreover, while the granularity of the system increased from 45,000 to about 55,000 logical pads, the number of logical channels could be reduced from 45,000 to 26,000. Despite this large reduction of readout channels, the performance of the L0 muon trigger is very similar to that reported in the Technical Proposal (for details see Section 3).

1.3.2 Modifications to the detector technologies

In the Technical Proposal, Multigap Resistive Plate Chambers (MRPC) and asymmetric Cathode Pad Chambers (CPC) were suggested as technologies for the muon system. During a period of extensive detector R&D work other technologies have been studied as well: single and double gap Resistive Plate Chambers (RPC) [3], Thin Gap Chambers (TGC) [4], and simple Multi Wire Proportional Chambers (MWPC) [5, 6]. The first tests conducted showed that the MRPCs [7] do not perform better than single gap RPCs, which are much simpler to construct. Therefore the MRPCs have not been considered further as a technology for the LHCb muon system. For the final choice between the other technology options, an internal LHCb review panel supplemented by external experts was set up to arrive at a decision. Based on performance studies, more refined estimates of the background rate [8, 9] and ageing conditions in the detectors, and finally cost, risk and resources

considerations, the following conclusion has been reached:

- Most regions of the detector (52% of the total area) should be instrumented with MWPC chambers operated in low gain mode. From the point of view of ageing they are superior to TGCs operated in limited space charge mode.
- RPCs should be employed in the outer regions (R3 and R4) of the last two stations (M4 and M5), where the particle rate is below 1 kHz/cm^2 (48 % of the total area).

Finally, the technology for the inner part (R1 and R2) of the first station M1, where rates of up to 460 kHz/cm^2 are considered, must still be selected. This amounts to 2.9 m^2 , i.e. less than 1% of the total area.

1.4 Structure of this document

This Technical Design Report is intended to be a concise but self-contained description of the Muon system. Further details can be found in the many Technical Notes, referenced throughout.

Detector specifications are given in Section 2. This is followed by a description of the physics performance of the system, determined using simulated events, in Section 3. Section 4 contains an overview of results obtained in the laboratory and at the test beam using prototypes, which give confidence that the required performance will be achieved. The technical design of the detectors is presented in Section 5, and finally the issues of project organisation, including the schedule and cost, are discussed in Section 6.

2 Detector Requirements and Specifications

The basic function of the LHCb Muon system is to identify and trigger on muons produced in the decay of b hadrons. The trigger logic is designed in such a way that information from all five muon stations is required. In order to achieve a muon trigger efficiency of at least 95%, the single-station efficiency has to be higher than 99%. Redundant single-station efficiency of 99% can be ensured by having two independent detector layers per station and taking the logical OR.

The detector efficiency is mainly limited by the intense flux of charged and neutral particles in the angular coverage of the LHCb experiment. These flux levels exceed those experienced by the ATLAS [10] and CMS [11] muon spectrometers and pose a different challenge.

Because of the importance of the background conditions in determining the design of the muon system, this section opens with a brief overview of backgrounds relevant to the $b \rightarrow \mu X$ detection in the LHCb experiment. The impact of the operating conditions on the muon-chamber technologies is then described and the main detector and electronics parameters are listed. Prototype tests have been undertaken and demonstrate that the listed specifications can be achieved. These tests are described in Section 4 of this document.

2.1 Background environment

High particle fluxes in the muon system impose stringent requirements on the instrumentation. These requirements include the rate capability of the chambers, the ageing characteristics of the detector and redundancy of the trigger instrumentation. The high hit rates in the chamber also effect the muon transverse momentum resolution due to incorrect hit association. Four classes of backgrounds can be distinguished:

1. *Decay muons:* The large number of π/K mesons produced in the p-p collisions contribute mainly to the background in the muon system through decays in flight. Such decay muons form the main background for the L0 muon trigger.

2. *Shower particles:* Photons from π^0 decays can interact in the area around the beam pipe and generate electromagnetic showers penetrating into the muon system. Hadrons emerging from the primary collision can interact late in the calorimeters and contribute to the background in the muon system through shower muons or hadron punch-through.
3. *Low-energy background:* Another important background is associated with low-energy neutrons produced in hadronic cascades in the calorimeters, the muon shield or in accelerator components. They create low-energy radiative electrons via nuclear n- γ processes and subsequent Compton-scattering or via the photo-electric effect in the detector material of the muon chambers. The photons have a probability of a few per mil to generate detectable electrons via these effects, which are in general only affecting a single detector layer. Moreover, the hits due to the low energy background occur up to a few 100 ms after the primary collision (see Figures 10 and 11).
4. *Beam halo muons:* The charged-particle flux associated with the beam halo in the accelerator tunnel contains muons of a rather wide energy spectrum and the largest flux at small radii (see Figure 17). In particular those halo muons traversing the detector in the same direction as particles from the interaction point can cause a L0 muon trigger.

Background caused by real muons traversing the detector is well simulated with the available Monte Carlo packages. The uncertainty attached to the total p-p cross-section and to the multiplicity produced in the primary collisions is estimated at the level of 30% [12]. There is a limited knowledge of the showering processes in the absorber material and a significant uncertainty in the background due to low energy neutrons. An estimate for the rate in the various regions of the muon system has been obtained from a detailed study, comparing two simulation packages, GCALOR [13] and MARS [14]. MARS predicted a counting rate

Table 2 Particle rates in the muon system. The first row gives the maximal particle rate in each region and station per interaction as obtained from GCALOR; the second gives the calculated rate at a luminosity of $\mathcal{L} = 5 \times 10^{32} \text{ cm}^{-2} \text{ s}^{-1}$ assuming a total p – p cross-section of $\sigma=102.4 \text{ mb}$; and the last row the rate including the safety factors.

	Station 1	Station 2	Station 3	Station 4	Station 5
Region 1	$8.3 \times 10^{-3} / \text{cm}^2$	$2.7 \times 10^{-4} / \text{cm}^2$	$7.2 \times 10^{-5} / \text{cm}^2$	$4.7 \times 10^{-5} / \text{cm}^2$	$3.2 \times 10^{-5} / \text{cm}^2$
	230 kHz/cm ²	7.5 kHz/cm ²	2 kHz/cm ²	2.3 kHz/cm ²	880 Hz/cm ²
	460 kHz/cm ²	37.5 kHz/cm ²	10 kHz/cm ²	6.5 kHz/cm ²	4.4 kHz/cm ²
Region 2	$3.3 \times 10^{-3} / \text{cm}^2$	$1.9 \times 10^{-4} / \text{cm}^2$	$2.3 \times 10^{-5} / \text{cm}^2$	$1.6 \times 10^{-5} / \text{cm}^2$	$1.3 \times 10^{-5} / \text{cm}^2$
	93 kHz/cm ²	5.3 kHz/cm ²	650 Hz/cm ²	430 Hz/cm ²	350 Hz/cm ²
	186 kHz/cm ²	26.5 kHz/cm ²	3.3 kHz/cm ²	2.2 kHz/cm ²	1.8 kHz/cm ²
Region 3	$1.4 \times 10^{-3} / \text{cm}^2$	$4.7 \times 10^{-5} / \text{cm}^2$	$7.3 \times 10^{-6} / \text{cm}^2$	$5.4 \times 10^{-6} / \text{cm}^2$	$4.7 \times 10^{-6} / \text{cm}^2$
	40 kHz/cm ²	1.3 kHz/cm ²	200 Hz/cm ²	150 Hz/cm ²	130 Hz/cm ²
	80 kHz/cm ²	6.5 kHz/cm ²	1.0 kHz/cm ²	750 Hz/cm ²	650 Hz/cm ²
Region 4	$4.5 \times 10^{-4} / \text{cm}^2$	$8.3 \times 10^{-6} / \text{cm}^2$	$3.0 \times 10^{-6} / \text{cm}^2$	$1.8 \times 10^{-6} / \text{cm}^2$	$1.7 \times 10^{-6} / \text{cm}^2$
	12.5 kHz/cm ²	230 Hz/cm ²	83 Hz/cm ²	50 Hz/cm ²	45 Hz/cm ²
	25 kHz/cm ²	1.2 kHz/cm ²	415 Hz/cm ²	250 Hz/cm ²	225 Hz/cm ²

twice that of GCALOR [15]. A conservative safety factor of 5 has therefore been applied to the background rates of the GCALOR simulation for stations M2–M5 before considering the detector design. For station M1, which is positioned in front of the calorimeters and therefore less affected by the uncertainties, a safety factor of 2 has been used. The hit rate in station M1 is strongly affected by the LHCb beam pipe.

A combination of the expected rates from the various processes yields the angular-dependence of the expected counting rate in each of the five stations of the muon system. The rates have been calculated using a simulation based on GCALOR with low tracking thresholds [8, 9]. Details of the simulation studies and the obtained distributions are discussed in section 3.1. The resulting maximal rates per region are summarised in Table 2 for a luminosity of $\mathcal{L} = 5 \times 10^{32} \text{ cm}^{-2} \text{ s}^{-1}$, at which the LHCb experiment should be able to operate for short periods. The rate rises from a few hundred Hz/cm² in the outer regions of stations M4 and M5 to a few hundred kHz/cm² in the innermost part of station M1. The rates have been obtained with an Al-Be beam pipe, recently adopted for the LHCb experiment.

2.2 Muon system technologies

The combination of physics goals and background conditions have determined the choice of detector technologies for the various stations and regions. The following three parameters particularly affected the technology choice and the location of the boundary between them:

1. *Rate capability and ageing:* The high particle fluxes in the muon system affect the instantaneous efficiency of RPCs, because of a voltage drop on the electrodes. Moreover, the materials for the chambers should have good ageing properties, allowing 10 years of operation. In the case of wire chambers, the accumulated charge should not exceed 1 C/cm, which in general is considered as an upper limit for safe operation.
2. *Time resolution:* The muon system must provide unambiguous bunch crossing identification with high efficiency. The requirement is at least 95% efficiency within a 20 ns window for each of the two layers in the station.
3. *Spatial resolution:* The spatial resolution must allow the determination of the p_T of

triggering muons with a resolution of 20%. This requires a granularity in stations M1 and M2, used for the measurement of p_T , as given in Table 1. Since two detector layers are employed in each station, inclined tracks traversing the detector can hit more than one logical pad. This effect is described as geometrical cluster size. Depending on the average crossing angle, the pad size and the layer separation, the geometrical cluster size varies between 1.1 in the outer part and 1.3 in the inner part of the muon system. To minimise any additional deterioration of the intrinsic detector resolution, cross talk between readout channels should be limited such that it doesn't add significantly to the geometrical cluster size.

Based on the above considerations, RPCs have been adopted for regions R3 and R4 of stations M4 and M5, where the expected rate is below 1 kHz/cm^2 , and the requirements on cross talk are rather modest due to the large size of logical pads. This type of detector has an excellent time resolution of $\leq 2 \text{ ns}$ and is well adapted for fast triggering.

MWPC have been adopted for all other regions except the inner part of M1. A time resolution of about 3 ns is achieved in a double gap by using a fast gas and a wire spacing of 1.5 mm . Space charge effects due to the accumulation of ions are not expected for rates of up to 10 MHz/cm^2 .

The choice of these two technologies, and the location of the boundary between them, also takes into account the robustness of the demonstrated performance, discussed in Section 4, and considerations of resources and schedule. The specifications of MWPCs and RPCs are summarised in the following sections.

For the inner part of station M1 ($\sim 3 \text{ m}^2$) a technology still has to be selected. Various technologies such as asymmetric MWPCs or triple-GEM detectors are under investigation. The status of the R&D for them is briefly described.

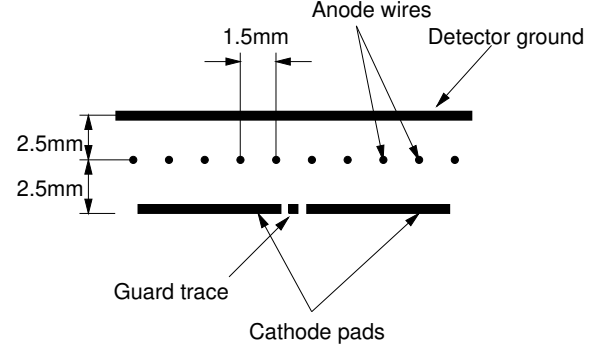


Figure 4 Schematic diagram of one sensitive gap in a MWPC.

Table 3 Main MWPC parameters

Parameter	Design value
Gas Gap	5 mm
Wire spacing	1.5 mm
Wire Diameter	$30 \mu\text{m}$
Operating voltage	3.0-3.2 kV
No. of gaps	4
Gas mixture	Ar / CO ₂ / CF ₄ (40:50:10)
Primary ionisation	$\simeq 100 \text{ e}^-/\text{cm}$
Gas Gain	$\simeq 10^5$
Threshold	$\simeq 3 \text{ fC}$
Charge / 5 mm track	$\simeq 0.8 \text{ pC}$

2.2.1 MWPC detectors

2.2.1.1 General description

A schematic diagram of an MWPC is given in Figure 4, and the principal chamber parameters are summarised in Table 3. The chambers have a symmetric cell with an anode-cathode distance of 2.5 mm and an anode-wire spacing of 1.5 mm . The MWPC gas is a non-flammable mixture of Ar/CO₂/CF₄ (40:50:10). The fact that this gas contains no hydrogen results in a low sensitivity to neutron background.

A muon crossing the 5 mm MWPC gas gap will leave an average 50 electrons that drift to the wires in the electric field. The electrons and ions moving in the avalanche close to the wire induce a negative signal on the wire and a positive signal with the same shape and about half the magnitude

on each of the cathodes. Each chamber contains four sensitive gaps which are connected as two double gaps to two front-end channels. This provides redundancy and ensures that the efficiency of each double gap is about 99%.

Chambers are readout differently, depending on their position in the muon system. In region R4 of stations M1 – M3 the chambers have anode-wire readout (through decoupling capacitors). In region R3 of stations M1 – M3 and regions R1 and R2 of stations M4 and M5 cathode pads are readout. In regions R1 and R2 of stations M2 and M3 a combined readout of wire and cathode pads is used as a consequence of the required granularity. Anode wires are grouped into vertical strips to measure x whereas the y coordinates are provided by the coarser granularity of the horizontal cathode pads. Wires are grouped in pads of 4 to 42 to match the required granularity, varying from 6 mm in region R1 of station M2 to 62 mm in region R2 of station M5. These groups of wires are referred to as *wire-pads* in this document. The muon system requires 864 four-gap chambers, with $\simeq 2.5 \times 10^6$ wires and about 80,000 front-end channels.

2.2.1.2 Special conditions and requirements

Ageing: High rates of up to 70 kHz/cm² raise concerns about chamber ageing due to gas polymerisation on wires or cathodes. The chambers must survive 10 years of operation (10^8 s) at the nominal luminosity of $\mathcal{L} = 2 \times 10^{32}$ cm⁻² s⁻¹ with the operational gas gain of 10^5 . The accumulated charge under these conditions will be about 0.5 C/cm on the wires and 1.7 C/cm² on the cathodes in the regions of highest particle flux.

Cross talk: Two sources of cross talk can be distinguished: (1) directly induced cross talk, if a particle crosses the chamber close to the edge of a pad, and (2) electrical cross talk, due to capacitive coupling between pads.

The amount of directly induced cross talk between cathode pads is given by the wire pitch and cathode-wire distance. To keep the cross-talk rate from direct induction below 20% the cathode pad dimensions should be larger than 2.2 cm [16], assuming a threshold of six primary electrons. In

case of wire-pad readout, cross talk due to direct induction is negligible, as it occurs only if a particle crosses a gap at less than 200 μ m from the centre between to neighbouring wire pads. On the other hand, the average geometrical cluster size increases as the wire-pad size decreases for the same average track inclination, given the 4.6 cm separation of the outer gaps within a chamber (see Figure 46). To keep the average geometrical cluster size below 1.2, the wire-pad size should be at least 6 mm.

Electrical cross talk between pads depends on several factors, including the amplifier input impedance, the pad capacitances and mutual pad to pad capacitances. Between wire pads it can only be limited by a low amplifier input impedance. Electrical cross talk between cathode pads can in addition be limited by guard traces in between the pads. It was shown [16] that for an amplifier input impedance of $\leq 50 \Omega$ together with the pad layout described in Section 5.1.2.2 the electrical cross talk does not add significantly to the geometrical cluster size described earlier.

2.2.2 RPC detectors

RPCs [17] are parallel plate chambers with a gas gap between two resistive electrodes. They are characterised by excellent timing properties. The readout occurs via capacitive coupling to external strip or pad electrodes, which are fully independent of the sensitive element. Further advantages compared to other technologies are the robustness and simplicity of construction. They are also well adapted to inexpensive industrial production.

2.2.2.1 General description

The operating principle of the RPC is shown in Figure 5. Ionising particles create electron-ion clusters in the gas, where an intense constant electric field is present between two parallel plates. Multiplication in the gas, averaged over the gap, is typically $\approx 10^7$. The large gas gain is necessary in order to have high efficiency even for those clusters that are created close to the positive electrode. Dense gases with high Z are preferred since they have a large ionisation probability. The plates are

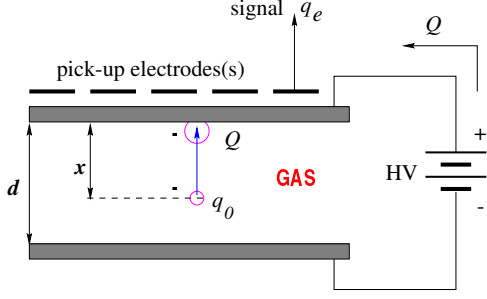


Figure 5 Principle of the RPC. Primary electron clusters, moving in the gas over a distance x , create an avalanche of total charge Q . A charge q_e is induced on the readout electrode(s).

Table 4 Main RPC parameters

Parameter	Design value
Gas gap	2 mm
Operating voltage	9-10 kV
Gas mixture	$C_2H_2F_4 / C_4H_{10} / SF_6$ (95:4:1)
Gas gain	$\approx 10^7$
Avalanche charge	≈ 30 pC
time resolution	< 2 ns
No. of RPC/chamber	2
Threshold	40 fC
Bakelite resistivity	$(8 \pm 2) \times 10^9 \Omega\text{cm}$

made of bakelite, a phenolic resin with high volume resistivity (typically $10^9 - 10^{11} \Omega\text{cm}$).

Given the characteristic exponential growth of the avalanche, the output signal induced on the readout electrodes has a very fast rise time ($\tau \approx 1$ ns), yielding the excellent time resolution of these detectors. A threshold of 40 fC is adequate to achieve full efficiency.

If the electric field is too large, the avalanche may be followed in time by a streamer. Working in streamer regime strongly reduces the rate capability of these detectors. Therefore, in LHCb the RPC will be operated in avalanche mode, where the charge is limited to tens of pC [18]. The main characteristics of the RPC detectors of LHCb are summarised in Table 4.

The gas mixture ensures high efficiency and a wide operating plateau (about 500 V) in avalanche mode. The readout electrodes are strips with a

pitch of about 6 cm, and a strip-to-strip distance of 2 mm. To cope with the requested spatial granularity the strip length in region R3 is half the length in region R4 (respectively 15 and 30 cm). The cluster size (due to particles crossing the boundary between two strips and to electro-magnetic cross-talk from a strip to another) is less than 2. To achieve the required redundant efficiency of 99% per station, each chamber will consist of two RPCs in OR with independent HV supply and readout.

2.2.2.2 Specific requirements

In the RPC detectors, once the avalanche has developed, the bakelite plates are locally discharged and the detector remains insensitive in a small region around the hit spot. The time needed to recharge the plates and restore the field limits the rate performance of the RPC. Since the time constant for recharge is directly proportional to the bulk resistivity ρ of the electrodes (being of the order of milliseconds), it is desirable to have low-resistivity bakelite for the electrodes. Bakelite plates are now available in a wide range of resistivities. ATLAS and CMS, which operate at relatively low rate, use $\rho = 10^{10} - 10^{11} \Omega\text{cm}$ [10, 11]. In LHCb the specifications require a maximum rate capability of 750 Hz/cm² (see Table 2). This can be achieved by using bakelite with ρ in the range $(8 \pm 2) \times 10^9 \Omega\text{cm}$ which has given very satisfactory results in our tests [19, 3].

Detailed simulation studies of RPCs have been performed, in particular on cross talk, which are reported in Ref. [20].

The relatively large rate in LHCb also raises the question of possible ageing effects, which could reduce the rate capability. The relevant parameter is the total integrated charge per cm². This amounts to about 1.1 C/cm² in 10 years of operation, a value which is 3 times larger compared to the values achieved in previous tests by ATLAS and CMS. Therefore measurements at the Gamma Irradiation Facility (GIF) facility at CERN are carried out at present to test the operation of RPC detectors for several LHCb years (see Section 4.2 for details).

The intrinsic noise of the RPCs should be low enough not to spoil the performance of the muon

trigger. Simulations of the effect of RPC noise on trigger performance have been carried out [21] (see also section 3.2.2), which show that noise can be tolerated provided its rate is limited to less than 1 kHz/cm^2 . However, ageing considerations, as discussed in Section 5.2.2.1, lead to a more stringent requirement and limit the RPC noise to less than 100 Hz/cm^2 .

2.2.3 Technology studies for the inner part of station M1

MWPCs with an anode-cathode distance of 2.5 mm have a limitation on the cathode-pad dimension of about 2.2 cm due to directly induced cross talk. With the required pad granularity in region R1 of $1 \times 2.5 \text{ cm}^2$, the cluster size would be about 1.4. Moreover, the accumulated charge during 10 years of operation at nominal luminosity in the MWPCs would be 2.9 C/cm , which is well above the upper limit generally considered safe for operation.

With the new Aluminium-Beryllium beam pipe, recently adopted as the baseline for the LHCb experiment, the before mentioned problems with symmetric MWPCs are diminished for region R2. Due to the reduced rate in this region the physical channel granularity has been increased to $2 \times 5 \text{ cm}^2$, which leads to a cluster size due to direct induction of 1.22. The total accumulated charge would be 1.2 C/cm .

The cluster size due to direct induction can also be reduced to 1.2 for region R1 if the anodes-wires are placed asymmetrically in the gas gap at 1 mm from the cathode-pads. The induced charge on the cathode pads would allow to operate the chamber at a factor two lower gas gain, which would reduce the total accumulated charge to 1.4 C/cm . Such chambers were proposed in the Technical Proposal for this part of the muon system and remain a viable option [22].

Another technology under consideration for this part of the system are triple-GEM detectors with pad readout. Concerns about the time resolution of such devices have been addressed in recent beam tests. An efficiency of 96% (93%) within a 25 ns (20 ns) time window has been measured with a chamber prototype using a CF_4 based gas

mixture and a fast pre-amplifier, which is an encouraging result [23]. The measured cluster size on a $18 \times 16 \text{ mm}^2$ ($6 \times 16 \text{ mm}^2$) pad was 1.1 (1.5). Studies on the ageing and high-rate performance of such a detector are ongoing.

2.3 Electronics

The muon system front-end (FE) electronics has to prepare the information required by the L0 muon trigger as quickly as possible and must conform to the overall LHCb readout specifications [24]. The readout electronics chain comprises the following elements (see Section 5.3 for details):

- *FE boards* on the chambers with amplifier, shaper, discriminator (ASD) chips, and chips to combine the output signals of the ASD to form logical channels;
- *Intermediate (IM) boards* on the side of the muon system, to generate logical channels for those regions where this has not been possible on the chambers, because the logical channels are made of physical channels belonging to different chambers;
- *Off-Detector Electronics (ODE) boards*, also located on the side of the detector, where the data is synchronised and dispatched to the L0 trigger. It comprises also the L0-pipelines, L1-buffers and the DAQ interface.

Several stringent requirements must be satisfied by the FE electronics, in particular by the ASD chip. The requirements for the ASD chip in the highest rate regions are summarized in Table 5. In the following some important aspects are pointed out.

In the highest rate regions the maximal total dose is about 1 MRad, which requires the use of radiation hard chips on the FE board. The layout of the chips is therefore done using $0.25 \mu\text{m}$ CMOS technology or similar processes, which are known to be radiation hard.

High signal rates have a large impact on the detector efficiency due to deadtime generated by the output pulse width of the ASD chip. Figure 6 shows how the pulse width affects the single layer

Table 5 Front-end chip requirements for the muon system. Some parameters apply only to the highest rate regions.

Parameter	Specification
Detector capacitance	40-250 pF
Maximum signal rate	1 MHz
Maximum total dose	1 MRad
Input resistance	$< 50 \Omega$
Average pulse width	< 50 ns (ASD output)
Peaking time	~ 10 ns

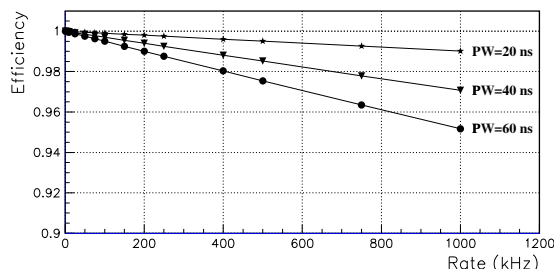


Figure 6 Efficiency as function of signal rate for pulses of different width.

efficiency, assuming that the readout electronics is only sensitive to the trailing edge of the signal. Since an output pulse width below 50 ns is unrealistic, a maximal signal rate of 1 MHz per physical channel has been defined, which keeps the inefficiency below 5%. The maximal rate per channel sets an upper bound on the size of the FE channels. In order to minimise the dead time, unipolar pulse shaping has been chosen. A unipolar linear signal processing chain also requires a BaseLine Restoration circuit (BLR) to avoid baseline fluctuations. Moreover, the chamber signal has an ion tail which requires a dedicated ion tail cancellation network to filter it.

The input resistance of the pre-amplifier has to be smaller than 50Ω in order to limit the cross talk due to capacitive coupling. Performance tests of pre-amplifiers, summarised in Section 4, show that input capacitances of up to $\simeq 250$ pF provide a satisfactory performance. This value sets an additional limitation on the size of the readout channels.

Finally, the power dissipation of the FE chip should be low to keep thermal gradients on the chambers to a minimum.

The particle rates to which the electronics of the muon system are exposed affect also the single event upset (SEU) behaviour of the system. Whenever logical operations are foreseen in the electronics, special procedures like triple voting will therefore be implemented to ensure the SEU immunity of the system.

2.4 Detector layout

The requirements and specifications described previously are an important ingredient to the detector layout summarised here. Details of the muon system configuration can be found elsewhere [25].

An important constraint to the detector layout comes from the L0-muon trigger design, which requires projectivity at each station for the correct execution of the algorithm.

From several view points the situation of station M1 is special. While M1 is not used for muon track identification, it plays an important role in the transverse momentum measurement of the muon track in the L0-trigger and is therefore positioned in front of the calorimeters. This position makes it not only subject to the highest rates in the muon system, but implies also that special care has to be taken in the detector design to minimise its radiation length X_0 . The performance studies for the calorimeter [26] have been done with a simplified muon chamber description including $0.1 X_0$ of material and showed good performance. The requirement in terms of radiation length for M1 has therefore been set to $0.1 X_0$ for the chamber sensitive area.

2.4.1 Overview

The allocated space for the muon stations is 40 cm, except for station M1, where the space is only 37 cm. The thickness of the four iron absorbers is 80 cm. The inner and outer acceptance of the muon system is $20 \text{ mrad} \times 306 \text{ mrad}$ in the bending plane (x) and $16 \text{ mrad} \times 258 \text{ mrad}$ in y . The total detector area is about 435 m^2 , of which 228 m^2 will be equipped with MWPCs and 207 m^2 with RPCs. The inner part of station M1 amounts to 2.9 m^2 . All basic muon system dimensions are summarised in Table 6.

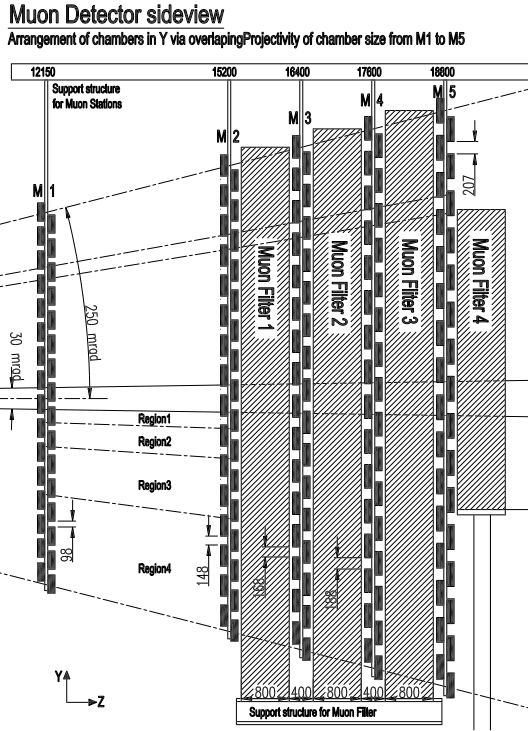


Figure 7 Side view of the muon system in the y, z plane

2.4.2 Chamber arrangement

The chosen chamber heights of 20–30 cm matches the required y -granularity in region R4. In the case of MWPCs, this allows the use of the anode-wire readout, which provides a factor two larger pulse height than the cathode signal and thus allows larger input capacitances. Moreover, constructing all chambers with the same height in one station avoids complications in the boundary area between different regions. The chamber lengths are a consequence of the aim to have the smallest possible number of different chamber types within each station. For region R4, chamber construction issues limited the chamber length.

The same chamber dimensions have been chosen for MWPCs and RPCs. Although the boundary between the two technologies has been defined, having the same chamber dimensions makes one technology the backup for the other in some regions of the muon system.

At the centre of each station will be a 44 mm (42 mm in M1) thick Aluminium chamber-support

structure. The chambers are positioned at four different z positions relative to this support, $z_{1,2}$ in front and $z_{3,4}$ behind. All chambers in the same horizontal row are either in front of, or behind the support. The chambers will be arranged as indicated in Figures 7, 8 and 9, where three views of the muon system are shown.

The positioning of the chambers in the $x-y$ plane within a station is done in such a way as to preserve as much as possible the full projectivity of the logical layout. This is mandatory for a correct execution of the L0-muon trigger algorithm and to minimise the geometrical cluster size and geometrical inefficiencies at the boundary of the chambers. The logical layout is defined at the central plane of the station and the sensitive area of each chamber is sized as if it were at this plane. The x - and y -positions of the centres of each chamber within a station are obtained simply by positioning each chamber centre so that it projects from the interaction point (IP) to its position in the logical layout at the central plane of the station. In doing so, the chambers at positions $z_{1,2}$ will overlap in x with their neighbours. The overlap however is always less than half of one logical channel. Similarly, the holes introduced between the chambers at positions $z_{3,4}$ are small, and are further limited by the thickness of the chambers of <75 mm in z . Viewed from the interaction point the total loss in angular acceptance is less than 0.1%. The corresponding y -overlaps are negligible due to the small y -dimensions of the chambers.

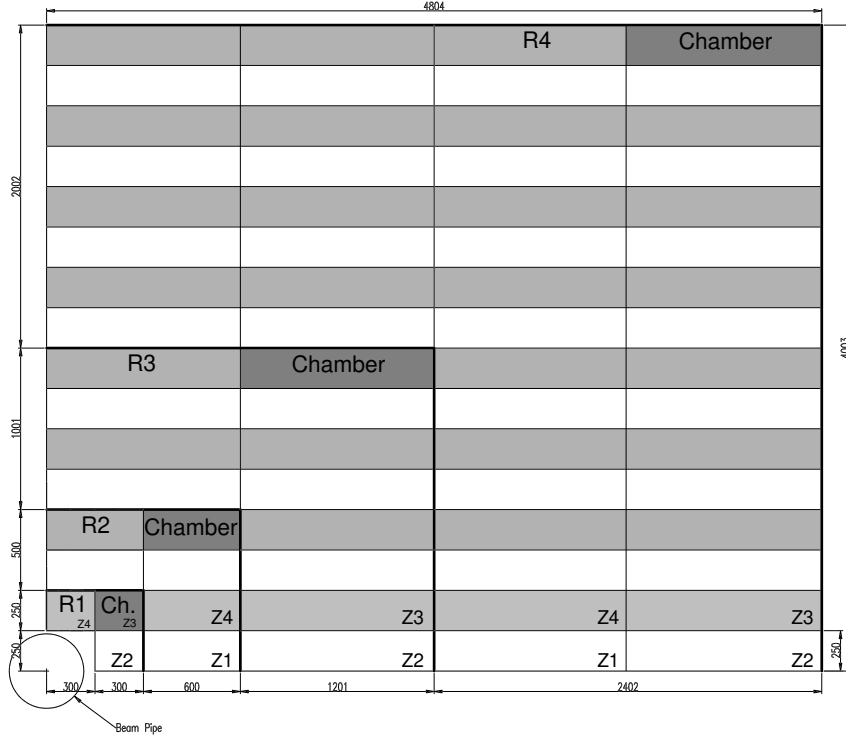


Figure 8 x,y view of a quarter of station M2, one chamber in each region is highlighted. The rows of chambers marked in a darker shade are in positions $z_{3,4}$ behind the support structure, those not marked are in $z_{1,2}$ in front of the support structure.

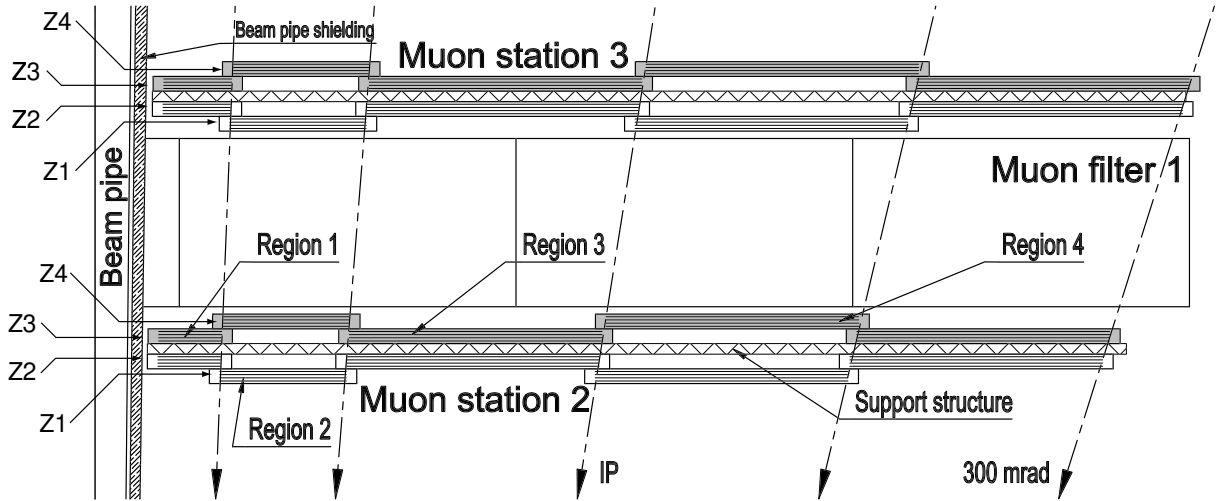


Figure 9 Partial view of the muon system in the x,z plane at $y = 0$. There are two sets of chamber positions indicated in different colours, before and after the chamber support, in each station. Each set indicates the position of the chambers in a horizontal row, the other set of positions correspond to the chambers in the rows directly above and below this row. The projectivity of the chambers to the interaction point has been indicated. The four sensitive gaps in each chamber are also indicated.

Table 6 Summary table of the Muon System parameters

	Station M1	Station M2	Station M3	Station M4	Station M5	Sum
Station z-pos.(m)	12.10	15.20	16.40	17.60	18.80	
Station dimensions(m ²)	7.7×6.4	9.6×8.0	10.4×8.6	11.1×9.3	11.9×9.9	435
Surface Region R1 (m ²)	0.6	0.9	1.0	1.2	1.4	5.1
Technology	t.b.d.	MWPC	MWPC	MWPC	MWPC	
Readout	t.b.d.	Combined	Combined	Cathode	Cathode	
No. of chambers	12	12	12	12	12	60
Chamb.sens.area (cm ²)	24×20	30×25	32.4×27	34.8×29	37.1×30.9	
Physical channels	4608	2688	2688	2304	2304	14592
Logical channels	2304	1536	1536	1152	1152	7296
Logical unit size (cm ²)	–	3.75×25	4.05×27	–	–	
Logical pad size (mm ²)	10×25	6.3×31.3	6.7×33.7	29×36	31×39	
Surface Region R2 (m ²)	2.3	3.6	4.2	4.8	5.5	20.5
Technology	t.b.d.	MWPC	MWPC	MWPC	MWPC	
Readout	t.b.d.	Combined	Combined	Cathode	Cathode	
No. chambers	24	24	24	24	24	120
Cham.sens.area (cm ²)	48×20	60×25	64.8×27	69.5×29	74.3×30.9	
Physical channels	9216	5376	3840	2304	2304	23040
No.logical channels	2304	1536	1536	672	672	6720
Logical unit size (cm ²)	–	15×25	16.02×27	17.4×29	18.6×30.9	
Logical pad size (mm ²)	20×25	12.5×62.5	13.5×67.5	58×72	62×77	
Surface Region R3 (m ²)	9.2	14.4	16.8	19.3	22.1	81.8
Technology	MWPC	MWPC	MWPC	RPC	RPC	
Readout	Cathode	Cathode	Cathode	Electrode	Electrode	
Number of Chambers	48	48	48	48	48	240
Sensitive area (cm ²)	96×20	120×25	129.6×27	139×29	148.5×30.9	
Physical channels	9216	9216	9216	4608	4608	36864
No. logical channels	2304	1344	1344	480	480	5952
Logical unit size (cm ²)	–	60×50	65.54×27	70.4×58	74×62	
Logical pad size (mm ²)	40×100	25×125	27×135	116×145	124×155	
Surface Region R4 (m ²)	36.9	57.7	67.2	77.4	88.3	327.3
Technology	MWPC	MWPC	MWPC	RPC	RPC	
Readout	Anode	Anode	Anode	Electrode	Electrode	
No. chambers	192	192	192	192	192	960
sensitive area (cm ²)	96×20	120×25	129.6×27	139×29	148.5×30.9	
Physical channels	9216	9216	9216	9216	9216	46080
No. logical channels	2304	1344	1344	480	480	5952
Logical unit size (cm ²)	–	120×100	130×108	139×116	149×124	
Logical pad size (mm ²)	80×200	50×250	54×270	131×290	248×309	

3 Physics Performance

The performance of the muon detector, for triggering and for physics analysis, has been evaluated using simulated events. This section contains an outline of the simulation procedure, and details of the studies undertaken. The efficiency of the muon trigger under nominal conditions is reported, and information is given on the trigger sensitivity to changes in the detector characteristics. Offline muon identification is discussed both in relation to flavour tagging and in relation to channels of physics interest with $\mu^+\mu^-$ in the final state.

3.1 Simulation procedure

The event simulation consists of several basic operations, performed in series: generation, tracking of particles through the experimental apparatus, addition of background, and digitisation.

3.1.1 Event generation

Proton-proton interactions at the LHC centre-of-mass energy of 14 TeV are generated with Pythia 6.1 [27], using a multiple-interaction model characterised by varying impact parameter and a running p_T cut-off. The model parameters have been tuned [12] to reproduce results for proton-antiproton collisions at centre-of-mass energies in the range 50 GeV to 1.8 TeV, the highest energies for which data are available. Parton distribution functions are taken from the set CTEQ4L [28]. Event generation is performed taking into account the angular dispersion of the beam particles and the spatial distribution of the primary-interaction point.

3.1.2 Tracking of particles

The LHCb apparatus is described in the context of Geant 3.21 [29], following the layouts given in the relevant Technical Design Reports for calorimeters [26], RICH [30] and vertex locator [31], and using the layout of the Technical Proposal [1] for the tracking detectors. The descriptions of the five muon stations and the iron shielding closely follow the designs presented in this report. Each of

the 276 chambers forming a muon station is simulated in detail [32], taking into account the different material layers, the appropriate gas mixtures, and the aluminium frames. There are four gas gaps for an MWPC and two for an RPC. Chambers are positioned as described in Section 2.4.2, so that they are projective to the interaction region and distributed over four planes per station. The chambers' aluminium supports are not simulated, but are expected to have negligible effect on muon-system performance.

Geant transport routines track particles through the experimental setup, taking into account all secondary processes, and allowing for the effect of the magnetic field in the region of the tracking detectors. Particle decays are handled by the CLEO collaboration's QQ package [33], which relies as much as possible on measured branching fractions, and includes detailed information of decay kinematics. Except in the muon shields, electrons and photons are tracked down to an energy of 1 MeV, whereas hadrons and muons are tracked down to 10 MeV. Inside the muon shields, and to keep the event-simulation time at an acceptable level, the tracking thresholds are 10 MeV for muons and 500 MeV for other particle types. A hit is recorded in a muon chamber whenever a gas gap is traversed by an ionising particle. The coordinates for the points at which the particle enters and exits the gas gap are stored, together with the particle's time of flight.

3.1.3 Background and spillover

In stations M2 to M5, the relatively high tracking thresholds for the muon shielding suppress hits that would result from the generation of lower-energy shower particles, or from the emission and conversion of photons following thermal-neutron capture. The loss is corrected by adding background according to a set of parameterisations [8, 9]. These are obtained by comparing the minimum-bias hit distributions from the standard program and the corresponding distributions from a more complete simulation, based on the GCALOR package [13].

The tracking cut-offs in GCALOR are set everywhere to 0.1 MeV for electrons and photons,

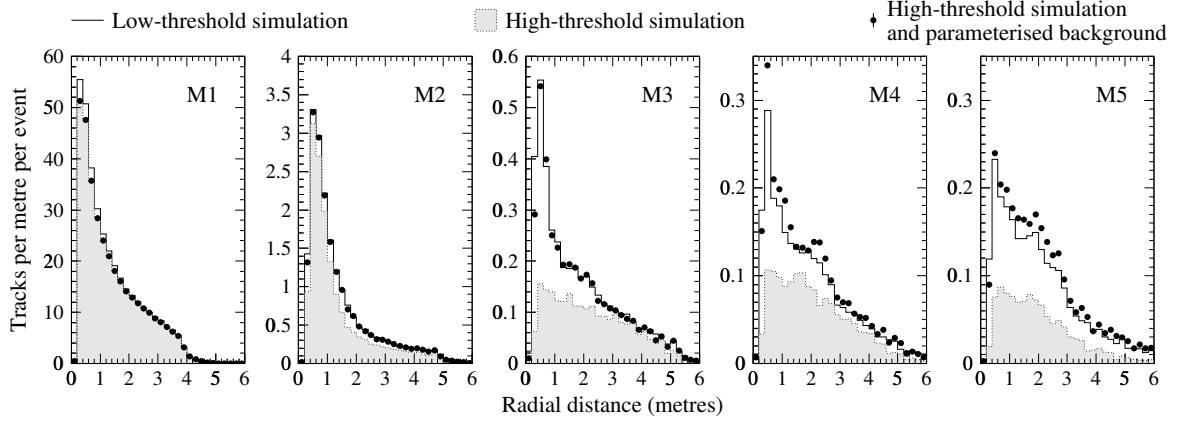


Figure 10 Radial distribution of tracks at muon stations, as given by low-threshold simulation (solid line), high-threshold simulation (shaded histogram) and high-threshold simulation with parameterised background (shaded circles).

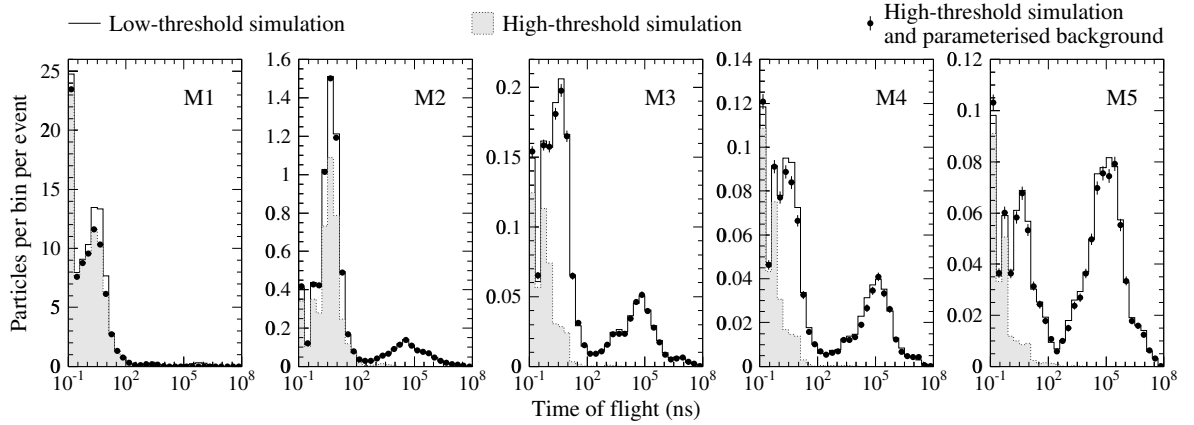


Figure 11 Particle flight times at muon stations, as given by low-threshold simulation (solid line), high-threshold simulation (shaded histogram) and high-threshold simulation with parameterised background (shaded circles). Particles produced before M1 and particles from showers in the calorimeter and muon shielding are recorded with a maximum flight time of about 100 ns. Later times, peaking at around 10^5 ns, are due to particles emitted following thermal-neutron capture.

10^{-6} eV for neutrons and 1 MeV for other particles. The GCALOR simulation also includes infrastructure elements near the muon system and relevant for low-energy processes.

Parameterisations are extracted both for the total multiplicities from GCALOR and for the differences with respect to the standard simulation. The parameterisations provide descriptions of spatial and temporal distributions, and correlations between multiplicities for high and low thresholds. With parameterised background added, the standard simulation for stations M2 to M5 reproduces the GCALOR results to better than 10% (Figures 10 and 11). No parameterised background is added for station M1. Distributions for this station from the standard simulation do not perfectly

match those from GCALOR, but disagreements are small compared with the intrinsic GCALOR uncertainties.

Possible inaccuracies in the simulation at high and low energies are accommodated by using the parameterisations of total multiplicities to increase the numbers of hits in all five muon stations, according to chosen scale factors. Two sets of scale factors are considered in the performance studies. A scale factor of 1 for each station is taken to correspond to a situation of nominal background. Scale factors of 2 for M1 and 5 for M2 to M5 define maximal background. In this latter case, the scale factor for M1 is less than for the other stations because of the smaller contribution from low-energy processes.

Low-energy particles associated with a single interaction arrive at the muon stations with flight times extending to milliseconds (Figure 11), orders of magnitude greater than the 25 ns interval between bunch crossings. This means that hits recorded in a readout window containing just one interaction can include contributions (spillover) from interactions that occurred many bunch crossings previously. The fraction of hits from spillover in a 20 ns readout window ranges from about 2% in M1 to around 20% in M5. Since spillover hits in different stations are essentially uncorrelated, their effect on occupancies is more pronounced than their effect on trigger rate.

Given that a readout channel is dead for some tens of nanoseconds after receiving a signal, particles arriving shortly before the start of the readout window can give rise to inefficiencies for detecting particles inside the window (dead-time inefficiency, see Section 2.3).

The effects of spillover and dead time on the hits detected in the muon system during each readout interval is allowed for by explicitly generating hits from earlier interactions. This hit generation is based on the parameterisations defined in relation to the background simulation.

3.1.4 Digitisation

The digitisation model closely follows the baseline choice for the muon-system readout (Section 5.3). Design values are used for the numbers of physical channels per chamber – with readout of cathode only, anode only, or both cathode and anode – and for the mappings of physical channels to logical channels. Basic response characteristics of chambers (efficiency, cross talk, noise, time jitter) and readout electronics (noise, timing) are taken into account. All response parameters can be freely varied within the simulation. Nominal values (Table 7) are based on testbeam measurements, where available, or on conservative estimates.

For each hit recorded in a muon-chamber gas gap, all physical channels lying on the line joining the entry and exit points of the hit-generating particle are initially taken as fired at the front end. The number of gas gaps giving input to a single physical channel is two for the MWPCs and one for the

Table 7 Nominal values for response parameters used in the simulation. Cross-talk probabilities have a dependence on particle position within a channel, so that values shown are indicative only.

Single-gap jitter (root-mean-square value)	
MWPC anode	5.7 ns
MWPC cathode	6.6 ns
RPC	1.4 ns
Single-gap efficiency	0.95
Cross-talk probability	
MWPC	0.08
RPC	0.15
Chamber noise	
MWPC	None
RPC	100 Hz/cm ²
Electronic noise	100 Hz/channel
Synchronisation imprecision	3 ns
Channel dead time	50 ± 10 ns
Width of readout gate	20 ns

RPCs. In regions R1 and R2 of stations M2 and M3 physical channels are calculated for the two independent readouts, whereas for other regions only a single readout is present. The number of physical channels fired per gas gap per readout is a function of the particle’s track angle and position, and effectively includes the contribution of geometrical cluster size.

A small fraction of the initially fired channels is randomly suppressed to simulate single-gap inefficiencies.

Physical channels not crossed by any particle, but adjacent to a fired channel, are taken to be themselves fired with a certain probability, so as to simulate directly induced cross talk and cross talk due to capacitive coupling. The cross-talk model used is based on the experimental measurements reported in Sections 4.1 and 4.2.

Additional physical channels are fired at random to simulate the effect of noise, two forms of which are considered. Chamber noise is expected to be negligible for the MWPCs but present at some level in the RPCs. This type of noise is expressed in terms of a count rate per unit area. Electronic noise, associated with the readout system, is

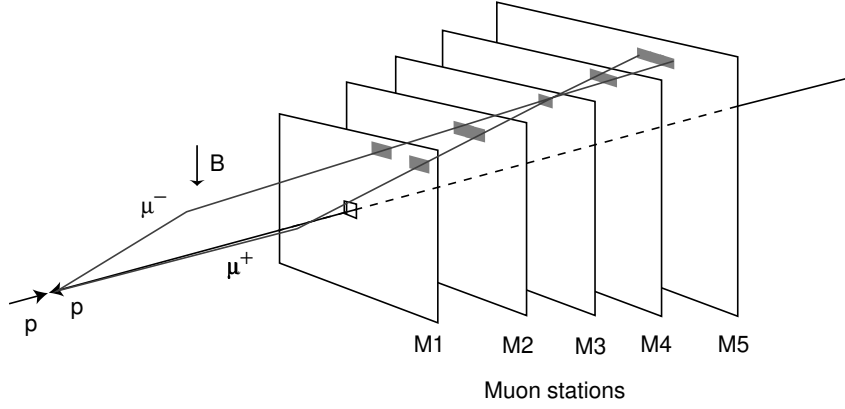


Figure 12 Track finding by the muon trigger. For each logical-pad hit in M3, hits are sought in M2, M4 and M5, in a field of interest (highlighted) around a line projecting to the interaction region. When hits are found in the four stations, an extrapolation to M1 is made from the hits in M2 and M3, and the M1 hit closest the extrapolation point is selected. The track direction indicated by the hits in M1 and M2 is used in the p_T measurement for the trigger, assuming a particle from the interaction point and a single kick from the magnet. In the example shown, μ^+ and μ^- cross the same pad in M3.

specified as a count rate per physical channel.

At this stage in the digitisation, a single physical channel may have received more than one signal. This can occur because two or more particles cross the channel, because of cross talk or noise, or because a particle induces signals in two gas gaps attached to the same front end. The arrival time of each signal is evaluated, taking into account the bunch crossing of origin, particle flight times, chamber jitter, and synchronisation imprecision. Signal losses at a channel because of the dead time associated with the arrival of an earlier signal are introduced, then a fixed-length time gate is applied. Data for the physical channels recording a signal inside the gate are transmitted to the next stage of the readout.

The two front ends of a stations are ORed together. Surviving physical channels are mapped to logical channels, in the form of strips or pads. For the strip regions, pads are defined from the intersections of horizontal and vertical strips. Pad information from all regions is used in the trigger simulation and in the muon-identification studies.

3.1.5 Future developments

The simulation and all results reported below are based on software developed in Fortran. In the future, high priority will be given to the migration to object-oriented C++ software within the framework of Gaudi [34]. The object-oriented software is expected to be at a stage where it can com-

pletely replace the Fortran software about midway through 2002.

3.2 Level-0 muon trigger

The Level-0 (L0) muon trigger and its implementation are described in detail in several LHCb notes [35, 36]. The architecture is fully synchronous and pipelined, and the algorithm run is very close to the one reported in the Technical Proposal [1], and used in the performance studies described below.

The L0 muon trigger looks for muon tracks with a large transverse momentum, p_T . It searches for hits defining a straight line through the five muon stations and pointing towards the interaction point (Figure 12). The position of a track in the first two stations allows determination of p_T .

This section contains a short description of the muon-trigger design, and a summary of the expected performance.

3.2.1 Trigger design

The L0 muon trigger is implemented with the four quadrants of the muon system treated independently. Track finding in each region of a quadrant is performed by 12 processing units, arranged on processing boards in groups of four for regions R1, R3 and R4, and in pairs for region R2 (Figure 13).

A processing unit collects data from the five muon stations for pads and strips forming a tower pointing towards the interaction point, and also

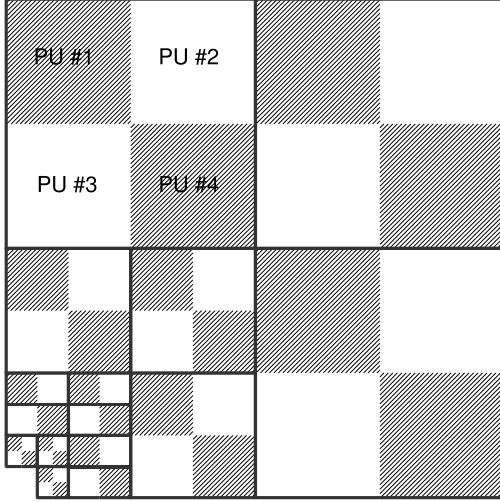


Figure 13 Organisation of the muon trigger processing boards, delimited by thick lines, and of the processing units, shown as hatched and white squares.

receives information from neighbouring towers. Track finding in a processing unit starts from the information for the 96 logical pads defined by the intersections of the 4 horizontal strips and 24 vertical strips representing the unit's input from station M3. The track search is performed in parallel for all pads.

For each logical-pad hit in M3 (track seed), the straight line passing through the hit and the interaction point is extrapolated to M2, M4 and M5. Hits are looked for in these stations in search windows, termed fields of interest (FOI), approximately centred on the straight-line extrapolation. The size of the field of interest is dependent on the station considered, the distance from the beam axis, the level of background, and the minimum-bias retention required. When at least one hit is found inside the field of interest for each of the stations M2, M4 and M5, a muon track is flagged and the pad hit in M2 closest to the extrapolation from M3 is selected for subsequent use.

The track position in station M1 is determined by making a straight-line extrapolation from M3 and M2, and identifying in the M1 field of interest the pad hit closest to the extrapolation point.

Since the logical layout is projective, there is a one-to-one mapping from pads in M3 to pads in M2, M4 and M5. There is also a one-to-one mapping from pairs of pads in M2 and M3 to pads in M1. This allows the track-finding algorithm to be

implemented using only logical operations.

Once track finding is completed, an evaluation of p_T is performed for a maximum of 2 muon tracks per processing unit. The p_T is determined from the track hits in M1 and M2, using look-up tables.

The two muon tracks of highest p_T are selected first for each processor board, and then for each quadrant of the muon system. The information for up to eight selected tracks is transmitted to the Level-0 decision unit.

3.2.2 Trigger performance

The performance of the muon system has been studied and optimised using a simulation of the trigger algorithm [35]. This algorithm is fully specified by giving the horizontal and vertical dimensions of the FOI for each station, and the cut on p_T . The muon-system performance is quantified by evaluating the trigger efficiency for selecting muons from b-hadron decays as a function of the minimum-bias (MB) retention level. Possible limitations introduced by the hardware implementation of the trigger algorithm are not considered.

3.2.2.1 Trigger efficiency

The $b \rightarrow \mu X$ acceptance is defined as the number of $b \rightarrow \mu X$ events where a prompt muon (μ_b) coming directly from the semileptonic b-hadron decay satisfies the muon trigger selection, divided by the total number of $b \rightarrow \mu X$ events in the full solid angle. The $b \rightarrow \mu X$ acceptance is the product of two contributions: the geometrical acceptance, ϵ_G , of the detector, defined as the fraction of events where the prompt μ_b hits station M3, and the trigger efficiency, $\epsilon_{\mu_{Tr}}$.

The value of ϵ_G is fixed for a defined detector layout, whereas the value of $\epsilon_{\mu_{Tr}}$ depends on the bandwidth assigned to the L0 muon trigger (the MB retention) and also on the assumptions made concerning background level and detector-response parameters. For the setup considered in this report, a Monte-Carlo calculation gives $\epsilon_G = 0.19 \pm 0.01$.

The rate of the L0 muon trigger is dominated by the presence of true muons, mainly from de-

Table 8 Performance of the L0 muon trigger algorithm, with fields of interest as given in [37]. Statistical uncertainties for the different running conditions are correlated, as the same event samples were used in all studies.

MB Retention	Nominal background		Maximal background	
	$b \rightarrow \mu X$	p_T cut	$b \rightarrow \mu X$	p_T cut
	$\epsilon_{\mu_{Tr}}$ [%]	[GeV/c]	$\epsilon_{\mu_{Tr}}$ [%]	[GeV/c]
1%	41.8 ± 1.1	1.40 ± 0.04	35.5 ± 1.8	1.69 ± 0.11
2%	55.2 ± 0.9	1.02 ± 0.02	49.7 ± 1.4	1.17 ± 0.07
3%	61.4 ± 0.7	0.75 ± 0.02	56.9 ± 1.2	0.97 ± 0.04

cays in flight of pions and kaons. The contribution from accidental combinations of particle tracks and background hits in stations M2 to M5 varies from 3% to 17%, depending on background scale factor.

A procedure has been developed to determine the trigger FOIs and p_T threshold so as to maximise $\epsilon_{\mu_{Tr}}$ for a given level of MB retention [2, 37]. If two sets of parameters give compatible performance, the set with highest p_T threshold is selected.

3.2.2.2 Event samples

Performance estimates have been obtained using 10^4 $b \rightarrow \mu X$ events and 10^5 non-diffractive inelastic interactions. Each event in the two samples corresponds to a single proton-proton collision, consistent with the use of a pile-up veto in the L0 trigger.

In the $b \rightarrow \mu X$ events, the b hadron is requested to be inside a 600mrad forward cone, a condition satisfied by about 40% of b hadrons generated over the full solid angle, and is forced to decay to a muon. The accompanying \bar{b} hadron decays according to branching fraction.

Non-diffractive inelastic interactions (55 mb cross section) are chosen as a good approximation of MB events contributing to the trigger rate. A separate study [38], using a p_T cut of 1 GeV/c, shows that the muon-trigger acceptance for diffractive interactions and elastic scatterings (combined cross section of 47 mb) is about 2% of the acceptance for the non-diffractive inelastic interactions. The contribution of diffractive and elastic events to the trigger rate is suppressed even further if the muon trigger is placed in coincidence

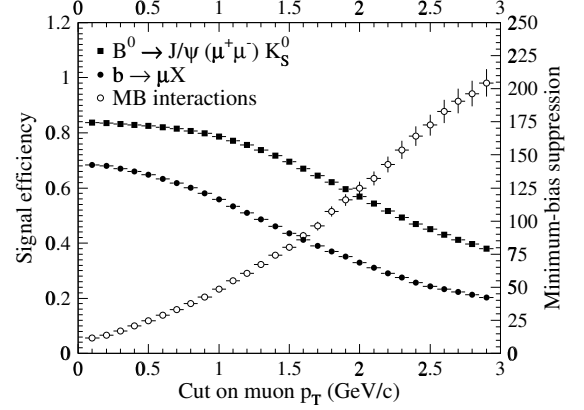


Figure 14 Minimum-bias suppression and trigger efficiency for decays indicated, for nominal background. Efficiency estimates are relative to muons that are inside the acceptance of M3 and come directly either from the b -hadron decay ($b \rightarrow \mu X$ events) or from the J/ψ decay ($B_d^0 \rightarrow J/\psi(\mu^+\mu^-)K_S^0$ events). The FOIs used are optimised for a minimum-bias retention of 2%.

with an interaction trigger, requiring, for example, a minimum energy in the calorimeters.

3.2.2.3 Results on trigger performance

Several running conditions have been considered, corresponding to different levels of MB retention and background.

The performance of the L0 muon trigger for nominal background is illustrated in Figure 14, where trigger efficiency and MB suppression are plotted as function of the p_T cut using FOI optimised to give an MB retention of 2%. The trigger performance for nominal and maximal background is summarised in Table 8, and is discussed in more detail in [37].

Comparisons have been made with previous studies, performed with simplified simulations, not

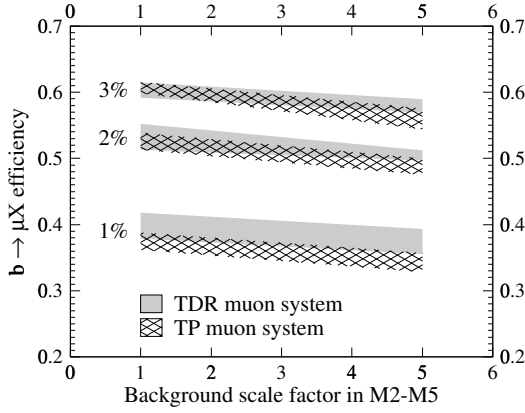


Figure 15 Trigger efficiency for $b \rightarrow \mu X$ decays within M3 acceptance as a function of background rate, for three values of MB retention. For each setup, the upper edge of a band corresponds to nominal background in M1, and the lower edge is obtained with the M1 hit rate doubled. Band edges have a statistical uncertainty of about 2%.

including details of the chamber geometry and detector response [39], as well as with results from simulations performed at various stages during the evolution of the detector layout [2]. Since the Technical Proposal, the number of logical channels has been decreased by 40%, and a realistic detector simulation has been introduced. Nevertheless, the improved detector optimisation ensures that the $b \rightarrow \mu X$ trigger efficiency is slightly better than that quoted in the Technical Proposal [1] (Figure 15).

Systematic studies have been carried out of the effect on the L0 trigger of any variation in the muon-detector efficiency and noise levels relative to the design specifications (Figure 16), and show that the system is robust [21]. In the studies, one of the response parameters is varied, while the others are kept constant. The decrease in trigger efficiency, with MB retention fixed at 1%, 2% or 3%, remains less than 5% for a single-gap efficiency as poor as 80%, for RPC noise of up to 1 kHz/cm², and for electronic noise in excess of 1 kHz/channel.

The effect of the signal time spread due to chamber jitter and synchronisation imprecision has been investigated [40], and the trigger efficiency is found to be stable under any reasonable variation in the muon-system timing characteristics.

Studies using inclusive b-hadron decays, gen-

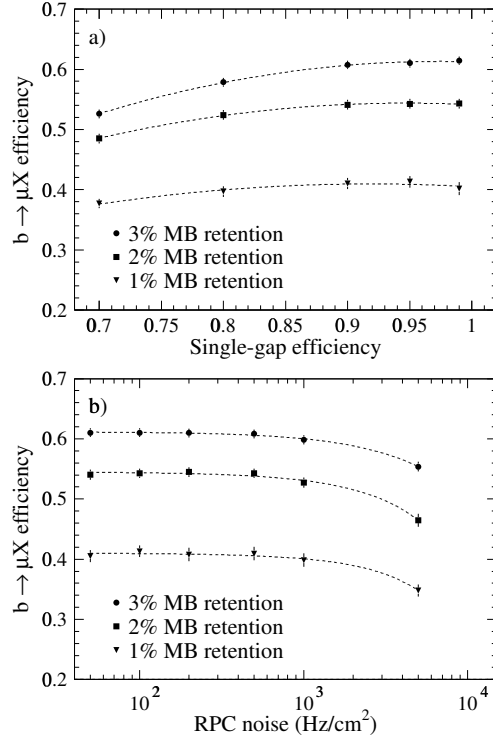


Figure 16 Trigger efficiency for $b \rightarrow \mu X$ decays within M3 acceptance as a function of (a) single-gap efficiency and (b) RPC noise, for three values of MB retention. Curves are fits of second-order polynomials to the points calculated with the simulation.

erated over the full solid angle, have also been performed [38]. With p_T cut and FOI optimised at 2% MB retention, the trigger acceptance for the inclusive b-hadron events is $(5.7 \pm 0.2)\%$. The fraction of cases in which the trigger is satisfied by a μ_b is $(34 \pm 2)\%$.

3.2.2.4 Machine-related background

Muons from the beam halo have been simulated using distributions calculated in studies of beam-gas interactions before the detector hall. The distributions of energy and radial position for muons crossing a plane 1 m upstream from the interaction point, and travelling in the direction of the muon system, are shown in Figure 17. The beam-halo muons are concentrated at small radii, and have a wide energy spectrum. About 80% have a momentum of less than 5 GeV/c, and so will be unable to penetrate the full depth of the muon system. Muons entering the experimental hall behind M5 will not cause hits in the same bunch-crossing time

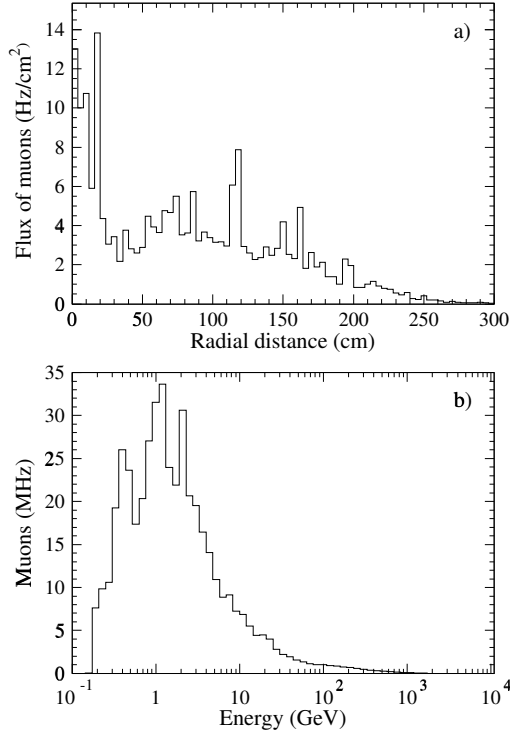


Figure 17 Distributions of (a) radial position and (b) energy, for muons from the beam halo entering the detector cavern travelling in the direction of the muon system.

window in the different muon stations. Preliminary studies indicate that beam-halo muons would be present in only 1.5% of the bunch crossings, and the fraction of bunch crossings in which a halo muon would cause a trigger is less than 0.1%. At the present level of understanding of the machine background, halo muons should not significantly affect the L0 muon trigger.

3.3 Muon identification

Efficient muon identification is important in the reconstruction of physics channels with muons in the final state, as well as for tagging the flavour of the initial b quark in decays relevant to studies of CP violation. For rare decays, such as $B_s^0 \rightarrow \mu^+ \mu^-$ it is essential to have high muon-identification efficiency while keeping the misidentification of other particles, mainly pions, as low as possible. The performance of a realistic muon-identification algorithm has been tested using reconstructed charged tracks in 10000 $b \rightarrow \mu X$ events, simulated with nominal response parameters for the muon

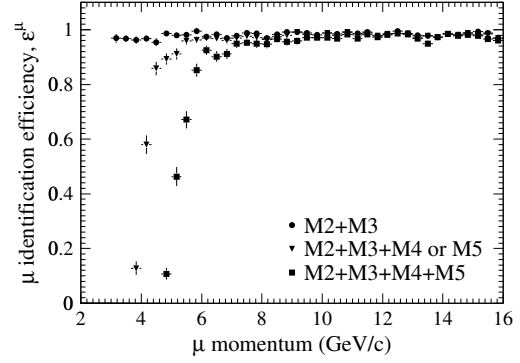


Figure 18 Muon-identification efficiency as a function of momentum, for different requirements on the number of hits. At each momentum value, muons have been generated with uniformly distributed polar angle.

system (Table 7). Full details of the study are given elsewhere [41].

Well-reconstructed tracks that have at least one hit in the vertex detector, and are within the geometrical acceptance of stations M2 and M3, are extrapolated from tracking station T10 to the muon system. The minimum momentum for a muon to penetrate to M3 is about 3 GeV/ c . A track is identified as a muon if hits are found inside rectangular search windows centred on the track extrapolation. The number of hits required is dependent on track momentum:

- M2+M3 for $p < 6$ GeV/ c
- M2+M3+M4 or M5 for $6 < p < 10$ GeV/ c
- M2+M3+M4+M5 for $p > 10$ GeV/ c

The search-window dimensions are parameterised as a function of momentum in the four regions of each station. The parameterisation is obtained using single muons, generated at the primary-interaction point with momentum flat over the range 1 to 150 GeV/ c , and with uniformly distributed polar angle. The search-window dimensions take into account the multiple scattering in the calorimeters and muon filter, as well as the finite granularity of the muon system. The momentum ranges indicated above were chosen to avoid decreases in muon-identification efficiency when a higher number of stations is required. For example, as shown in Figure 18, requiring hits in three stations rather than two has little effect on

Table 9 Muon-identification efficiency (%), and particle-misidentification probabilities (%), for $b \rightarrow \mu X$ events.

	Nominal background	Maximal background
ϵ^μ	94.0 ± 0.3	94.3 ± 0.3
\mathcal{M}^e	0.78 ± 0.09	3.5 ± 0.2
\mathcal{M}^π	1.50 ± 0.03	4.00 ± 0.05
\mathcal{M}^K	1.65 ± 0.09	3.8 ± 0.1
\mathcal{M}^p	0.36 ± 0.05	2.3 ± 0.1

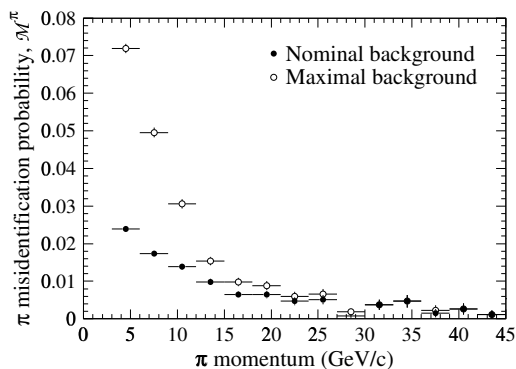


Figure 19 Pion-misidentification probability as a function of momentum, for $b \rightarrow \mu X$ events.

efficiency for muons having a momentum greater than 6 GeV/c.

Table 9 shows results obtained with $b \rightarrow \mu X$ events for the muon-identification efficiency, ϵ^μ , and for the misidentification probability, \mathcal{M} , for electrons, pions, kaons and protons. Values quoted are relative to all tracks satisfying the criteria listed above for being extrapolated to the muon system. Both nominal and maximal backgrounds have been considered.

It should be noted that the number of pions passed to the muon-identification algorithm is about a factor of 10 higher than the number of particles of other types, so pions are by far the most important source of misidentification. As would be expected, the misidentification probability is highest at low momentum (Figure 19), where the number of hits required is smallest and, to accommodate multiple scattering, search windows are largest. Also, pions of lower momentum are more likely to decay in flight before reaching the muon stations.

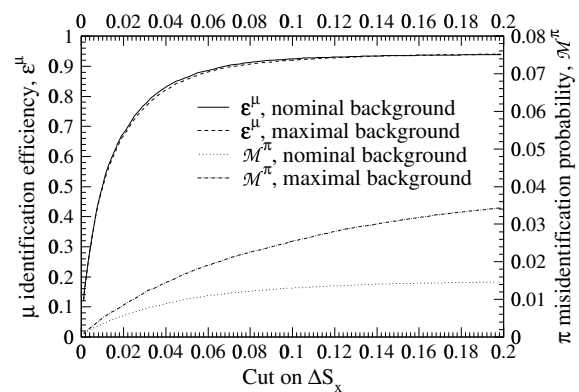


Figure 20 Muon-identification efficiency, and pion-misidentification probability, as a function of the cut on ΔS_x .

For nominal background, the muon-identification efficiency in $b \rightarrow \mu X$ events is 94% and the pion-misidentification probability is 1.5%. In 61% of cases the pion is misidentified because it decays in flight to a muon, and in 27% of cases the misidentification occurs because a muon from another hadron decay is present close to the pion. In both of these cases the hits found by the identification algorithm are due to muons. The remaining 12% of pion misidentifications result from some combination of background hits, ghost hits, and hits generated by punch through, aligned by chance with the pion track.

The number of random alignments increases with the background hits, so that for the situation of maximal background the misidentification probabilities are significantly higher. Improvement is possible by requiring that the track slope measured in the x - z plane by the muon system be consistent with the value measured in the tracking system. Figure 20 shows the muon-identification efficiency and pion-misidentification probability as a function of the difference, ΔS_x , in the two measured slopes. Under maximal background conditions, requiring ΔS_x to be less than 0.07 gives a muon-identification efficiency of 90%, while the pion-misidentification probability falls from 4% to about 2%.

In the physics analyses presented below, only about 1% of the muons relevant for decay reconstruction or flavour tagging have a momentum of less than 6 GeV/c. As a result, misidentification probabilities can be reduced, with negligible loss

of useful muons, by introducing an explicit cut on momentum. After this cut is applied, other identification criteria can be re-optimised. For particles with momentum greater than $6 \text{ GeV}/c$, and the situation of maximal background, requiring hits in all of the stations M2 to M5 and asking for ΔS_x less than 0.05 gives a pion-misidentification probability of 1.2%, while the muon-identification efficiency remains at 90%.

Information from the RICH system and from the calorimeters can be used to decrease still further the misidentification rates. A preliminary study [42] indicates that, even in the case of maximal background, misidentification probabilities of less than 1%, and a muon-identification efficiency above 90%, are readily attained.

3.4 Reconstruction of muonic final states

The analysis of b decays with muonic final states constitutes a significant part of the LHCb physics program. Of particular interest is the well-established CP-violating decay $B_d^0 \rightarrow J/\psi(\mu^+\mu^-)K_S^0$, from which the angle β of the unitarity triangle can be determined. The decay $B_s^0 \rightarrow \mu^+\mu^-$ involves a flavour-changing neutral current, and is strongly suppressed in the Standard Model. New physics might be detected as a significant enhancement of the branching fraction. The decay modes indicated give rise to muons with quite different kinematics, and so have been chosen to demonstrate the physics potential offered by the muon detector. The studies presented are preliminary.

The two analyses discussed have been performed considering only single-interaction events, 95% of which are assumed to be accepted by the pile-up veto. The combined efficiency of trigger levels L1, L2 and L3 for events that contain a fully reconstructed decay, and are passed by the pile-up veto, the L0 trigger and the offline selection, is taken to be 80%.

3.4.1 $B_d^0 \rightarrow J/\psi(\mu^+\mu^-)K_S^0$

Reconstruction of the decay $B_d^0 \rightarrow J/\psi(\mu^+\mu^-)K_S^0(\pi^+\pi^-)$ is described in detail in [43]. The first step is to select pairs of oppo-

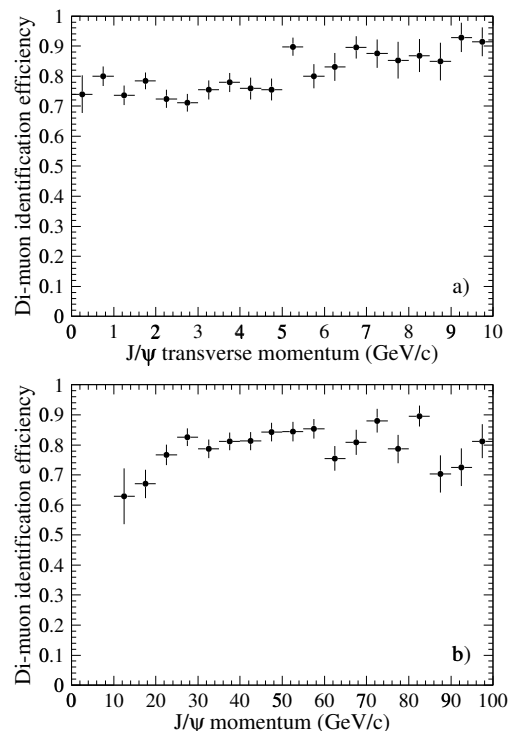


Figure 21 Probability to identify both muons of a J/ψ decay as a function of (a) J/ψ transverse momentum and (b) J/ψ total momentum. Values are calculated relative to events that satisfy the L0 trigger and analysis selection criteria, and have the tracks of the two muons reconstructed in the spectrometer. Losses from reconstructed tracks outside the geometrical acceptance of the muon system are included.

sitely charged tracks originating from a common vertex and identified as muons by the muon system (see Section 3.3). To ensure good vertex resolution, each reconstructed muon track is required to have at least one hit in the vertex detector. A J/ψ candidate is obtained when the mass of a di-muon pair is consistent with that of the J/ψ . The resolution on the J/ψ mass is $10 \text{ MeV}/c^2$. Figure 21 shows the probability to identify both muons of the J/ψ as a function of the J/ψ transverse and total momentum. The di-muon efficiency is almost flat as a function of the J/ψ transverse momentum, and has an average value of $(79.7 \pm 0.8)\%$. The geometrical acceptance of the muon system for muons reconstructed in the spectrometer decreases for J/ψ momenta below $30 \text{ GeV}/c$, because of the increased bending of the muon tracks in the magnetic field.

The K_S^0 candidates are reconstructed from two

oppositely charged tracks forming a common vertex and giving a mass consistent with the K_S^0 mass, the resolution for which is $3.5 \text{ MeV}/c^2$. Both tracks are required to be identified as pions by the RICH system. The J/ψ and K_S^0 candidates have their momenta refitted with mass constraints, and are then combined to identify B_d^0 decays. The momentum vector of any B_d^0 candidate is required to point to the reconstructed interaction vertex. The resolution on the B_d^0 mass is $7 \text{ MeV}/c^2$, and the proper-time resolution is 36 fs.

In the sample of signal events, a low-level combinatoric background is found uniformly distributed in a mass window of $\pm 60 \text{ MeV}/c$ around the peak. All of the background events are due to the combination of a true J/ψ from a b-hadron decay, and a true K_S^0 , either from fragmentation or from the decay of the other b hadron. The total number of background events can then be obtained by multiplying the number of background events found in the signal sample by the ratio $\text{BR}(b \rightarrow J/\psi X) \times \text{BR}(J/\psi \rightarrow \mu^+ \mu^-) / (f_b \times \text{BR}(B \rightarrow J/\psi(\mu^+ \mu^-) K_S^0(\pi^+ \pi^-)))$, where f_b is the probability that a b quark will fragment into a B_d^0 . The resulting background is assumed to retain a flat distribution within the mass window, and to have the same trigger acceptance as the signal. Any combinatoric background arising from the misidentification of pions as muons in the muon system is negligible. The resulting signal-to-background ratio under the mass peak (± 3 standard deviations) is 3 ± 1 .

The L0-trigger efficiency for events that have a fully reconstructed decay and satisfy the analysis selection criteria is $(98.1 \pm 0.3)\%$. The L0-muon trigger efficiency is $(95.2 \pm 0.5)\%$, and $(70 \pm 1)\%$ of the fully reconstructed decays are selected only by the muon trigger. With a $B_d^0 \rightarrow J/\psi(\mu^+ \mu^-) K_S^0(\pi^+ \pi^-)$ visible branching fraction of 1.8×10^{-5} , the present analysis shows that LHCb will fully reconstruct more than 10^5 decays per year.

3.4.2 $B_s^0 \rightarrow \mu^+ \mu^-$

The $B_s^0 \rightarrow \mu^+ \mu^-$ decay is mediated by a flavour-changing neutral current. In the Standard Model, it occurs via loop diagrams and the branching frac-

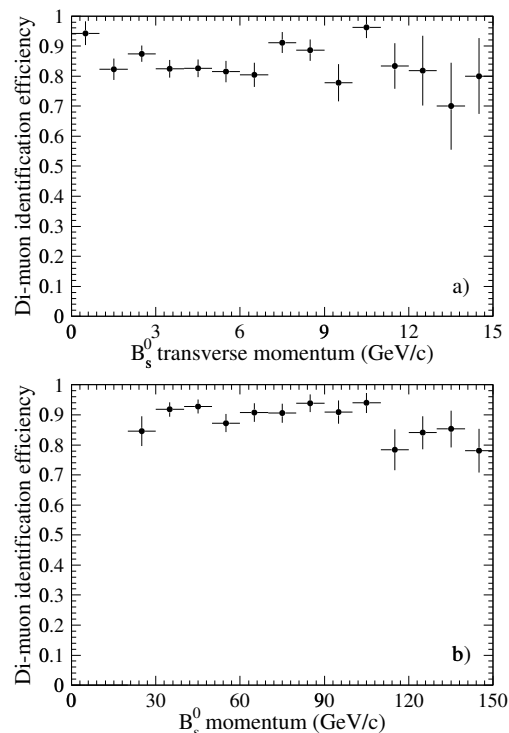


Figure 22 Probability to identify both muons of a B_s^0 decay as a function of (a) B_s^0 transverse momentum and (b) B_s^0 total momentum. Values are calculated relative to events that satisfy the L0 trigger and analysis selection criteria, and have the tracks of the two muons reconstructed in the spectrometer. Losses from reconstructed tracks outside the geometrical acceptance of the muon system are included.

tion is calculated to be about 3.5×10^{-9} [44]. The study of LHCb sensitivity to $B_s^0 \rightarrow \mu^+ \mu^-$ reported below is preliminary, and is currently limited by the low statistics available for the background estimate. Details of the reconstruction procedure are reported in [45].

The analysis uses pairs of well-reconstructed oppositely charged tracks forming a secondary vertex, and inconsistent with an origin at the interaction point. The combined momentum vector of the secondary tracks is required to point back to the primary vertex. In the absence of muon identification, the $\mu^+ \mu^-$ mass spectrum for the pairs of secondary tracks in simulated $B_s^0 \rightarrow \mu^+ \mu^-$ events is dominated by the combinatorial background. A B_s^0 mass peak, with a width of $18 \text{ MeV}/c^2$, emerges when the criteria for muon identification (Section 3.3) are applied.

The geometrical acceptance of the muon sys-

tem for $B_s^0 \rightarrow \mu^+ \mu^-$ decays with both muons reconstructed is $(92.9 \pm 0.7)\%$. The efficiency of the muon-identification procedure for pairs of reconstructed muon tracks inside the muon-system acceptance is $(88 \pm 1)\%$. Figure 22 shows the probability of having both muons inside the geometrical acceptance of the muon system and correctly identified, as a function of the B_s^0 transverse and total momentum. The efficiency is essentially flat for a B_s^0 momentum above $25 \text{ GeV}/c$.

The L0-trigger acceptance for decays with both muons identified is $(97.7 \pm 0.5)\%$, the L0-muon acceptance is $(97.3 \pm 0.5)\%$, and $(74 \pm 1)\%$ of events are selected only by the muon trigger. After one year of LHCb operation, the estimated numbers of signal and background events are 10 and 3.3 respectively.

3.5 Muon tagging

The ability to tag the flavour of the initial state of B mesons using the muon system has been studied. For this study, fully reconstructed $B_d^0 \rightarrow J/\psi(\mu^+ \mu^-) K_S^0$ events selected by the L0 trigger have been used. The $B_d^0 \rightarrow J/\psi(\mu^+ \mu^-) K_S^0$ reconstruction is as described above (Section 3.4.1).

The following pre-selection cuts are applied to reconstructed charged tracks not associated with the $B_d^0 \rightarrow J/\psi(\mu^+ \mu^-) K_S^0$ candidate, to obtain a sample of tracks with a high probability of being decay products of the accompanying b hadron:

1. $p_T > 1.2 \text{ GeV}/c$;
2. number of hits in vertex detector > 1 ;
3. impact-parameter significance > 3 ;
4. impact parameter $< 2 \text{ mm}$.

Tracks are then selected as muons if they are identified as such by the muon-identification algorithm (Section 3.3). An average of 0.053 tracks per event pass this selection, of which $89 \pm 3\%$ are muons. Some $81 \pm 4\%$ of these muons are from semi-leptonic b-hadron decays and 15 ± 4 are from $b \rightarrow c \rightarrow \mu$ decay chains. If more than one track passes all cuts, the track with the highest transverse momentum is used. The charge of the selected track is used to tag the flavour of the initial

state of the reconstructed B meson. The overall efficiency, ϵ , of the muon tag is $(5.3 \pm 0.5)\%$, and the mistag rate, ω , is $(27 \pm 5)\%$. For perfect muon identification the efficiency is $(5.1 \pm 0.5)\%$, and the mistag rate is $(25 \pm 5)\%$. These two quantities can be combined into a measure of the statistical power, \mathcal{P} , of the tag:

$$\mathcal{P} = \sqrt{\epsilon} (1 - 2\omega).$$

For perfect muon identification, $\mathcal{P} = (0.11 \pm 0.02)$, whereas in the present study $\mathcal{P} = (0.10 \pm 0.02)$.

4 Prototype Studies

An intensive programme of development work has been undertaken for the LHCb muon system. Prototypes of MWPC and RPC detectors have been constructed, allowing the study of a number of important properties in test beams and in the laboratory. A summary of the work is described in this section.

4.1 MWPC studies

General features of the MWPC design and operation are summarised in section 2.2.1. Prototype chambers have been evaluated in several test-beam studies over the past two years, and some of the key results are reported here. A full presentation of results can be found in Refs. [46, 47, 48, 49]. Before discussing the chamber performance, the front-end specifications are described, and an overview is given of the different front-end chips tested.

4.1.1 Front-end electronics

4.1.1.1 Front-end specifications

Parameters characterising the readout electronics are shown in Table 10, and are discussed in detail in Refs. [16] and [50].

Since both cathode pads and wire pads are read, the front end must be able to handle both negative and positive polarities. For a double-gap chamber with a gas gain of 10^5 , the average signal charge in the first 10 ns is 40 fC on the anode-wire pads, and half this value on the cathode pads. Landau fluctuations result in the signal having a large dynamic range, so that a scale extending to 150 fC is required to guarantee optimum tail cancellation for more than 95% of the signals. The optimum amplifier peaking time t_p is 8 ns, the time resolution degrading for both shorter and longer values. Figure 23 shows the simulated dependence of the time resolution on amplifier peaking time and threshold. The noise rate per channel requires a threshold of at least 6 primary electrons at the working point.

In the regions of highest occupancy, signal rates of up to 1 MHz/channel are anticipated.

Table 10 Electronics Parameters.

Parameter	
Av. charge in 10 ns	40 fC (double gap)
Input polarity	positive and negative
Signal tail	$t_0=1.5$ ns
Detector capacitance	40-250 pF (double gap)
Maximum signal rate	1 MHz
Maximum total dose	1 MRad
Decoupling capacitors	1 nF (double gap)
Loading resistors	100 k Ω
Coupling	AC for wire signals DC for cathode signals
Specifications	
Peaking time at disc.	~ 10 ns
Equiv. noise charge	< 2 fC ($C_{\text{det}}=250$ pF)
Linear range	150 fC
Input resistance	$< 50 \Omega$
Shaping circuit	unipolar $2\times$ pole/zero
Average pulse width	< 50 ns (ASD output)
Baseline restorer	$\sim 1 \mu$ s response time

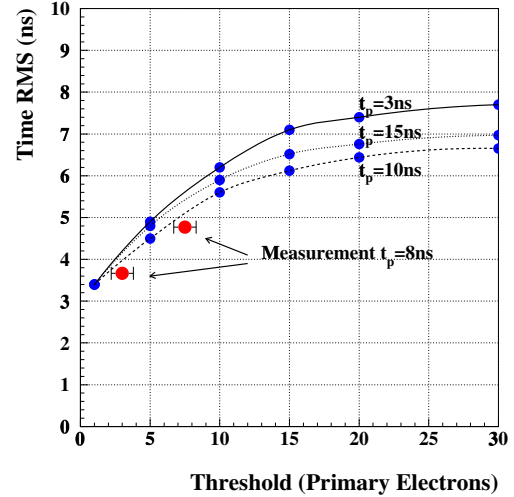


Figure 23 Simulated dependence of the time resolution on amplifier peaking time and threshold, for a single MWPC gap. At a gain of 10^5 the noise level allows a threshold of ~ 6 primary electrons.

Unipolar pulse shaping is used to minimise the dead time, which is the largest source of inefficiency. The signal has an ion tail, with a constant of $t_0 \approx 1.5$ ns [50]. A dedicated cancellation network is needed for tail suppression, the standard solution being a double pole/zero filter net-

Table 11 Parameters of front-end chips tested. The peaking time t_p is given for small values of C_{det} .

	t_p (ns)	ENC (e^-)	R_{in} (Ω)
PNPI	8	$1250+50 e^-/\text{pF}$	25
ASDQ++	10	$1740+37 e^-/\text{pF}$	25
SONY++	10	$1962+37 e^-/\text{pF}$	25
CARIOCA	10	$750+30 e^-/\text{pF}$	≤ 10

work. The average arrival time of the last electron is about 30 ns, so the front end should not increase the dead time to more than 50 ns. The input resistance must be smaller than 50Ω , to limit cross talk from capacitive coupling between adjacent channels. The noise level should be as small as possible. Since the detector capacitance represents a series noise source, the noise level is completely determined by the front-end design. The ASDQ++ front end (see below) has a good performance across the entire capacitance range, so that the $1740+37 e^-/\text{pF}$ noise of this front end is specified as the maximum tolerated. The wire signals are AC coupled and the HV loading time is $\tau = R_L C_{\text{dec}} = 100\mu\text{s}$. This implies large baseline fluctuations at high rates for a unipolar linear signal-processing chain. The front end must include a baseline-restoration circuit (BLR) to avoid this problem.

Various front-end chips have been studied in order to find the optimal solution for the muon system. Their characteristic parameters are summarised in Table 11. The aim of the studies has been to find a single chip satisfying the requirements for all regions of the system. Results obtained are discussed below.

4.1.1.2 Comparison of front-end chips

The PNPI electronics [6], built from discrete components, consists of an on-chamber preamplifier and an off-chamber main amplifier. The main characteristics are a peaking time of 8 ns, an input resistance of 25Ω , and a tail-cancellation network. The equivalent noise charge (ENC) has been measured to be $1250+50 e^-/\text{pF}$. This frontend was developed especially for the MWPCs and serves as a reference for all other front-end tests.

The SONY chip [51], originally developed for

the ATLAS TGCs, has been tested on a prototype with readout of both wire pads and cathode pads [5]. The drawbacks of this chip are a large deadtime, due to the missing tail-cancellation circuit; a poor time resolution, due to the low sensitivity; a large peaking time; and proven radiation hardness of up to only 50 kRad. It is, therefore, not possible to use this chip without additional components. With additional components, this chip would be viable only for the chambers with large wire pads, for which the requirements on radiation hardness are less stringent. For the large wire pads, the connection of eight channels to one chip results in readout traces with a length of up to 25 cm. It is, therefore, advantageous to have a preamplifier close to the pad, and to send the amplified signals to a multi-channel main amplifier and discriminator. Such a scheme has been implemented with a discrete component preamplifier and shaper close to the pad, and the SONY chip serving as main amplifier and discriminator (SONY++). This scheme has a performance very similar to that of the PNPI electronics [49].

The CMS electronics, originally developed for the CMS cathode-strip chambers, has been tested on a wire-pad chamber, but gave unsatisfactory results, probably because of the long peaking time of 30 ns. Another drawback of the chip is the long dead time, in excess of 200 ns. This chip is not appropriate for the LHCb muon system.

The ASDQ chip [47], developed for the COT chamber at Fermilab, is an offspring of the ASDBLR chip developed for the ATLAS TRT. The principle characteristics are a peaking time of 8 ns, a tail-cancellation network, an input resistance of 280Ω and an ENC of $1100+70 e^-/\text{pF}$. Except for the large input resistance and the noise slope, this chip is well matched with requirements. The weak points have been overcome by adding a common-base transistor external to the chip (ASDQ++). This lowers the impedance to about 25Ω (ASDQ++), and results in an ENC of $1740+37 e^-/\text{pF}$ [47]. This front end is a possible solution for MWPCs in all regions.

The preferred solution, however, is the CERN And RIO Current-mode Amplifier (CARIOCA) [52], a $0.25\mu\text{m}$ CMOS chip, which is at an advanced state of development. Samples built ac-

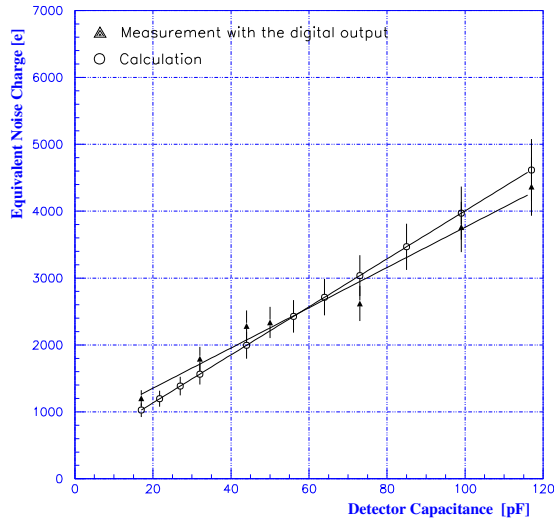


Figure 24 Dependence of equivalent noise charge on detector capacitance, for CARIOCA chip. The measured noise slope (closed circles) is $30e^-/pF$, in good agreement with the calculation.

cording to the final design should be delivered in the second half of 2002. The attractive features of the technology chosen are radiation hardness and low cost. Moreover, the measured ENC is only $750+30e/pF$. Noise studies for a prototype chip show agreement within 10% between simulation and measurement (Figure 24).

4.1.2 Results of MWPC prototype tests

4.1.2.1 Wire-pad readout

In region R4, only wire pads will be read, and cathodes will be grounded. Efficiencies of single gaps and of a double gap for an $8 \times 16 \text{ cm}^2$ wire pad, with readout using PNPI electronics, is shown in Figure 25. The corresponding ADC and TDC spectra for the double gap, at a voltage of 3.05 kV, are shown in Figure 26.

Each logical channel is to receive inputs from two double gaps per station. The efficiency plateau for a single double-gap chamber starts at about 2.95 kV (95% efficiency) and ends at 3.35 kV, giving a comfortable operating range of 400 V. The plateau end is defined by the voltage above which the dark count rate of a pad exceeds 1 kHz. The intended working point is 3.05 kV, which is 100 V above the start of the plateau. This ensures that there is good redundancy, and that the muon sys-

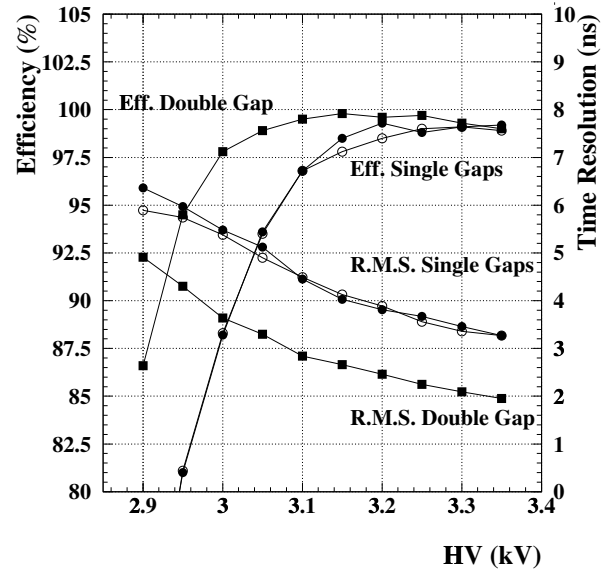


Figure 25 Efficiency (20 ns time window) and time resolution measured for two single gaps (shaded and unshaded circles) and for one double gap (shaded squares), for an $8 \times 16 \text{ cm}^2$ wire pad read using PNPI electronics [49].

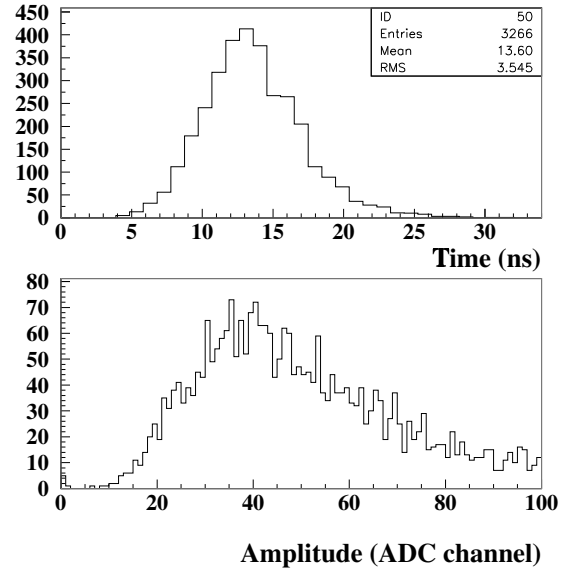


Figure 26 TDC spectrum (top) and ADC spectrum (bottom) measured for a double gap, for an $8 \times 16 \text{ cm}^2$ wire pad at an operating point of 3.05 kV [49]. The tail in the TDC spectrum is due to primary-ionization statistics and to electron-drift effects.

tem has low sensitivity to environmental variations. The electrical cross talk – the probability that a particle crossing the centre of one wire pad causes the firing of a neighbour – has been measured to be 5% for 3.15 kV and 10% for 3.25 kV.

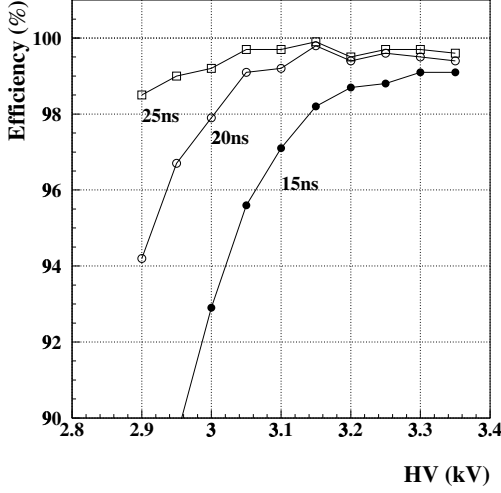


Figure 27 Double gap efficiency (time windows of 15, 20, 25 ns) for a $4 \times 16 \text{ cm}^2$ wire pad, read using the ASDQ++ front end [47].

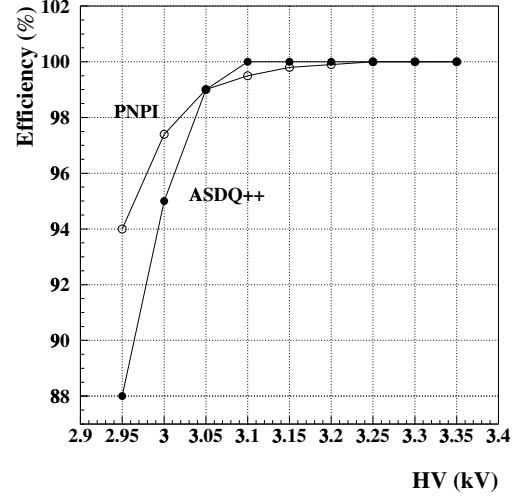


Figure 29 Double-gap efficiency (20 ns time window) for a $2 \times 8 \text{ cm}^2$ cathode pad, read using the PNPI electronics and using ASDQ++ [47].

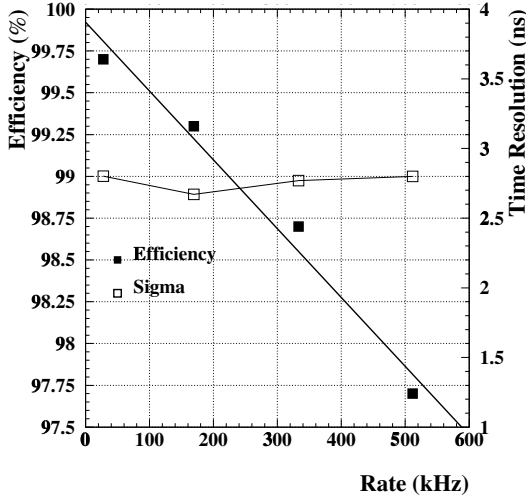


Figure 28 Double-gap efficiency (20 ns time window) and time resolution as a function of rate, for a wire pad. The fact that the time resolution is unchanged, and the efficiency drops with a slope of $0.4\%/100 \text{ kHz}$, shows that the inefficiency is due only to pile-up of signals with 50 ns average pulse width [47].

The SONY++ option has also been tested with the wire-pad chamber, and shows a performance very similar to that of the PNPI electronics with respect to efficiency and cross talk.

The ASDQ++ performance for a $4 \times 16 \text{ cm}^2$ wire pad ($C_{\text{det}} \approx 100 \text{ pF}$) is shown in Figure 27, for time windows of 15, 20 and 25 ns. The efficiency in 20 ns is 94% at 2.9 kV and 99% at 3.15 kV. The plateau length is 450 V.

The electrical cross talk has been measured to be 2.5% at 3.15 kV and 5% at 3.25 kV.

The result of a high-rate test is shown in Figure 28. The efficiency loss due to signal pile-up is about $0.4\%/100 \text{ kHz}$ for a 20 ns time window, compatible with the measured average signal pulse width of 50 ns. The fact that the measured root-mean-square value for the time resolution is independent of the rate indicates that, as expected, there are no detector effects.

4.1.2.2 Cathode-pad readout

In region R3, cathode pads will be read, and wires will be grounded at AC. The efficiency for a $2 \times 8 \text{ cm}^2$ cathode pad ($C_{\text{det}} = 40 \text{ pF}$), read using the PNPI electronics and using ASDQ++, is shown in Figure 29.

The start of the plateau is shifted by about 100 V relative to that for the wire pads, because the signal on a cathode pad is only half the signal at a wire pad. This still leaves a comfortable plateau of 350 V. The effect of the input resistance on the cross talk is shown in Figure 30. The pad-to-pad cross talk at the working point of 3.15 kV is 22% for ASDQ ($R_{\text{in}} = 280 \Omega$) and 2.7% for ASDQ++ ($R_{\text{in}} = 25 \Omega$). As expected, the cross talk is proportional to the input resistance.

In the chamber tested, the cathode pads were

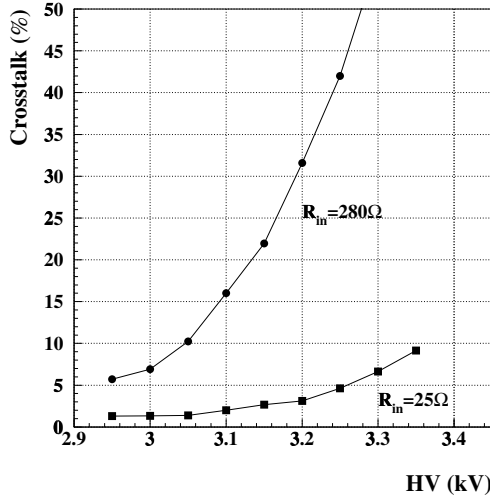


Figure 30 Cross talk between two cathode pads sharing an 8 cm edge, for input resistances of 25Ω (ASDQ++) and 280Ω (ASDQ). The cross talk is proportional to the input resistance [47].

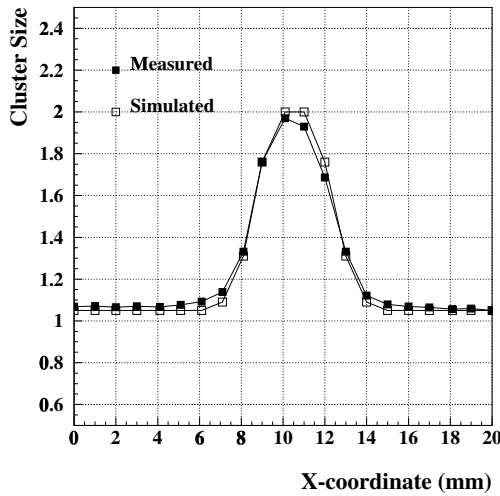


Figure 31 Measured and simulated cross talk for particles crossing the chamber close to the border between two cathode pads [47].

separated by only 0.4 mm, resulting in a cross capacitance of 1 pF/cm. In the final design, the pads are separated by 1.3 mm, with an additional guard trace. This will reduce coupling, and therefore cross talk, by a factor 4. The cross talk due to direct induction (Figure 31) is in good agreement with the simulation.

4.1.2.3 Combined readout

In regions R1 and R2, cathode pads will be read following a chess-board pattern. Wire pads will also be read in stations M2 and M3. The critical issues in these regions are, therefore, the readout traces on the cathode boards, and the combined readout of cathodes and wires. A prototype chamber containing all of the cathode structures of R1 and R2 has been tested with the ASDQ++ chip. A schematic view of this prototype is shown in Figure 32. The chamber contains two double gaps: it is a full-scale prototype with four sensitive gaps.

Small cathode pads with an edge in common (for example, 1s and 3s in Figure 32) showed a mutual capacitance of 1 pF. The capacitance between neighbouring small cathode pads where the readout trace of one pad runs underneath the other pad (for example, 1s and 2s in Figure 32) has been measured to be 4 pF. Both measured capacitances match the simulation well, showing that these parameters are well understood.

The efficiencies of small cathode pads and large wire pads, for combined readout, are shown in Figure 33. If the threshold for the cathode pads had been the same as for the wire pads, the cathode efficiency plateau would be shifted by 150 V. The shift is smaller in practice because the threshold could be set lower for the cathode pads than for the wire pads, the former having less noise.

Wire-pad cross talk has been studied by evaluating the cluster size for a chamber inclination of 4° with respect to the beam. Cluster sizes of 1.12 at 3.15 kV and 1.23 at 3.3 kV have been measured for 1.2 cm wire pads.

Electrical cross talk between cathode pads through wire pads, a crucial number for the combined readout, has been measured by focusing the beam on one cathode pad and counting cross-talk hits in its vertical neighbours. Only out-of-time cross talk has been found for this coupling, as expected. The cross-talk probabilities (pad positions as shown in Figure 32) are 0.62% (5s) and 0.57% (3s) at 3.15 kV, 1.9% (5s) and 2.1% (3s) at 3.3 kV, well within design specifications. Since the pads tested correspond to the largest wire pads to be used with combined readout, this kind of cross talk will not pose a problem.

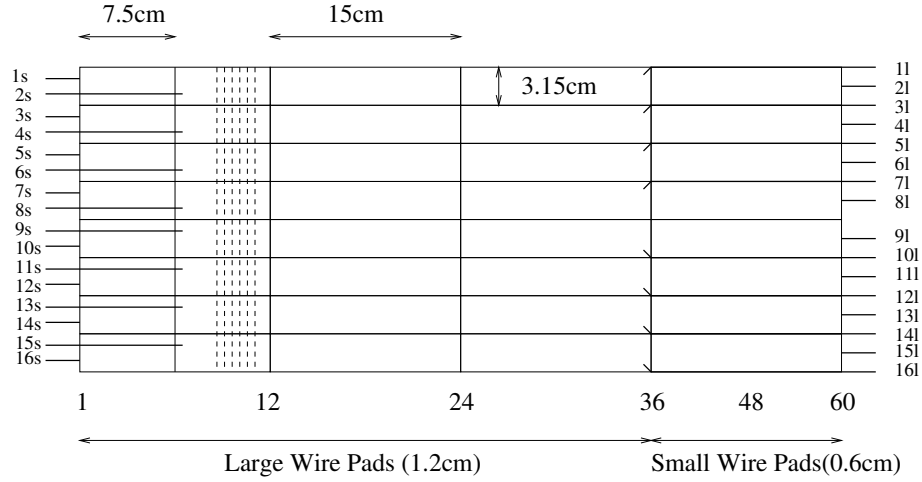


Figure 32 Schematic view of the prototype for regions R1 and R2 of M2 and M3.

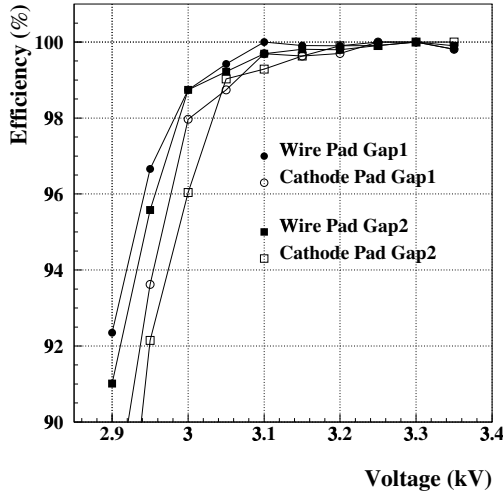


Figure 33 Efficiencies for the two double gaps of a chamber, for wire pads and cathode pads, with combined readout using the ASDQ++ and an input resistance of $25\ \Omega$. The threshold for the cathode pad is lower than that for the wire pad, and so the curves are very similar.

The electrical cross talk due to direct capacitive coupling has been evaluated by focusing the beam on pad 7s and counting the hits on pad 8s. The cross talk is entirely in time, with probabilities of 1.9% at 3.15 kV and 6.5% at 3.3 kV (mutual capacitance of 4 pF). Since the mutual capacitance between pads will be ≤ 4 pF in the entire muon system, the problem of readout traces is considered solved.

4.1.2.4 Conclusions

Test-beam measurements for prototypes indicate that the MWPCs satisfy all requirements for the LHCb muon system with sufficient redundancy. All major potential problems have been shown to be solved. The important task for the near future is to test full-size prototypes having all channels equipped with electronics, to evaluate the performance of a complete system.

4.1.3 Ageing

The performance of chambers after intense irradiation is a major concern of the experiment. Local ageing tests have been carried out at PNPI, using the same gas mixture and similar materials to those planned for the MWPCs of the muon detector. These tests show no ageing up to an accumulated charge of 13 C/cm [53].

Global ageing tests are being performed at the CERN Gamma Irradiation Facility (GIF), which provides a very intense (740 GBq) ^{137}Cs source. The CMS EMU group has recently conducted a global ageing test of this type with a chamber [54] similar to the LHCb chambers. This shows no serious ageing effects up to collected charges of 0.4 C/cm on the wires and 0.5 C/cm² on the cathodes.

A global ageing test of a prototype of a LHCb MWPC, constructed with the components and materials to be employed in the experiment is currently in progress. Unlike the CMS chambers,

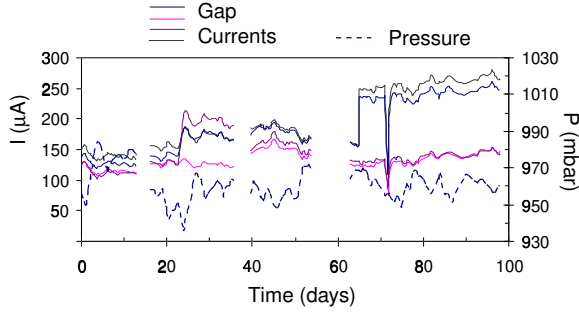


Figure 34 Current (I) drawn in each of four gaps in the MWPC prototype, as a function of time. The atmospheric pressure (P) during this period is also shown. The gaps indicate periods where the ageing test was interrupted and the dip at 72 days was due to a large drop in gas temperature.

this chamber has gold-pated cathodes, as foreseen in the regions of highest irradiation, to improve the ageing performance. The charge accumulated so far is $\sim 0.32 \text{ C/cm}^2$ on the cathodes, and about 0.1 C/cm on the anode wires, corresponding to about two LHCb years. The test will continue until the end of 2001, when an accumulated charge of 0.5 C/cm can be expected for the wires. This corresponds to the irradiation of nearly ten LHCb years in the regions of highest intensity for which MWPCs are considered. Similarly, the accumulated charge on the cathodes should be about 1.7 C/cm^2 . With the charge accumulated to date, no ageing effects have been observed. Currents recorded for each sensitive gap during the first 97 days of test are displayed in Figure 34, together with the variation in pressure. The increases in current after 23 days and after 62 days are due to a 50 V increase of high voltage, to accelerate the test. The current fluctuations are mainly due to variations in temperature and atmospheric pressure.

4.2 RPC studies

Several RPC prototypes have been built and tested, to select the most appropriate solution for the LHCb muon system. Most of the results, in particular those on rate capability, have already been reported elsewhere [3, 19]. In this section, previous tests are briefly summarised, then recent developments, concerning the front-end electronics, wider readout strips and ageing tests, are discussed.

Chambers measuring $50 \times 50 \text{ cm}^2$, and consisting of one or two gas gaps, have been built. A single gas gap has a depth of 2 mm, and is contained between two bakelite plates, each 2 mm thick and characterised by a resistivity of $9 \times 10^9 \Omega\text{cm}$. The basic steps in the gap construction are the following. First, a polycarbonate frame, 7 mm wide, is glued to one of the bakelite plates. Next, rows of disc-shaped polycarbonate spacers, $(2.00 \pm 0.01) \text{ mm}$ high and 10 mm in diameter, are glued to the same plate. The row separation and the centre-to-centre distance between spacers are both 10 cm. The gas gap is closed by the second bakelite plate, then the bakelite's internal surfaces are treated with linseed oil. The external surfaces of the bakelite are coated with a spray-on layer of graphite, which serves to distribute voltages, and are covered with a PET insulating film, $200 \mu\text{m}$ deep. Four gas inlets/outlets are positioned close to the structure's corners.

The readout electrodes are strips with a width of 3 cm or 6 cm, and lengths varying between 25 cm and 50 cm. Adjacent readout strips are shielded by 0.5 mm guard strips, to reduce cross talk.

The gas mixture used is $\text{C}_2\text{H}_2\text{F}_4/\text{C}_4\text{H}_{10}/\text{SF}_6$ (95:4:1) [55]. The main constituent, $\text{C}_2\text{H}_2\text{F}_4$, is a non-flammable, environmentally safe gas [55], characterised by high density and large primary ionisation (> 60 primary ion pairs per cm). The percentage of isobutane used is below the flammability threshold of 5.75%. The admixture of SF_6 reduces the formation of streamers.

4.2.1 Front-end electronics

In Ref. [3], two possibilities for the readout chip are presented: the GaAs-based solution adopted by ATLAS [10], and the BiCMOS-based chip developed by the Bari group for CMS [56]. Unfortunately, the production process on which the former solution was based is now obsolete, and so the ATLAS chip must be ruled out.

Readout has been performed using two different types of front-end electronics: (1) a “standard” chain consisting of hybrid fast voltage amplifiers, with a gain of about 300, followed by discriminators; (2) the 8-channel integrated charge

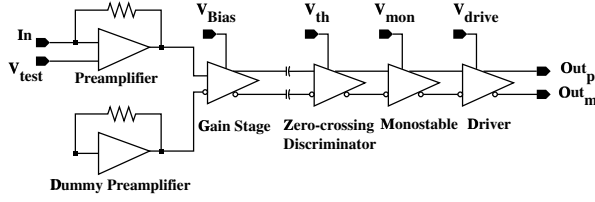


Figure 35 Block diagram for a single channel of the CMS front-end chip [56].

Table 12 Nominal properties of the CMS readout chip.

Technology	0.8 μm BiCMOS
Dimensions	$2.9 \times 2.6 \text{ mm}^2$
Input impedance	$\sim 15 \Omega$
Input polarity	negative
Dynamic range	20 fC – 20 pC
Threshold range	20 fC – 500 fC
Charge sensitivity	$\sim 1 \text{ mV/fC}$
Preamp. bandwidth	116 MHz
Equivalent Noise Charge	4 fC
Output pulse width	50 ns – 300 ns
Output level	LVDS
Power supply	+5 V, GND
Power consumption	$\sim 45 \text{ mW/channel}$

preamplifier-discriminator chip used by CMS.

The ASIC chip for the CMS front end has been designed and manufactured using 0.8 μm BiCMOS technology. The circuit comprises eight channels, each consisting of an amplifier, a zero-crossing discriminator, a mono-stable and a differential LVDS line driver. A block diagram for a single channel is shown in Figure 35. The preamplifier has an input impedance of about 15Ω at the signal frequencies. This value has been chosen in order to match the lowest value for the characteristic impedance of the CMS strips, and is close to the characteristic impedance (13Ω) of the 6 cm wide strips considered for the RPCs of the LHCb muon system.

The properties of the CMS readout chip are summarised in Table 12.

An 8-channel front-end board (Figure 36) has been built and tested in the laboratory. This prototype is designed to read eight strips of 3 cm width, with the channel inputs directly soldered on the strips, i.e. without intermediate connectors. It in-

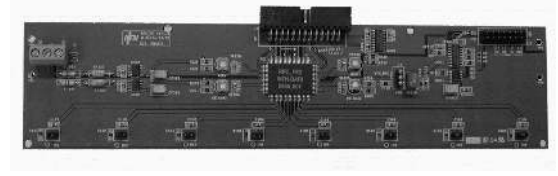


Figure 36 Photograph of the first version of the front-end board.

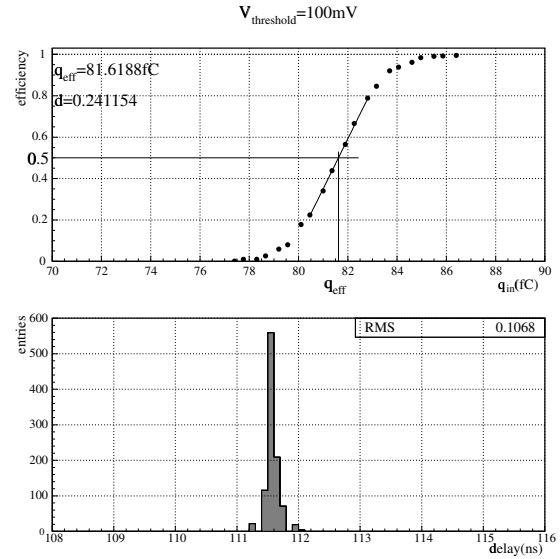


Figure 37 Typical results for (top) response as a function of input charge and (bottom) time jitter, from chip calibration at a nominal threshold of 100 mV.

cludes an adjustable voltage for remote threshold setting. The board is powered by a single voltage supply.

The performance measured for the readout chip is in agreement with that seen by CMS, with small variations among different channels and chips. The threshold calibration is about 1.1 fC/mV . Figure 37 shows the response as a function of the signal charge, and the time jitter (root-mean-square value of less than 0.11 ns). The equivalent noise charge at the input is about 4 fC. The variation in time delay among the eight channels is less than 0.35 ns , well below the requirement for the application considered.

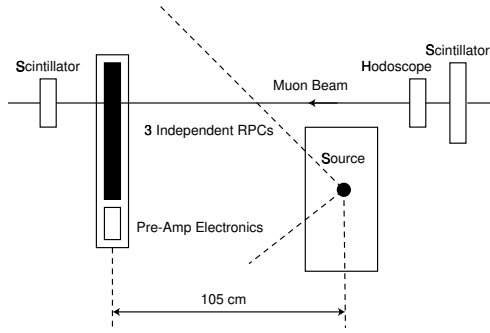


Figure 38 RPC test setup at GIF

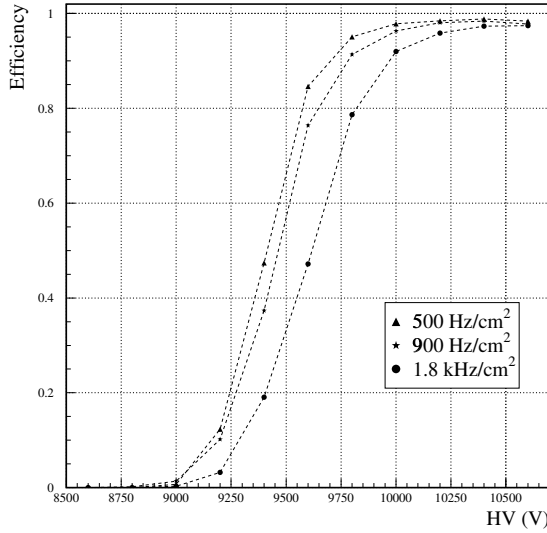


Figure 39 Efficiency curves for a single-gap RPC at GIF, for the irradiation rates indicated on the plot.

4.2.2 Results of RPC prototype tests

4.2.2.1 Rate capability

The maximum rate considered in the RPC detector is 750 Hz/cm^2 (see Table 2). The RPC performance for such a rate has been investigated using particle beams and the CERN Gamma Irradiation Facility (GIF) [57]. The latter is designed to expose large-area detectors to a continuous photon load, with fluxes comparable to those expected at LHC. The photon flux can be attenuated and adjusted using a system of filters. The setup for the GIF tests is shown in Figure 38.

Several single-gap RPCs have been tested. All had the same design, with 3-cm-wide readout strips. A double-gap RPC, following the CMS configuration (single central readout plane) has

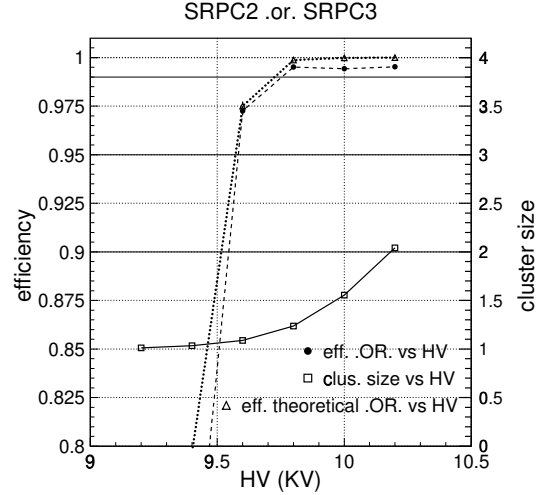


Figure 40 Efficiency and cluster size for the logical OR of two single-gap RPCs with readout strips 3 cm wide.

also been tested. The chambers were read using the “standard” electronics (see Section 4.2.1).

All single-gap RPCs gave an efficiency of more than 95% for an irradiation rate of up to 1.8 kHz/cm^2 over the entire detector surface. Figure 39 shows an example of the measured dependence of the efficiency on the applied voltage, for three different irradiation rates.

To obtain the efficiency per station required in the muon system, pairs of RPCs will be operated in OR. This ensures an overall efficiency greater than 99%, with a mean cluster size below 2, as shown in Figure 40. The double-gap RPC also had a high efficiency, but is not considered a valid option because the mean cluster size is significantly greater than 2 [3]. This is attributed to the fact that the readout planes have a different electrical layout, favouring cross talk.

4.2.2.2 Comparison of front-end electronics

The BiCMOS chip is used by CMS for double-gap RPCs, which differ from the LHCb chambers in terms of the layout of the readout plane and the composition of the gas mixture (no SF_6). A check that the chip performs satisfactorily with the LHCb setup has therefore been carried out. For this check, a single-gap RPC was equipped with BiCMOS electronics to read the signals collected on 16 strips of $3 \times 25 \text{ cm}^2$. These strips were termi-

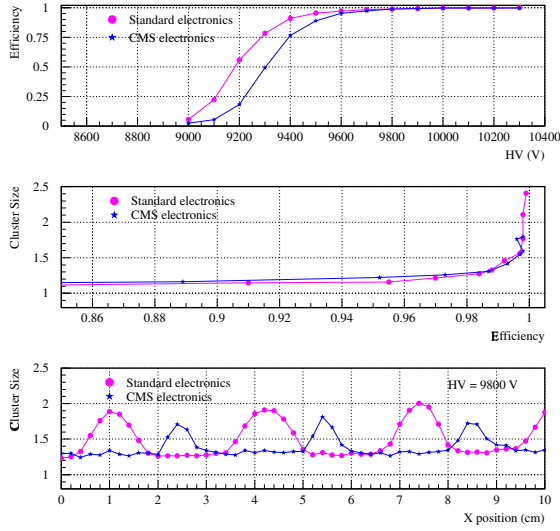


Figure 41 Comparison of test results for two identical chambers, one equipped with “standard” electronics, and one with CMS electronics. Results are given for (top) efficiency as a function of the applied voltage; (centre) efficiency as a function of cluster size; (bottom) cluster size as a function of position in the strip. The readout strips had a width of 3 cm.

nated with their characteristic impedance of about 27Ω . The efficiency and cluster size of this RPC were then measured in a test beam.

A second single-gap RPC, equipped with the “standard” electronics, has been tested in the same conditions and served as a reference. The strip length for this reference RPC was 50 cm. For technical reasons, the effective thresholds of the two RPCs were different: about 120 fC for the reference RPC, and about 180 fC for the RPC with BiCMOS electronics.

The results of the test are shown in Figure 41. The top plot shows the efficiency as a function of the applied voltage, the plateau starting at higher voltages for the BiCMOS RPC because of the higher threshold. The centre plot shows the relation between cluster size and efficiency, not expected to depend on the threshold value. Finally, the bottom plot shows the cluster size as a function of the position at which a particle crosses the strip. The peaks correspond to particles hitting the boundary between two strips. The relative shift in the peak positions for the two detectors tested is due to the different alignments with respect to the beam. The small differences between the two sets

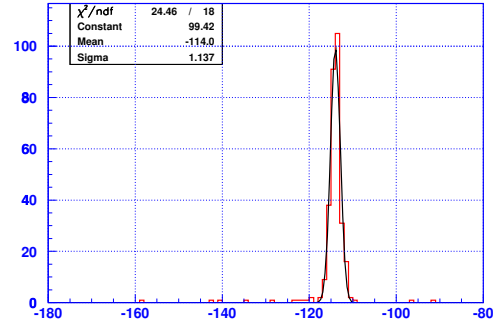


Figure 42 Time resolution of a single-gap RPC with readout strips of 6 cm width and BiCMOS electronics (trigger resolution unfolded).

of results can be understood as being due to differences in the applied thresholds and timing properties of the two electronic chains.

The conclusion from these tests is that the CMS BiCMOS electronics performs satisfactorily and can be chosen as the baseline solution for the RPC readout.

4.2.2.3 Performance with large strips

The measurements described above have all been obtained using readout strips 3 cm wide. The possibility of reducing the number of readout channels by doubling the strip width has been put forward, and is now the preferred solution (see Table 16). First tests of the detector performance with readout strips of 6 cm width have been carried out with cosmic rays, using the BiCMOS electronics. The readout strips used were 30 cm long and were terminated with their characteristic impedance. This was about 13Ω , or half the value for strips of 3 cm width. The time resolution measured is better than 1.2 ns, as shown in Figure 42, and the noise rate is less than 0.5 Hz/cm^2 .

Figure 43 shows the efficiency as a function of applied voltage for threshold values of about 70 fC and 100 fC. The efficiency in the plateau was larger than 97% in both cases. A first measurement indicates an average cluster size of about 1.2 up to the highest voltages applied. However, a precise assessment of the capacitive and geometrical contributions to the cluster size requires further measurements, using particle beams.

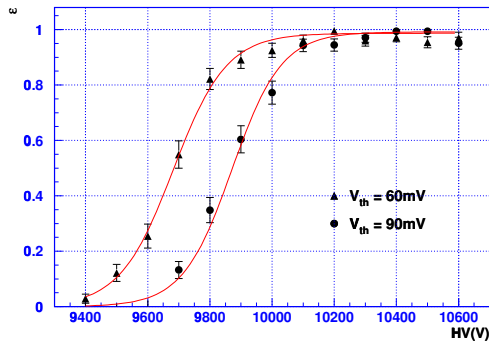


Figure 43 Efficiency as a function of applied voltage for a single-gap RPC with 6 cm readout strips and BiCMOS electronics, for two threshold values. Measurements were performed with cosmic rays.

4.2.2.4 Conclusions

The prototype tests briefly described in this section have shown that:

1. single-gap RPCs can be operated at rates of 1.8 kHz/cm^2 without degradation of performance;
2. the BiCMOS readout electronics developed by the CMS collaboration can be used for the RPC readout;
3. readout strips with a width of 6 cm show good performance.

4.2.3 Ageing

RPC detectors have not previously been operated under such heavy background conditions as are expected at the LHC. Ageing tests performed by the RPC groups of ATLAS and CMS have shown that their detectors can withstand the radiation doses expected in those experiments [58, 59]. However, the background levels expected at LHCb polar angles are an order of magnitude more severe [8]. An ageing test is therefore being performed, which should realistically reproduce the conditions of the LHCb experiment.

It has been demonstrated that the resistivity of bakelite is unaffected by radiation doses several orders of magnitude higher than those expected in LHCb [3]. The other parameter relevant to characterise ageing is the charge transported across the RPC.

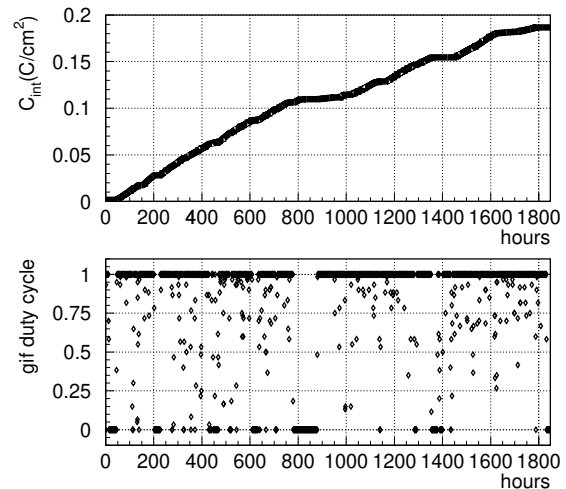


Figure 44 Summary of the GIF ageing test during the first three months of 2001, showing (top) total integrated charge density for the irradiated RPC, and (bottom) the GIF activity (time with source “on”).

Assuming a maximum particle flux of $\Phi_0 = 375 \text{ Hz/cm}^2$ in region R3, and taking 30 pC as the average avalanche charge in the RPC (see below), the current density is found to be about $J = 11 \text{ nA/cm}^2$, and the total charge accumulated in 10 LHCb years (10^8 s) is about $Q_{10y} = 1.1 \text{ C/cm}^2$. In region R4 ($\Phi_0 \sim 100 \text{ Hz/cm}^2$), the current density and the total charge are about 70% lower. For comparison, an accumulated charge of 0.3 C/cm^2 has been reached in the ATLAS test [58].

In the LHCb test, started in January 2001, a single gap RPC will be irradiated at the GIF facility for at least one year. The chamber under test is positioned at a distance of about one metre from the source. This gives a current density about three times larger than in the experiment.

The performance characteristics of an RPC depend on several parameters other than irradiation, including, for example, temperature and pressure. To isolate the effect of the irradiation, a second, similar, chamber is operated outside the irradiation area, and is used as a reference. The two chambers were thoroughly tested in the T7 beam before installation at the GIF. During irradiation, the current, temperature, pressure and counting rates of the two chambers are continuously monitored.

The average charge generated by background hits has been measured under the assumption that all current drawn by the irradiated chamber is due

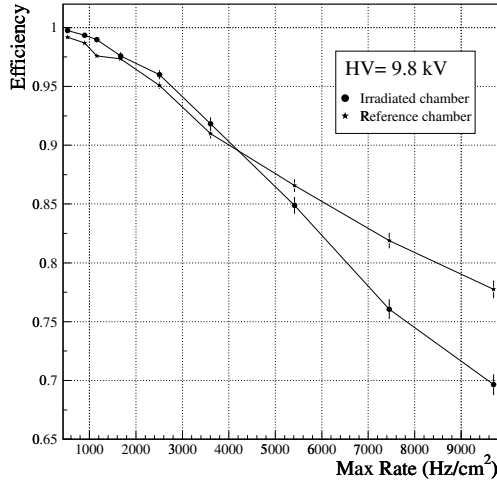


Figure 45 Efficiency as a function of rate for irradiated chamber and reference chamber. The integrated charge density collected by the irradiated chamber is about 0.2 C/cm^2 (see text).

to the observed hits, taking into account the cluster size. The value measured in this way is about 30 pC .

Figure 44 summarises the GIF test during the first three months of 2001. The upper plot shows the integrated charge per cm^2 . The lower plot shows the duty cycle. This has, unfortunately, been rather poor, so that only 0.2 C/cm^2 have been accumulated so far. A first check of the performance after irradiation with this integrated charge has been performed by measuring the chamber characteristics at the CERN T11 beam. Figure 45 shows the measured efficiency as a function of rate². No difference in performance between the irradiated and the reference detector has been observed up to rates of at least 3.5 kHz/cm^2 . The total charge accumulated corresponds to about two years of operation for the detectors in region R3 and four years in region R4. At the present rate, it should be possible to collect about $0.7 - 0.8 \text{ C/cm}^2$ by the end of 2001, corresponding to about eight LHCb years with the conditions of region R3.

²The difference between the radiation load of photons, produced at the GIF, and pions, used in the test beam measurements, induces a different rate performance [3, 7].

5 Technical Design

5.1 The MWPC detector

The LHCb muon system will use Multi-Wire Proportional Chambers (MWPC) for the four regions of stations M2 and M3, for regions R3 and R4 of station M1 and for regions R1 and R2 of stations M4 and M5. The full system covered by MWPCs consists of 864 chambers and about 80,000 FE-channels. An overview of the MWPC detector is given in Table 13.

5.1.1 Detector overview and requirements

The required geometrical tolerances for the chamber construction have been determined based on GARFIELD [60] simulations, practical considerations and prototype results. For the simulations [50] a maximal tolerable variation in gas gain of $\pm 20\%$ has been assumed, and only individual parameters have been varied while the other parameters have the design value. The maximal deviations of single parameters from the design values are given in Table 14 together with the acceptable geometrical tolerances. The geometrical tolerances combine all single effects and are therefore more stringent than the maximal deviations for single parameters.

Table 14 Geometrical tolerances for the MWPCs.

Parameter	Maximal Deviation	Acceptable Tolerance
Panel Thickness		$\pm 200 \mu\text{m}$
Panel flatness	$\pm 75 \mu\text{m}$	$\pm 50 \mu\text{m}$
Gas gap size	$\pm 80 \mu\text{m}$	$\pm 70 \mu\text{m}$
Wire plane offset	$\pm 300 \mu\text{m}$	$\pm 100 \mu\text{m}$
Single wire offset	$\pm 250 \mu\text{m}$	$\pm 100 \mu\text{m}$
Wire pitch	$\pm 80 \mu\text{m}$	$\pm 40 \mu\text{m}$

5.1.2 Chamber components and design

The general design and construction is the same for all chambers and is discussed in detail in Ref. [61]. They have four separate gas gaps, each with an anode wire plane and, in regions R1 to R3, a plane of cathode pads. In Figure 46 one can see a cross

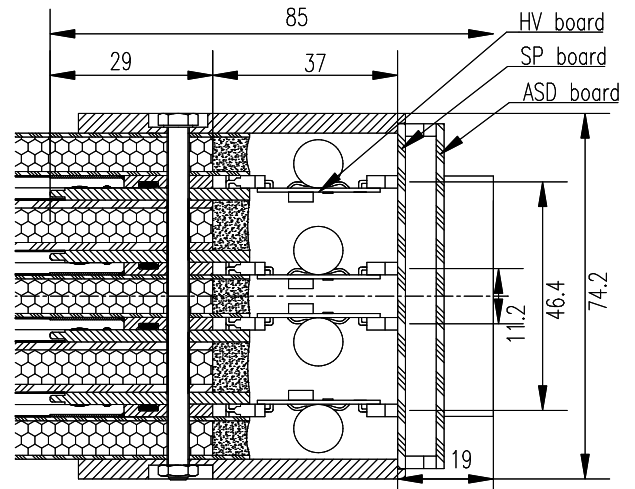


Figure 46 A cross section of the wire chambers showing the four gaps and the connection to the readout electronics.

section of one chamber where the four gas gaps are shown, together with the connection to the FE electronics.

The main components for the MWPCs are the following:

- Structural panels with FR4 laminates (total thickness $10.2 \pm 0.2 \text{ mm}$);
- Wire fixation bars with $2.40 \pm 0.08 \text{ mm}$ thickness;
- Gold-plated tungsten wires of $30 \mu\text{m}$ diameter;
- Side bars of $4.9 \pm 0.08 \text{ mm}$ on the short side of the chamber, where the gas inlets are located;
- Gap bars of $2.40 \pm 0.08 \text{ mm}$ thickness on top of the wire fixation bars to close the gas gap over the long side of the chamber;
- Spacers along the chamber border to ensure precision of the gas gap of $5.00 \pm 0.05 \text{ mm}$.

5.1.2.1 Panels

The panels are the basis of the chamber mechanical structure. The requirement on the flatness of

Table 13 Summary table of the MWPC detector

	Station M1	Station M2	Station M3	Station M4	Station M5	Sum
Chambers Region R1						
Number of Chambers		12	12	12	12	48
Sensitive area (cm ²)		30×25	32.4×27	34.8×29	37.1×30.9	
Anode channels		96	96			2304
Wire pad size (mm ²)		6.3×250	6.7×270			
Number of wires		800	864	928	992	4.4×10 ⁴
Cathode channels		128	128	192	192	7680
Cathode pad size (mm ²)		37.5×31.3	40.5×33.7	29×36	31×39	
Chambers Region R2						
Number of Chambers		24	24	24	24	96
sensitive area (cm ²)		60×25	64.8×27	69.5×29	74.3×30.9	
Anode channels		96	96			4608
Wire pad size (mm ²)		12.5×250	13.5×270			
Number of wires		1600	1728	1856	1984	1.7×10 ⁵
Cathode channels		128	64	96	96	9216
Cathode pad size (mm ²)		75.0×31.3	162×33.7	58×72	62×77	
Chambers Region R3						
Number of Chambers	48	48	48			144
Sensitive area (cm ²)	96×20	120×25	129.6×27			
Number of wires	2560	3200	3456			4.4×10 ⁵
Cathode channels	192	192	192			27648
Cathode pad size (mm ²)	20×100	25×125	27×135			
Chambers Region R4						
Number of Chambers	192	192	192			576
sensitive area (cm ²)	96×20	120×25	129.6×27			
Anode channels	48	48	48			27648
Wire pad size (mm ²)	40×200	50×250	54×270			
Number of wires	2560	3200	3456			1.8×10 ⁶

$\pm 50\mu\text{m}$ is of critical importance for gas gain uniformity and consequently for the width of the operational plateau.

A panel consists of two copper clad FR4 (fire-resistant fibreglass epoxy) laminates, interleaved with a core. For the core various materials are under investigation. Besides the panels based on Nomex honeycomb, other materials like polyurethanic foam and Chempir [62] are under consideration. The choice for the core material is still to be made.

Honeycomb panels: It has been demonstrated in several prototypes that Nomex honeycomb panels with the required specification can

be produced. Therefore, FR4-laminates of 1.6 mm (0.8 mm) thickness with $\simeq 30\mu\text{m}$ copper, interleaved with 7 mm (8.6 mm) honeycomb are the baseline panel for the chamber construction. However, the production of such panels is rather time consuming and expensive. Therefore other solutions like the one based on polyurethanic foam or chempir core are under investigation.

Polyurethanic foam panels: The panels are composed of two sheets of FR4 filled with a rigid polyurethane foam, which is the result of a chemical reaction between two components: the polyol and the isocyanate. A panel of $20\times 20\times 1\text{ cm}^3$ with a rigid polyurethane foam (ESADUR120) has

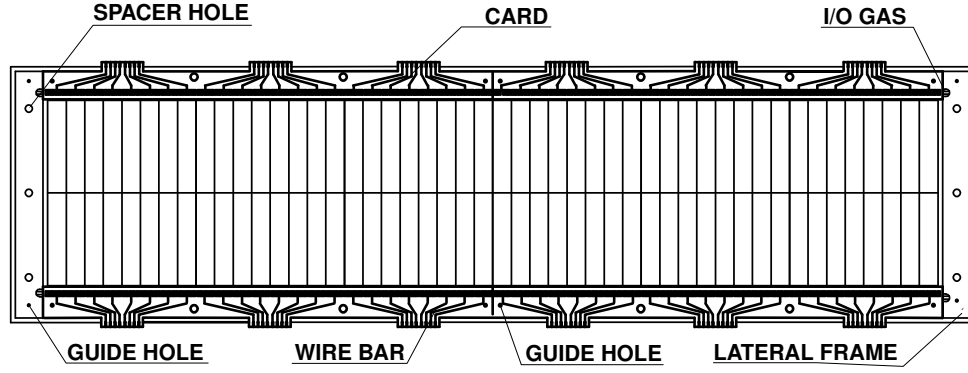


Figure 47 Cathode structure and chamber components for an MWPC designed for region R3.

been produced using a non precise mould, showing a very high mechanical rigidity. Small and large precision moulds of $30 \times 30 \text{ cm}^2$ and $40 \times 150 \text{ cm}^2$ are under preparation to test the requested planarity and to verify the construction sequence. The moulds have to sustain a pressure of 5 kg/cm^2 due to the expansion of the foam.

Chempir panels: Similar to the other options, the panels are composed of two sheets of FR4, in this case interleaved with a polyisocyanurate core (Chempir Core 75 [62]), which can be rectified with very high precision ($\pm 10 \mu\text{m}$) at low cost. First tests have shown that such panels provide the required rigidity. The long term behaviour is under investigation.

5.1.2.2 Cathode planes

Detailed PSPICE [63] simulations have been carried out in order to minimise the capacitance and the cross talk induced by the readout traces running under the cathode pads [16] (see also Section 4.1). The studies showed that, in order to minimise the cathode capacitance, it is preferable to have two panels with cathode pads on both sides, instead of having four panels with cathode pads on only one side (see Figure 48). Moreover, such a configuration provides better shielding to the cathodes, as they are always surrounded by detector ground.

In all regions the cross talk can be kept below the 5% level, which is within the requirements for the muon system.

In region R3 the cathode pads can be accessed from the top and bottom of the chambers (see Fig-

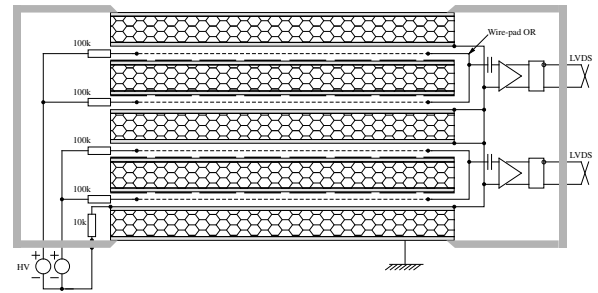


Figure 48 Cross section of the chamber with a schematic of the readout chain.

ure 47). This avoids the use of a double layer board in PCB technology for the cathode structure in this regions, which are difficult to produce in the required dimensions of $140 \times 35 \text{ cm}^2$. First investigations of using a milling machine to realise the cathode structure are promising, but a full test has still to be carried out. Guard traces of 0.5 mm width between the cathode pads are foreseen to minimize the cross talk. The width of the insulating surface between the pads and the guard trace should not exceed 0.4 mm to avoid problems of charge up at high rates.

In regions R1 and R2 the cathodes have a chessboard structure, as indicated in Figure 49. Only a fraction of the cathode pads of region R1 and R2 can be accessed from the border of the chamber. Most of the pads have to be read by traces running on the bottom of the cathode board to the edge of the chamber. A double sided PCB will be used to implement this structure. Special care has to be taken to minimize the capaci-

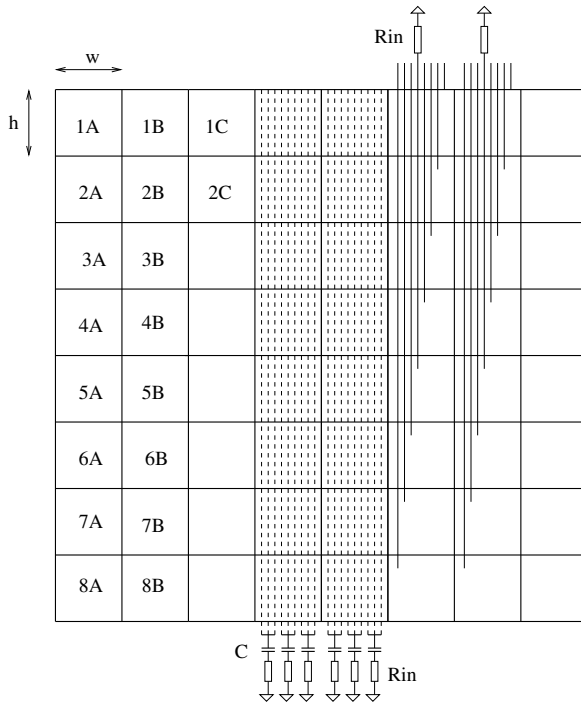


Figure 49 Cathode- and wire-pad structure and read-out.

tance between the readout traces and the pads. The readout traces of 0.25 mm width are separated by 0.25 mm ground traces with a gap of 0.25 mm. The pads are connected through metallized holes to the readout traces.

5.1.2.3 Wire fixation bars and gap bars

On the long sides of the panels wire fixation bars are glued. The bars have a thickness of 2.4 mm, 0.1 mm less than the anode-cathode distance. They will be made according to standard printed circuit board technology. A pattern of finger pads is etched on the bars which will be used for soldering the wires. They are interconnected in groups. The grouping of wires is determined in the case of anode wire readout by the required granularity in the x -coordinate. In order to minimize the cross talk in the case of cathode pad readout, wires are grouped together according to the x -dimension of the cathode pads.

The wire fixation bars and the other frames will be correctly positioned on the panels using a set of guide posts which are inserted into the

frames. Cylindrical spacers, (5.00 ± 0.05) mm thick, guarantee the exact gap along the perimeter of the chamber. In this case the wire fixation bars and the other frames can have standard tolerances. The side bars have additional holes for the gas inlets/outlets. This solution is both less expensive and does not require accurate glueing to maintain the required tolerances.

5.1.2.4 Wire

The total number of wires in the chambers is about 2.5×10^6 , with a total wire length of about 1200 km. Therefore, a great deal of effort has been expended to develop an efficient and reliable scheme of winding and attaching wires, as discussed in section 5.1.3.

Gold-plated tungsten wire of 30 μ m diameter has been chosen for the chambers. Measurements have shown a linear dependence of the elongation on the applied weight up to 140 g. At the wire spacing of 1.5 mm, a free wire length of 30 cm and with nominal HV of 3.15 kV, the wires become electrostatically unstable if their tension is below 30 g. The chosen wire tension is (60 ± 10) g, controlled with a standard wire tensioner during wiring.

5.1.3 Chamber construction and tooling

Two possible ways to build the chambers with the above parameters have been considered. One is producing panels with wires on both sides (double gaps), the other with wires on one side only (mono-gaps). The two options can be seen in the drawing of Figure 50. Both methods have their merits. The main advantage of mono gaps is that the panels can be handled more easily during the detector construction. Moreover, in case of incurable problems during the glueing or soldering process only one gap would be lost. Double gap wiring, on the other hand, is better adapted to the cathode design, which is based on two double gaps instead of four single gaps, as pointed out in section 5.1.2.2. All prototypes have been build so far with a double gap structure. Hence, this design is also backed up by experience and positive results from tests. The final choice of the construction method has still to be made.

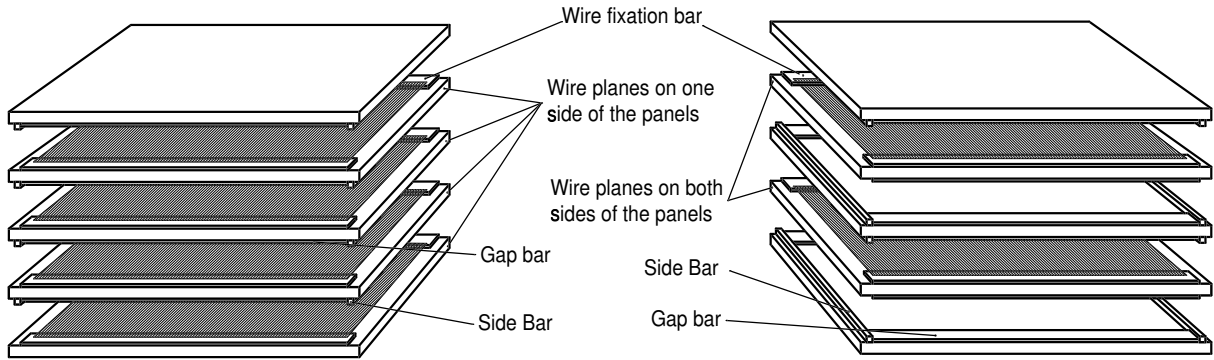


Figure 50 Exploded view of chambers ready to be assembled. The left side shows panels with single sided wires and the right side panels with wires on both sides. The position of the various bars is indicated as well.

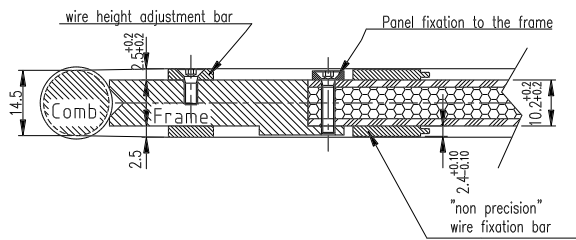


Figure 51 Schematic drawing of the frame cross section.

Prior to the wiring a panel is assembled in the following way:

- the side bars are inserted in the guide posts and glued to the panels;
- the wire fixation bars are also positioned using the guide posts (these are especially needed if the bars are made of several pieces due to the chamber length) and glued to the panels;
- the gap bars on top of the wire fixation bars are glued to the panels.

The final assembly can be seen in Figure 50.

5.1.3.1 Wiring

Double sided wiring is done by winding directly around the honeycomb panels. In this way symmetrically loaded panels with wire planes on both sides are produced. The panel is fixed to a rigid frame where the positioning combs are mounted

(see Figures 51 and 52). To achieve the required precision, the wire spacing is determined by the combs while the anode to cathode distance is given by the adjustment bars.

- *Grooved combs:* The grooved combs have a diameter of 15 mm and are machined in a precise way to have a pitch of 1.5 mm, which determines the wire spacing. The groove depth is of about 0.25 mm, hence the inner diameter of the combs is smaller than the distance between the two wire planes.
- *Adjustment bars:* The wire height with respect to the cathode-plane is adjusted by precision bars mounted to the frame. On one side the bars are fixed, and on the other, they can be adjusted depending on the panel thickness to achieve a wire to cathode plane distance of 2.5 mm.

The wiring procedure was tested for a 700 mm long detector panel, and the average pitch measured was 1.5 mm with a root mean square of $14\mu\text{m}$. This precision is well within the specifications of $\pm 40\mu\text{m}$. For bigger chambers, the panel should be fixed to the frame along its long side every 500 mm to avoid differences in sag between the panel and the frame.

The production of panels with wires on a single side could be done using the same winding machine, but with a different frame. Based on a calculation, no deflection of the panels is expected due to the asymmetric load of 60 g per wire. Tests done



Figure 52 Wiring of a panel mounted to the aluminium frame.

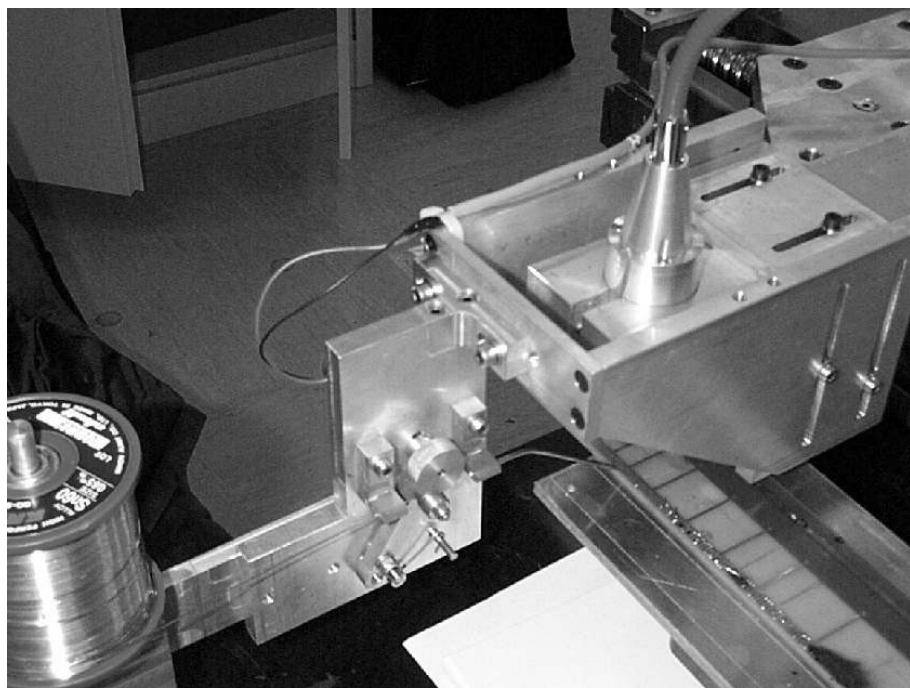


Figure 53 The laser soldering and the solder dispenser.

on both deflection and torsion of a panel wired in this way confirmed this. The wiring guidelines are the same as mentioned for doubled sided wiring.

5.1.3.2 Glueing

Once a frame is wired, it can be removed from the winding machine to have the wires glued and soldered. This separates the three important steps of the chamber construction and allows a parallel production.

The wires are glued to the wire fixation bars before soldering. This procedure guarantees that the wires are kept in place with a fixed height with respect to the cathode plane. The gluing also keeps the wire tension to its nominal value. Standard epoxy glue like Adekit A145 [61] polymerizing in about 24 hours at room temperature is foreseen for the wire glueing.

5.1.3.3 Soldering

One of the cleanest soldering methods is the use of a laser beam. Due to the large number of soldering points in the construction of the MWPCs ($\simeq 5 \times 10^6$), the use of an automated and reliable method is desirable. A test was made with an automatic soldering station [61] (see figure 53).

The result of the test was very clean and the control of local heat was very good. The wire suffers less heat stress with respect to conventional techniques.

Using a conservative value of 3 s for the soldering of one wire and assuming that the final setup will be equipped with two laser heads, the time evaluated for the wire soldering of all MWPCs would be 2100 hours. This number does not include the time spent for the layer setting up and for the required checks, which is proportional to the number of chambers.

5.1.3.4 Final assembly

To proceed with the final assembly of the chamber, five panels should be ready: two double sided wired panels and three ground panels (or four single sided wired panels and one ground panel). All the panels are already equipped with side bars, wire fixation bars and gap bars. The cylindrical

precision spacers are inserted in the holes around the chamber and the panels are assembled making use of the guide posts at the four corners, as indicated in Figure 54. For the final closing of the chambers the five panels are kept together with screws. In the side bars, the gas inlets/outlets for each gap are mounted. The gas tightness is obtained by gluing the five panels together with epoxy glue.

5.1.4 HV and FE interfaces

Several constraints determine the available space for and the location of the the HV-interface and the readout electronics:

- Density of channels in inner regions;
- Space problems due to the proximity to the beam pipe in region R1;
- Connectivity requirements due to logic ORs on FE-electronics cards.

As a consequence, the border region of the chambers have the space requirements summarized in Table 15. These parameters ensure sufficient space between the chambers for the routing of cables for readout, high and low voltage, and gas pipes. A detailed study of these combinations for the various stations and regions lead to the scheme shown in Figure 46.

Table 15 Space requirements around the sensitive area to the border of the chamber.

Space requirements	
Top with anode/cathode readout	85 mm
Bottom with cathode readout	70 mm
Bottom with no readout	35 mm
Side with no readout	50 mm
Side with cathode readout	60 mm

5.1.4.1 HV interface

The HV connection is realized by interface cards which carry the loading resistors and the decoupling capacitors. The HV boards will also carry a large amount of ground connections on the other

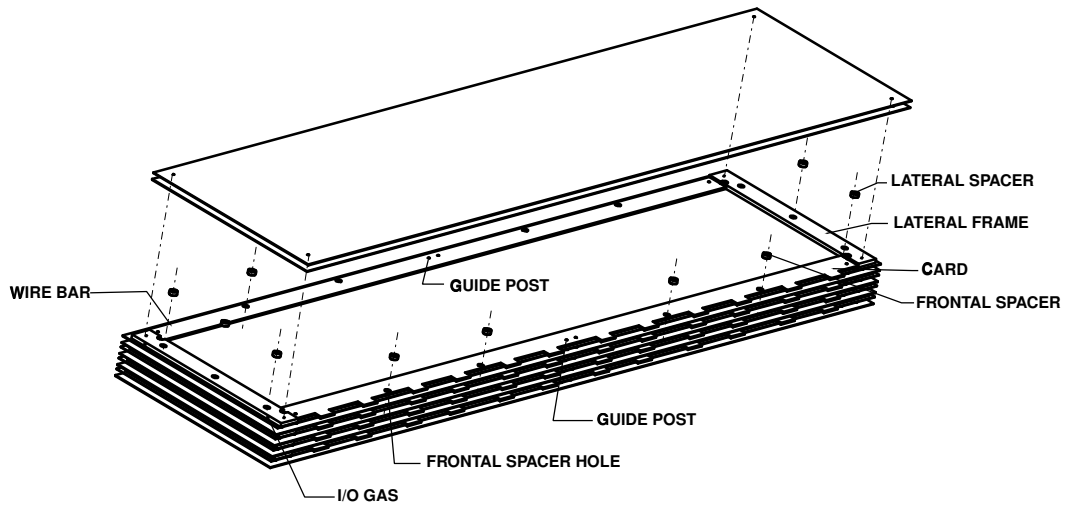


Figure 54 A sketch of the MWPC assembly.

side to reduce pickup noise. Samples of these cards will be tested in real configurations with existing wire chamber prototypes to check the validity of this solution. The value of the decoupling capacitor should be much larger than the capacitance of the group of wires connected to it. This ensures a low impedance to ground or to the amplifier. A value of 0.5-1 nF satisfies this condition in all cases.

The upper limit on the HV loading resistor is given by the maximal allowed voltage drop, while the lower limit is set by the introduced parallel noise. The choice for the resistors is therefore 100 k Ω .

5.1.4.2 FE interface

The FE electronics will be implemented in two stages; the first stage as a spark protection board (SPB) and the second as the Amplifier-Shaper-Discriminator (ASD) chip board (ACB). The ACB is mounted as shown in Figure 46 on the SPB. This design keeps the distance the signals must propagate from the wire pads and cathode pads small. The dimensions for these boards are given by the thickness of the chamber (70 mm) and the maximal allowed space between adjacent boards on the chamber (50 mm). The 50 mm are determined by region R1, where the highest granularity of readout channels occurs. Each board receives the signals

of 8 readout channels from each double gap, thus a total of 16 channels.

The SPB will be a 50×70 mm² two layer board that contains a system of resistors and diodes for each channel designed to limit the voltage in the event of a spark or discharge. The design uses a two stage double diode scheme. This design fully protects the readout channels.

The ACB is a 50×70 mm² four layer PCB containing two ASD chips, for which the preferred solution is the CARIOCA chip (see Section 4.1), and the chip, which provides some basic logic and diagnostic functions (see Section 5.3.2).

5.1.5 Quality control and testing

Quality tests of the individual chamber components and for the assembled chamber are foreseen. The key items to be checked during chamber construction are the following:

- *Panel planarity*, which can be verified with a proper apparatus;
- *Wire quality*, with optical inspection and tests of mechanical properties on samples;
- *Wire trimming*, to check that the wire is cut sufficiently close to the solder;
- *Soldering quality*, to check the electrical continuity after the semi-automatic soldering and trimming of the wires.

- *Wire tension checks*, using an automated resonance method;
- *Wire positioning*, to be verified on a small set of points on each wire plane;
- *Gas tightness*, to be verified using standard procedures such as applying a small under-pressure to the chamber in an He-bag and looking for possible leaks;
- *HV training and tests*. This test will be the most important as it will certify the quality of the production from each centre. A “good” chamber should be able to sustain a voltage well into the operational plateau for a minimum number of hours, after training with an automated procedure has been performed.

Afterwards the chamber will be inspected for uniformity in its response. A very efficient method is to perform a scan of the wire planes with a source, checking that the mean value and the standard deviation of the measured current is within specifications over the chamber. In addition, a complete test with cosmic rays to determine the efficiency plateau and time resolution will be performed. As far as possible, these tests will be done with the final electronics.

Important information about individual components and the final chamber will be stored in a database. This allows to retrieve at any time the results of all quality control measurements and will aid in understanding possible problems.

5.2 The RPC detector

The prototype tests demonstrate that the requirements of efficiency, redundancy, rate capability and cluster size are optimally met by a solution based on chambers made of two identical single-gap RPCs, each with its own strip readout plane (Figure 55). This allows two independent detector layers per station. The two strip planes are read out independently and the signals from corresponding strips in the two layers are logically OR-ed. The two gaps of the RPC are connected to independent HV supplies. This allows the adjustment of the HV for slightly different plateau voltages. In addition

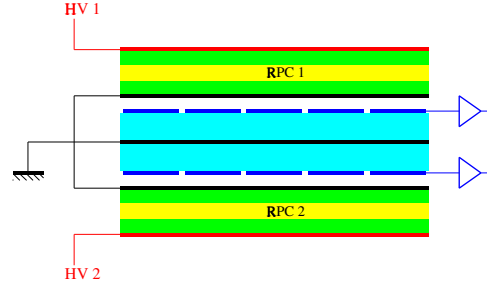


Figure 55 Schematic layout of the chamber with two independent single gap RPCs.

one of the gaps could be switched off, if necessary, at the price of a small reduction of the overall efficiency.

5.2.1 Detector overview and requirements

The main parameters of the RPC system are summarised in Table 16. The minimal number of chamber types per station is obtained with chamber sizes having an active area of $139 \times 29 \text{ cm}^2$ and $148 \times 31 \text{ cm}^2$ in station M4 and M5, respectively. In region R4 the strips have full length (about 30 cm), with the read out at one end. In region R3 they are split in the middle and are read out at both ends. In both cases the electronics boards are installed on the chamber horizontal sides. The strip width in station M4 (M5) is 5.6(6.0)cm, with a pitch of 5.8(6.2)cm and interleaved with narrow ground strips of 0.5 mm.

Maximum standardisation has been an important goal in the detector design:

- the dimensions of the RPC gaps are the same everywhere;
- chambers of region R3 and R4 in the same station have the same sensitive area but differ in the vertical strip dimension, which in region R3 is half that in region R4;
- the sensitive area (different in station M4 and M5) is defined by the strip readout and by the graphite layer (see later);

Uniform operation within each chamber requires controlling the planarity of the gas gaps at the level of $\pm 10 \mu\text{m}$.

Table 16 Main parameters of the LHCb muon system in the regions equipped with RPCs. Where relevant the horizontal dimension, i.e. the one in the bending plane, is given first.

Physical quantities:	Region R3		Region R4	
	Station M4	Station M5	Station M4	Station M5
Detector surface (m ²)	19.3	22.1	77.4	88.3
Horizontal dimension (cm)	139	149	278	297
Vertical dimension (cm)	116	124	232	248
Chamber sensitive area (cm ²)	139×29	148.5×30.9	139×29	148.5×30.9
Channel size (cm ²)	5.8×14.5	6.2×15.5	5.8×29.0	6.2×30.9
Maximal rate (Hz/cm ²)	750	650	250	190
Number of chambers	48	48	192	192
Total	480			
Physical channels per chamber	48×2	48×2	24×2	24×2
Total	27648			

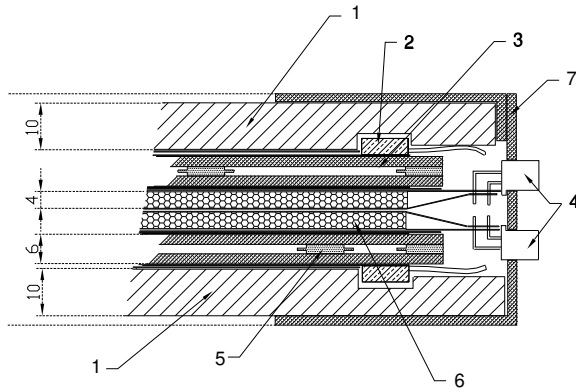


Figure 56 Chamber cross section: Al-polystyrene external panels (1); HV contacts (2); RPC detectors (3); multi-pin connectors (4); polycarbonate spacers (5); strip planes (6); aluminium external profiles (7).

5.2.2 Chamber design

A detailed cross section of the basic chamber is shown in Figure 56. The chamber is made by two independent RPC detectors, each with its own readout strip plane. All components are supported and kept together by means of two support panels which also provide the necessary rigidity to the chamber. The panels are made from polystyrene foam (density 40 kg/m³) sandwiched between two aluminium sheets (0.5 mm thick) and glued with epoxy adhesive. The overall thickness of each panel will be about 10 mm. These panels

are rigidly connected on the sides by shaped aluminium profiles, 0.5 mm thick. Since it is important that the panels provide an adequate and uniform pressure on the detector assembly, the possibility to have them pre-loaded is under consideration. This could be obtained, for example, by glueing them on a template in such a way as to have a non-zero sagitta. Where possible the use of standard commercial mechanical items will be pursued.

The gas gap of each RPC detector is made of two bakelite plates, 2 mm thick, and laminated with a thin melamine foil on the surface in contact with the gas. The purpose of the melamine layer is to improve the surface quality of the bakelite plates over that of purely phenolic plates [11]. The choice of the bakelite volume resistivity is driven by considerations about rate capability. As mentioned in the previous section, satisfactory results have been obtained with volume resistivities slightly less than 10¹⁰ Ωcm. Hence, bakelite plates with volume resistivities in the range of $(8 \pm 2) \times 10^9$ Ωcm will be used. On the outer surface of the gaps, the bakelite is painted with a conductive graphite layer (resistivity about 100 kΩ/square). The graphite layer distributes the HV and ground on the bakelite, and is electrically insulated by means of a 200 μm thick Polyethylene-Teraphtalate (PET) film glued onto the graphite itself by a “hot melt” process.

To ensure a precise and constant gap width, the

bakelite plates are kept parallel by polycarbonate spacers, 10mm in diameter, and 2.00 ± 0.01 mm in height. These are positioned within each gap to form a square array with a $10 \times 10 \text{ cm}^2$ basic repeating cell. The topology for spacer positioning is different in the two RPCs of a chamber to avoid correlating the insensitive areas. A polycarbonate rectangular frame, 7mm wide and of the same height and tolerances as the spacers, is used to close the gap at the edges. The circulation of the gas is insured by the four gas inlets/outlets placed at the four corners of the detector. They are also made of polycarbonate and are 3mm in diameter. All these parts (bakelite plates, spacers, frame, gas connections) are glued together using epoxy adhesives.

The two strip readout planes are located on the inner part of the chamber (Figure 56). These planes are made by a dielectric substrate (polystyrene foam 3.8mm thick, relative permittivity $\epsilon_r = 1.4$), sandwiched and glued between two copper foils. One of the foils constitutes the ground, the other is milled on a special machine to form the strips. The 6 cm wide strips will have a characteristic impedance of about 13Ω . The signals will be brought outside to the front-end electronics via standard multi-pin connectors.

An alternative scheme is under investigation, in which the strip readout plane is etched on a PC board made of a 0.8 mm thick FR4 layer. The PCB would then be glued on the polystyrene foam substrate. The basic strip module will be as shown in Figure 57. This solution would additionally simplify the construction by avoiding interconnecting cables from the strips to the external connector. Its feasibility, in terms of cost and electrical properties, has to be checked.

An exploded view of the RPC chamber is shown in Figure 58.

5.2.2.1 Oil treatment

It is well known that depositing a thin layer of linseed oil on the bakelite surface has the effect of reducing the noise and the dark current of the RPC. This occurs partly because linseed oil has a larger conductivity than the bakelite.

The treatment of the bakelite plates with lin-

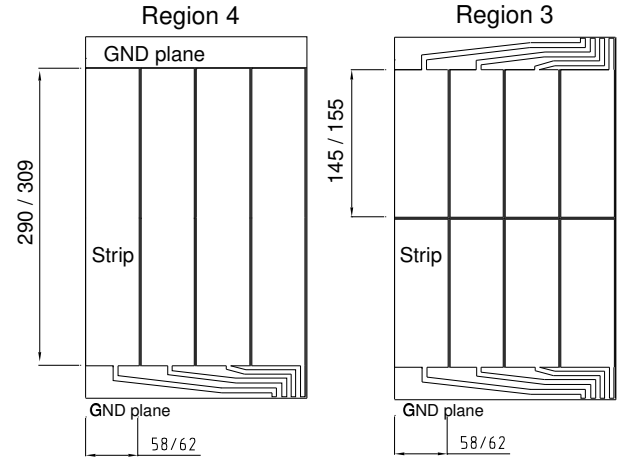


Figure 57 Printed circuit for strip planes: basic modules for R3 and R4; dimensions in mm (the first indicated is for M4, the second for M5).

seed oil was recently much debated in the RPC community. This was triggered by the problems faced by BABAR [64], which were attributed to high-temperature operation coupled with improper oil polymerisation. In a “sticky” layer the oil can form “stalagmites” because of electrostatic attraction, that can eventually short-circuit the gap and inhibit proper operation of the RPC.

Since the oil is applied after the gap is assembled and sealed, quality control of the layer is very difficult. Therefore it would be preferable to avoid the oil treatment, which would also simplify the construction of the detectors. However, this will unavoidably increase both dark currents and noise.

The increased dark current will result in extra ageing. In order to control this effect, the dark current should be kept below the current due to the flux of real particles traversing the detector (see Section 4.2.3). Considering an increased ageing of 25% for chambers in Region R3 as acceptable, RPCs without oil treatment will be a viable solution if the dark current density can be kept below 3 nA/cm^2 ($30 \mu\text{A/m}^2$). Assuming that the average charge of the noise hits is 30 pC, this corresponds to a maximum noise rate of 100 Hz/cm^2 per RPC gap, which is well below the rate acceptable by the trigger (see Figure 16).

Preliminary studies performed by the CMS collaboration with non-oiled chambers [65] have shown that with the melamine treatment of the

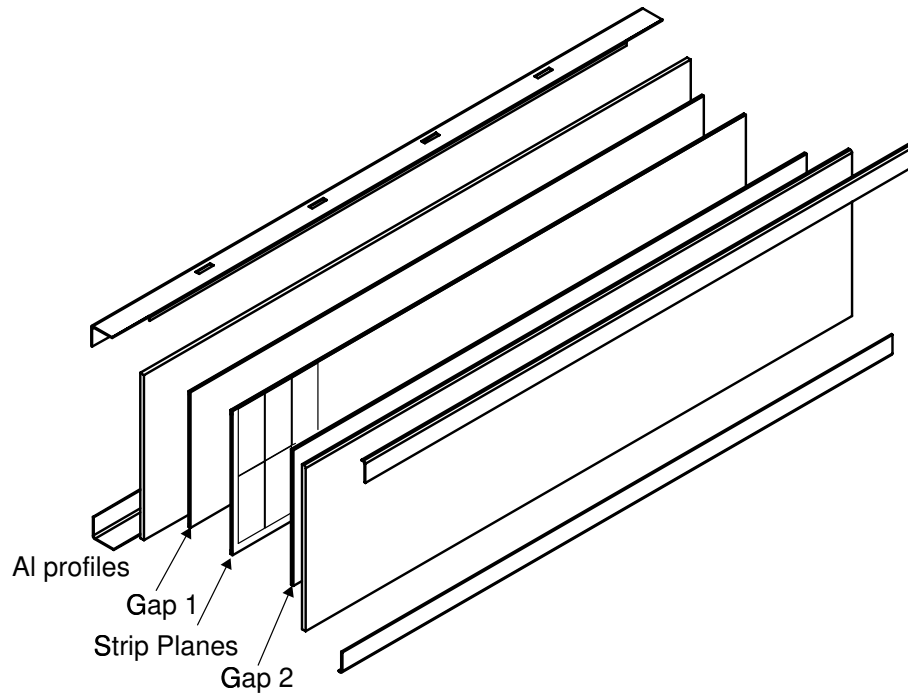


Figure 58 Exploded view of the RPC chamber.

bakelite plates it is possible to reach full efficiency keeping the noise level below 50 Hz/cm².

A test of RPCs without linseed oil treatment is scheduled for the summer of 2001, in order to definitely assess if these detectors can be used in the experiment.

5.2.3 Chamber construction

The industrial capabilities for producing RPC detectors is by now well established. The total amount of melamine laminated bakelite needed for the LHCb RPCs is about 1000 m² and can be produced industrially in a few weeks. Since the commercial plates come in rather large dimensions (about 3.2×1.3 m²) they will have to be cut to the required size. The possibility of having the shaping performed by the firm producing the bakelite is under investigation.

Once the bakelite plates are ready, the whole number of gaps required by LHCb can be produced in a few months. The gaps will be produced following the LHCb specifications, using the same techniques detailed in Refs. [10, 11]. The specifications refer to the size of the gaps and of the

graphite paint defining the active area, the positioning of the spacers and the linseed oil treatment (if applied).

5.2.4 Quality control and testing

The individual chamber components, as well as the assembled chambers, will undergo some basic quality control and tests.

Quality control of the bakelite plates is performed at the factory by measuring the volume resistivity and the surface roughness at several places on the plates³. Plates not satisfying the specifications will be rejected, the others will be grouped according to the measured resistivity values. A second selection step will be performed in Rome II, looking in particular for possible surface damage (scratches) that could have occurred in the storage and shipping phase. Here the matching of the two plates for a given gap will also be made, which could possibly require a new measurement of the

³The CMS group developed a special tool for a multi-point resistivity measurements [66]; we are investigating the possibility to use the same tool or a similar one better specified for our case.

resistivity.

The gap production will be closely monitored at the factory by technicians and physicists belonging to the responsible institutes. In the case the oil treatment will be necessary, a procedure has to be defined to control its quality. A possibility would be to perform a routine check by opening up and inspecting a fraction of the gas gaps (e.g. one in ten) during the production phase.

The produced gaps have to be checked for gas tightness and their capability to stand high voltages. This will be done by the producers using Ar or N₂.

Pairs of gaps satisfying the basic quality controls mentioned above will be used to produce chambers. This assembly phase will take place in Rome II and Firenze. The quality of the gaps delivered by the producing firm will be checked at first by performing an automated I-V measurement, in parallel for about ten gaps. For this purpose, the gaps will be equipped with connectors to distribute the high voltage and monitor the dark current. The ten gaps will be flushed with gas at a rate of about 3 l/h for about 15 hours; since the gap volume is about 1 litre, this will insure that at least four volumes are changed during the flushing procedure. Gaps with dark currents that are too large will be rejected. The tolerances to accept or reject gaps will be defined with the next prototypes. These quality checks will start as soon as the first gaps will be produced in order to assure a prompt feedback to the factory in case of problems.

Chambers with two good gaps will be equipped with strip planes and completely assembled. At this point the chambers will be ready for the final tests with cosmic rays, using the final electronics. The test should provide the basic performance parameters of the chambers, such as the plateau curve, efficiency and cluster size, and the degree of uniformity over the chamber. For this purpose a tracking trigger telescope will be designed, most probably also made of RPCs.

The successfully tested chambers will then be shipped to CERN where they will be stored and flushed with nitrogen until installation in the experiment.

Each chamber/gap will be identified by a bar code which will allow to retrieve all the impor-

tant facts about the chamber/gap, the history and results of all the measurements done by the companies and in the institute laboratories.

5.2.5 Front-end electronics

As discussed in Section 4.2.2.2, the CMS BiCMOS electronics satisfies our basic requirements and has been chosen as baseline for the RPC readout. Depending on the availability, we plan to test also the ASDQ [47] and CARIOCA [52] chips developed for the MWPC, which potentially have some nice feature that could allow operation of RPCs at lower gain.

The Front-end boards (FEB) will be mounted on the upper side of the chamber (in region R4) or on the upper and lower sides (in region R3), and will read out 16 channels, eight channels in the first layer of the RPC and eight in the second layer. Three boards will be necessary to completely readout a chamber in region R4, and six in region R3. A first prototype with eight channels only has been developed for the test chambers (Figure 36). The second prototype, presently under development, should be close to the final form, housing two chips and the connectors to take the signal out of the chambers. The operational requirements of the CMS readout chip are a LV supply of +5 V and a variable voltage to adjust the threshold. The power and threshold setting should be provided via ECS.

The structure of the FEBs has not yet been frozen. The Front-End architecture [67] requires that part of the logic gates are moved on the detector. This is discussed in detail in section 5.3.2.

5.3 Readout electronics

5.3.1 Overview

The main task of the electronics is to prepare the information needed by the L0 muon trigger [36]. This corresponds to:

- Formation of around 26,000 logical channel signals, starting from the around 120,000 physical channels, corresponding to the outputs from the ASD chips.

- Each logical-channel signal is tagged with the number of the bunch crossing (BX) to which it belongs (BX identifier).

As far as possible, the first step should be performed on the chambers in order to minimise the number of LVDS links exiting the detector.

The second step requires a time alignment of channels. This is necessary because signals from different channels take different paths before being sent to the L0 pipelines and tagged with their BX identifiers. Moreover, each front-end channel has a time behaviour that depends on the read-out scheme and the chamber operating conditions. Signals have a width, including tails, comparable to the BX cycle (see Section 4.1). Correct time alignment is therefore necessary to avoid inefficiencies.

On-chamber formation of logical channels from physical channels is achieved using a custom integrated circuit for Diagnostics, time Alignment and LOGics (DIALOG). The DIALOG chip also allows programming of a delay for each single input channel, and contains features useful for system set-up, monitoring and debugging (see section 5.3.2). The detector layout and the logical channel distribution allow generation of logical channels in the front-end boards (FEB) in a large part of the system. However, in regions R3 and R4 of stations M2 to M5 and region R2 of stations M4 and M5, physical channels from different FE-boards and chambers must be combined, and a simple local solution is not feasible [67]. In this case, logical channel formation requires a further step of logical operations, performed in the intermediate boards (IB), discussed in section 5.3.3.

Once generated, the logical channels are sent to the Off-Detector Electronics (ODE), where they are assigned the corresponding BX identifier and dispatched to the L0 trigger. The ODE contains also the L0 pipelines, the L1 buffers and the DAQ interface (Section 5.3.6). Both the intermediate boards and the ODE boards are located inside the cavern, on either side of the detector.

The Experiment Control System (ECS) of the muon detector is a distributed system based on CAN bus [68]. The ECS performs basic control and monitoring of the ODE boards and controls the

Table 17 Total number of units in the system

Item	Number required
Front-end boards	7536
8-channel ASD chips	15072
DIALOG chips	7536
Service boards	144
Service board crates	12
Intermediate boards	168
Intermediate board crates	12
SYNC chips	4032
ODE boards	168
ODE board crates	12
Data-concentrator boards	12

Table 18 L0 and L1 parameters for LHCb FE electronics

L0	
Maximum rate	1.1 Mhz
Latency	4.0 μ s
Consecutive triggers	Max. 16
Derandomiser depth	16 events
Derandomiser readout time	900 ns
L1	
Rate	40–100 kHz
Buffer size (latency)	1927 events
Derandomiser buffer	Min. 15 events

FEBs through specially designed Service boards (SB) (see section 5.3.5). Further technical details of the muon architecture are found in Ref. [69] and [67]. A simplified scheme of the muon architecture is shown in Figure 59.

Table 17 gives a summary of the total number of units in the system. The Level-0 and Level-1 parameters, defined in [24], are summarized in Table 18. These tables will be referred to in the following sections.

5.3.2 Front-end boards

The on-chamber electronics is based on a two-stage scheme. The main functionalities are performed by two chips.

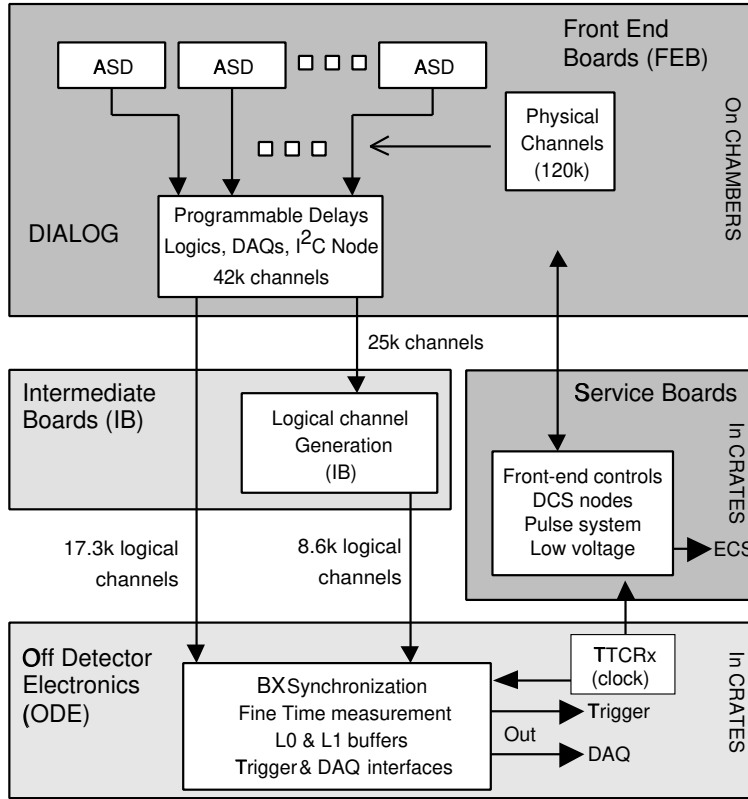


Figure 59 Simplified scheme of Muon Architecture.

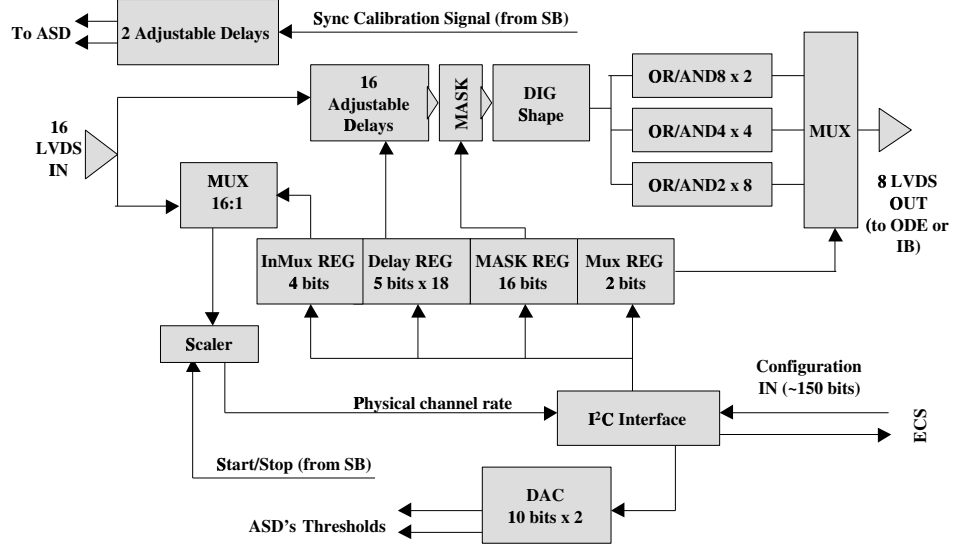


Figure 60 DIALOG chip schematic.

5.3.2.1 ASD chip

The first stage consists of the Amplifier-Shaper-Discriminator (ASD) chip. The characteristics of these chips are described in Sections 4.1.1 and 4.2.1. This stage outputs digital signals using the LVDS standard. The signals have a pulse width of 50 ± 10 ns, depending on the shape of the signals before the discriminator. Moreover, the ASDQ and CARIOCA chips optionally provide digital signals with a length proportional to the pulseheight of the chamber signal. This can be used for testing and monitoring purposes. Each ASD chip integrates eight channels.

5.3.2.2 DIALOG chip

The second stage is the DIALOG chip, described in detail in Ref. [70]. Each DIALOG chip deals with sixteen physical channels. It processes the digital outputs of the first stage as illustrated in Figure 60.

Signals enter the programmable delays (one per signal), where they can be delayed from 0 to 25 ns in steps of 1.5 ns. Physical channels can be masked, in order to make them individually accessible through the logical-channel readout. Signal arrival times are measured in the ODE boards at the end of the chain.

The signals in the DIALOG chip are shaped to a fixed width less than 25 ns. Depending on the specific position of physical channels in the detector, the signals are combined within the same detector layer according to the logical channel size, and with the corresponding signals in the other detector layer.

Individual physical channels can be examined and the number of accumulated hits can be monitored via a dedicated counter. The circuit is accessed via the ECS, which takes care of configuration and programming. DIALOG also contains two 10 bit DACs for setting the thresholds of two ASD chips.

A single front-end board (FEB) deals with 16 physical channels. It consists of two ASD chips and one DIALOG chip. Each board can output a maximum of eight logical channels. Depending on the local topology, eight, four or two outputs are used. The digital outputs of variable pulse width

Table 19 Number of IBs in each of the five half stations. The number of Input/Output signals per board are given in brackets.

	M1	M2-M3	M4-M5
R1	–	–	–
R2	–	–	12(96/28)
R3	–	24(192/56)	12(96/40)
R4	–	24(192/56)	12(96/40)

can also exit the FEBs for special tests of the chambers, and of the FEBs themselves. It is not foreseen to use this feature during normal data taking. A total of 7536 FEBs is foreseen.

5.3.3 Intermediate boards

In region R2 of stations M4 and M5 and in regions R3 and R4 of stations M2 to M5, a further level of logical combination is required, because logical channels are formed from signals which originate from different chambers. The logical combination is carried out in the intermediate boards, which are placed to the sides of the detector. Each IB allows a maximum of 192 inputs and a maximum of 64 outputs. Both the inputs and the outputs use the LVDS standard. The IBs only perform the residual logic (ORs) needed to complete the generation of logical channels in the regions mentioned.

A total of 168 IBs is foreseen. Table 19 shows the numbers on inputs and outputs per IB for the different detector regions.

5.3.4 ECS interface

A distributed control system based on a specific field-bus provides the basic control and monitoring functions of the muon detector. The architecture of this system is based on ELMB (Embedded Local Monitor Box [71]) a special CAN node board designed by the ATLAS collaboration to operate in a moderate rate environment. The ELMB is a general-purpose small plug-on module, comprising two commercial 8-bit micro-controllers and one CAN-Controller chip. The main processor is a 4 MHz micro-controller with 128 kbytes flash memory to store the program. It handles communication with the CAN controller

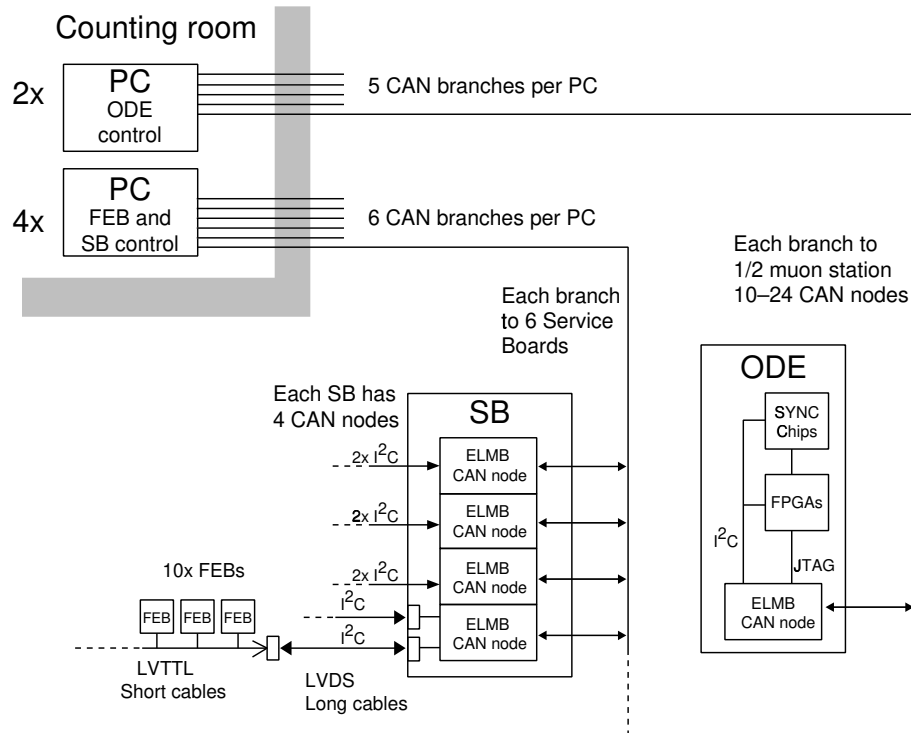


Figure 61 The ECS system for the Muon Chambers. Shown are the ECS CAN interfaces to the Service Boards (SBs) and the fanouts to the Front End Boards (FEBs). The CAN branches to the Off Detector Electronics boards (ODEs) are also shown and the internal connections within the ODE boards.

and performs user-chosen local tasks. A second smaller micro-controller acts as dedicated “watch dog”, prompting a refresh when the first micro-controller blocks, for example in the case of Single Event Upset (SEU). The ELMBs are grouped in different CAN bus branches, each branch containing up to 24 ELMB CAN nodes. There are two ECS subsystems, sketched in Figure 61, one servicing the front-end boards through the SBs and comprising 24 CAN branches, the other servicing the ODE boards via 10 CAN branches. The CAN branches are controlled by six PCs placed in the counting room. The ECS structure is given in Ref. [67].

5.3.5 Service boards

The Service Boards (SBs) are 9U size VME boards. Each SB houses four ELMB CAN nodes. Each ELMB CAN node can handle two I²C buses. These buses are extended up to 10 m (long distance branches) using an LVDS driver. At the end of the long distance branch a LVDS receiver placed

on a chamber will drive ten DIALOG chips on the FEBs with the standard LVTTTL I²C bus (short I²C branch) [67]. At start-up, a remote CAN command will trigger a local process in the ELMB that will write the registers inside the DIALOG chip. The ELMB periodically checks the consistency of the DIALOG registers. In case of errors, the ELMB send diagnostics information to the CAN-bus PC interface and correct the error. In addition, the ELMB regularly monitor the rate counters inside the DIALOG chip and return the value to the CAN-bus PC interface. There are two ways to access and control the registers of the DIALOG chip: the first requires the use of special tasks running inside the ELMB, which performs all the operations, the second involves running from the control PC, using I²C instructions. The use of the ELMB local intelligence reduces the load of the PC processors and of network communications.

Another function of the SBs is to provide the power supply generation circuitry for the FEBs. The appropriate voltage levels are generated on the service boards and transmitted to the FEBs. As the

distance between the SBs and the FEBs is 10 to 15 m, a voltage regulation facility is envisaged for the FEBs.

The SBs are also used to send and receive signals useful for front-end calibration and to monitor the correct operating conditions of the chambers and front-end electronics (e.g. temperature). A system to pulse the front-end channels for test and diagnostics is also envisaged.

The SBs are placed to either side of the detector, in the racks housing both the intermediate boards and the ODE boards. In total 144 SBs are foreseen.

5.3.6 Off-Detector Electronics boards

The ODE boards synchronise signals and dispatch them to the L0 trigger. They also contain the L0 pipelines, the L1 buffers and the DAQ interface.

A schematic of the ODE boards is shown in Figure 62. Each board receives up to 192 logical channels (LVDS) and outputs data to the L0 muon trigger and the DAQ system. The signals to the L0 muon trigger are sent directly via optical links. The data for the DAQ are multiplexed onto the Data Concentrator (DC) board (one per ODE crate), where they are formatted and sent to the readout units (one S-link per crate). Up to 18 ODE boards and one DC are housed in one ODE crate. The DC also contains the TTC-Rx chip and manages the distribution of the system clock and trigger signal to the ODE boards in the crate.

Incoming signals are assigned the appropriate BX identifier and sent to the L0 pipelines. In parallel, the data and the four least significant bits of the associated BX Id are sent to the L0 trigger. Data resides on the L0 pipelines for $4\mu\text{s}$ before receiving the L0 yes/no signal. Triggered data are then moved to the L1 buffer, where they wait for the L1 decision. If this is positive, data are zero-suppressed and multiplexed to the DC on the back-plane bus.

The average data size for $b \rightarrow \mu X$ events has been estimated to about 1.6 kbytes, assuming that full information for each hit would be a 32-bit word. About 75% of the hits originate from station M1.

The LVDS receivers, the L0 pipelines and the

L0 derandomizer are integrated in a single component, the SYNC chip [72], presently under development. A custom chip has been preferred over an FPGA solution for several reasons, fully explained in reference [72]. This solution is more compact and reliable, allowing greater flexibility in the implementation of functions crucial for system operation:

- *System time alignment:* The relevance of measuring the phase of logical channels within the BX period has been discussed in reference [40]. A low-resolution (3 bit) TDC is adequate for this purpose. The time information associated to the hits is sent to the L0 pipeline and enters the normal data path to the DAQ.
- *System remote control:* It is of fundamental importance to equip the system with a number of error-detection features, allowing remote control and diagnosis of possible malfunctioning in the boards.

The other main board components (L1 buffer, trigger interface and bus interface) are based on FPGAs. Each ODE board also contains a CAN node.

A total of 168 ODE boards and 12 DC boards (one per crate) is foreseen.

5.3.7 System synchronisation

A system synchronisation procedure under consideration involves two phases, briefly described in the following:

1. When the whole system is powered-up, a calibration run is performed. This consists of a complete scan of all physical channels. In order to adjust a single channel, other physical channels normally logically ORed with it are masked within the DIA-LOG chips. The signals' BX identifier and the phase inside the BX cycle are measured at the level of the L0 pipelines. Time spectra for each channel are acquired inside the SYNC chips.

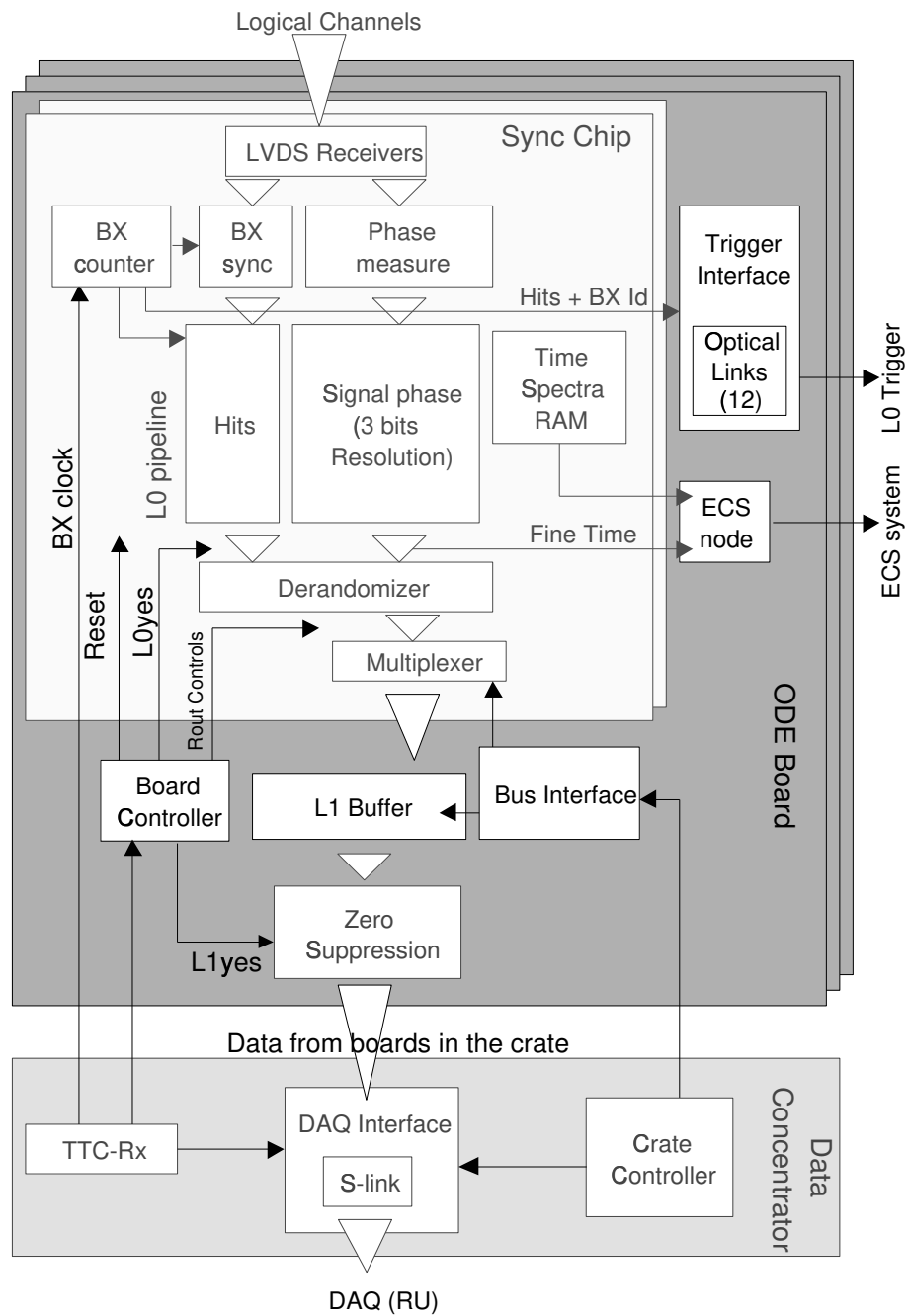


Figure 62 Schematic of the ODE boards and the crate interface

2. The detection of the relative phase between the rising edge of the system clock and that of the time spectra allows the calculation of the delay to be added to each channel for correct time alignment. This delay consists of two numbers. The first is the phase relative to the clock rising edge (fine-time offset), the second is the difference in BX cycles (bunch-crossing offset). The delay correction is realized by setting the fine-time correction on the FEB (inside DIALOG) and the BX correction inside the ODE boards (SYNC chip).

Compared to other schemes not using signal-phase information of channels, the procedure described above is rather fast, although sufficient statistics also for the lower-rate outer regions are necessary. Moreover, it must be executed only once, when the system is set-up before data taking. The fine-time and bunch-crossing offsets constitute calibration constants, to be saved in a database. The detector alignment is monitored online using the SYNC chip.

5.3.8 Radiation levels

The radiation level estimate considered for the system design is given in Ref. [73]. This gives an accumulated dose in 10 LHC years of about 1 MRad in the inner part of station M1. The dose decreases radially and is reduced to about 1 kRad at the sides of the detector. This means that radiation-hard electronics must be used for the FEBs, while commercial devices can be placed in the IBs and ODE boards. Both the CARIOCA and the DIALOG chip are designed in radiation hard-technologies (0.25 μ m CMOS). It is also important to consider particle rates, which affect the single event upset (SEU) behaviour of the system. In this respect the use of FPGAs, containing important amounts of SRAM, must be considered carefully. Whenever possible, complex logical functions will be implemented using anti-fuse based FPGA technologies (e.g. Actel family). The number of SRAM-based FPGAs (e.g. Xilinx and Altera families) is to be minimised, even in the ODE boards. Whenever used, a specific procedure is envisaged to compare the FPGA configuration with a local copy.

This function is performed by the CAN-node micro controller, which also takes care of uploading the FPGA configuration when mismatches are detected [74]. SEU immunity of the DIALOG chip, also placed in the higher-rate regions, is ensured through the use of triple voting for all internal registers and the implemented logical functionality. Moreover, the content of the registers is refreshed regularly via the I²C interface.

5.3.9 Cooling of the FE-electronics

The inner regions of the Muon System are characterised by a large amount of electronics located in a small space, in particular in region R1 of stations M2 and M3 where each chamber contains 224 readout channels. An estimate of the dissipated power has been performed in these cases, assuming a Faraday cage containing the chamber and the electronics with thermal contact only along the outer perimeter, while the front and rear faces are considered insulating. A nominal consumption of 15 mW/channel has been assumed for CARIOCA. To this number, the consumption of the DIALOG chip and the presence of some service elements (local regulators, controls, etc.) must be added. The amount to be added has not yet been quantified, and is therefore not considered in this evaluation. Using the approximate formula $dT = 900 \times (P/S)^{0.8}$, where dT is the internal thermal gradient ($^{\circ}$ C), P is the total dissipated power in the box (W) and S is the surface available for heat exchange (cm^2), the inner chambers are found to be subject to an increase in temperature of 10° C. Although this does not represent a significant problem, several possibilities are under investigation, for example pumping air through the box with a simple pipe network. A better understanding of the situation will come when a more realistic estimate of the power consumption becomes available. In addition, a test with a real box is planned in the near future.

5.4 Service systems

5.4.1 Gas system

The design of the gas system under consideration for the muon system is described in detail in

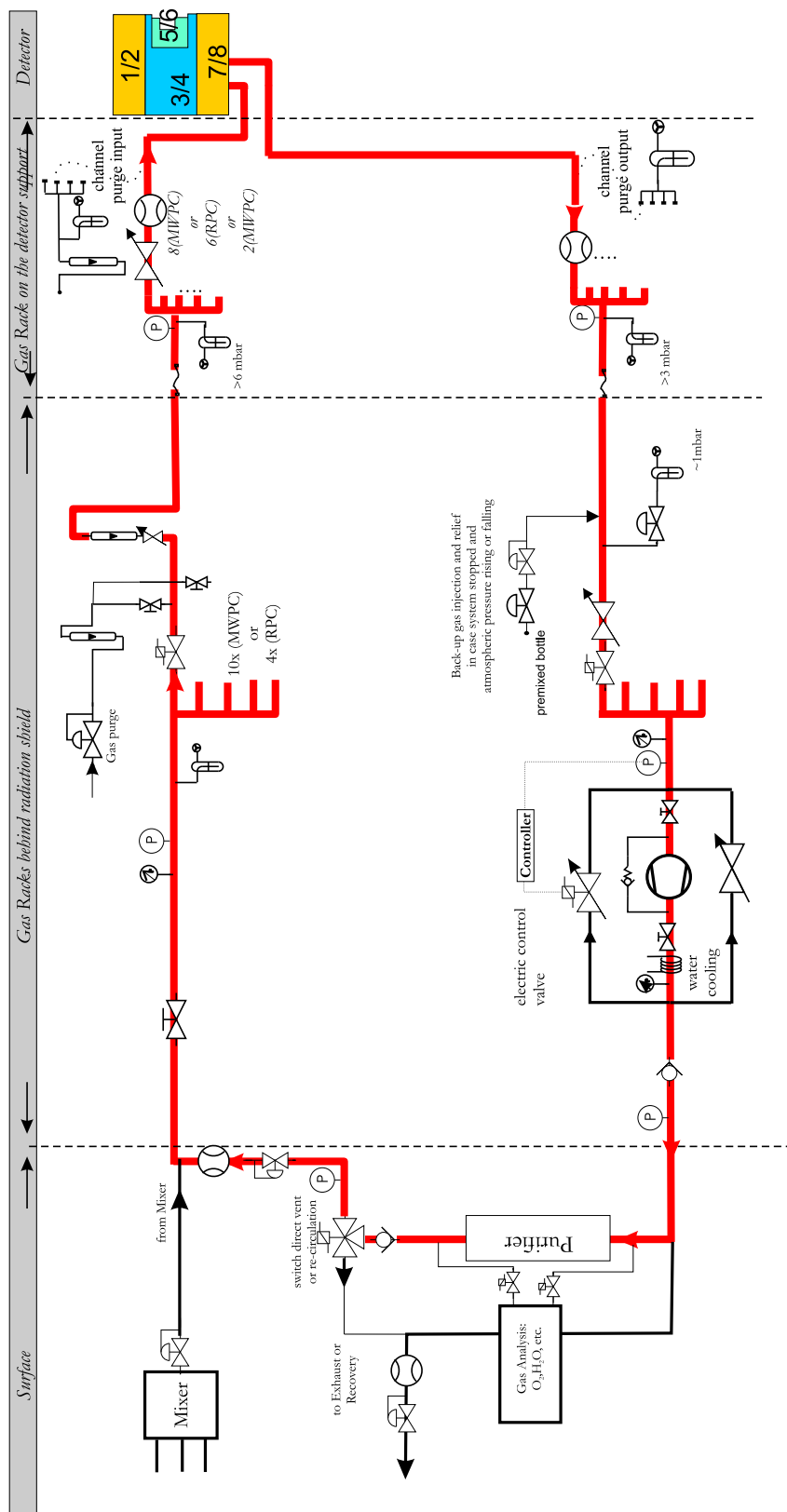


Figure 63 Schematic pipe and component drawing of the muon gas system.

Ref. [75]. As a consequence of the two detector technologies employed, two independent gas systems have to be designed and constructed. The gas volume of the MWPC amounts to 4.5 m^3 . Test results have shown that this detector is suitably operated with a gas mixture of $\text{Ar}/\text{CO}_2/\text{CF}_4$ (40:50:10). For the RPC detector with a total volume of 0.83 m^3 a mixture of $\text{C}_2\text{H}_2\text{F}_4/\text{C}_4\text{H}_{10}/\text{SF}_6$ (95:4:1) non-flammable composition is foreseen. A compilation of the basic parameters of both detectors concerning the gas system is listed in Table 20.

Gas components will be mixed with the appropriate composition in the mixer in the surface gas building at the experiment. In addition the RPC gas mixture will be monitored continuously with an infrared analyser. If the C_4H_{10} ratio exceeds the flammability limit the gas supply will be stopped immediately. Both gas systems will run in a closed loop (Fig. 63). The expected circulation flow rate will be between 6 to 12 hours per volume exchange. A pump in the return line allows the gas to be compressed before entering the gas building at the surface. To stabilise the pressure in the muon detector, a back-pressure regulator in parallel with the pump controls the pressure to 0.5 mbar below atmospheric pressure at the inlet of the pump. Using an inline purifier situated in the gas building at the surface, the regeneration rate will be kept above 90%. The purifier consists of two cleaning agents: a molecular sieve (3\AA) to remove water vapour and activated copper as reducing agent for oxygen removal. A humidity and an oxygen meter will measure the impurity concentration before and after the purifier. Each half station of the muon system is connected to one supply line and only in stations 4 and 5, where both gas mixtures are needed, two input lines will be used. Distribution racks, mounted on the detector support, will distribute the gas to the muon chambers. One half station is divided in ten gas regions, controlled by gas flow meters at the input and output of each separated gas volume. A safety relief bubbler is incorporated into every gas channel to prevent over pressure of the chamber modules. The existing DELPHI supply and return pipes between the SGX building and the UX cavern will be reused by the LHCb experiment and hence for the two muon

gas systems. The gas control will follow the general recommendations of the Joint-Control-Project of the four LHC experiments (JCOP) [76].

5.4.2 High-Voltage system

The HV distribution system of the chambers is based on the assumption that for the safe and reliable operation of the detectors there should be independent operation of the gaps inside a chamber. However, for the MWPCs (and possibly also for the RPCs) this leads to a very large number of HV channels (3456 for the MWPC) that could be prohibitively expensive. Alternative solutions have also been studied.

5.4.2.1 MWPC detector

For the MWPC, assuming that the various chambers exhibit similar gain responses (i.e. the "knee" of the efficiency plateau is within $\pm 50\text{ V}$) and therefore will be operated well inside the region of full efficiency, a scheme is foreseen where several gaps are serially chained. For the determination of the optimal configuration, the following considerations should be taken into account:

- Chains should comprise homologous gaps (i.e. gap 1 of chamber 1 chained with gap 1 of chamber 2, etc...), to minimise, in case of HV problems, the effect on geometrical efficiency of the trigger;
- Due to high local rate, chains should equalise the amount of current drawn by MWPC, also the characteristics of HV systems commercially available should be considered.

In this scheme the number of channels needed would be 1200. Assuming a current of $3\mu\text{A}$ per MHz of incoming radiation (at a gain of 10^5), each HV channel would draw less than 0.5 mA at the operating voltage.

The MWPC HV system will have a main control unit, fully remotely programmable, in the control room and detached subunits, built in radiation tolerant technology, located in the off-detector electronics racks, which will provide HV to the

Table 20 Basic gas parameters of MWPC and RPC

Detector	MWPC	RPC
Gas	Ar/CO ₂ /CF ₄	C ₂ H ₂ F ₄ /C ₄ H ₁₀ /SF ₆
Volume (m ³)	4.5	0.83
Flow Rate (m ³ /h)	0.375–0.75	0.07–0.14
Regeneration rate (%)	>90	>90
Impurities: O ₂ (ppm)	50	10
Impurities: H ₂ O (ppm)	50	10
Pressure (mbar above atm.)	1	1
Pressure max. (mbar)	5	3

chambers. Each channel should deliver up to 4 kV and 1 mA. Models with these characteristics are commercially available.

A careful scheme of HV-grounding, compatible with the grounding of the detector and FE electronics is under study.

5.4.2.2 RPC detector

The RPC system requires 960 HV channels each able to deliver up to 12 kV and 1 mA. The solution envisaged at present follows the developments made in this field by the ATLAS and CMS collaborations. In such a scheme the RPC power supply system is made of two main blocks: a main board (Generator Board, GB), located in the counting room, supplying the power at a medium voltage and managing the remote controls and monitoring, and a remote system (Distributor Box, DB), located in the electronics racks, consisting of a radiation tolerant board hosting a transformation stage generating both the high and the low voltages needed by the system. In this way the problem of distributing the high voltage over long distances is minimised, while keeping the main power supply controllers, which are radiation sensitive, in a safe environment.

The GBs supply a medium voltage which is easy to distribute over long distances with conventional cables (the foreseen voltage is 48 V), and supports a communication link for remote control and monitoring purposes. The GBs would be interfaced with the general LHCb control system and would be placed in the counting room allowing an easy and safe access to the power supply system.

In the DBs the input medium voltage is transformed into two HV channels, which are floating, allowing an optimal grounding configuration. Moreover, the HV channels are fully programmable remotely. The voltages and currents can be remotely monitored through the communication link driven by the GBs. The communication line is optically decoupled to preserve the floating ground of the voltage channels.

Finally, the feasibility of a solution with a reduced number of HV channels to be applied in the case the cost becomes prohibitive is under study. In this configuration two gaps in a single chamber would still be powered by different HV lines while the two gv tdr.ps corresponding gaps belonging to two adjacent chambers in the bending plane share the same HV. This configuration would allow to keep a high detection efficiency even in case of failure of a high voltage channel, while reducing by a factor of two the number of DBs needed by the system.

5.5 Chamber support structures and muon filter

Two independent support structures are envisaged for the muon system:

- A support structure for the chambers and electronic racks, suspended from a general structure (gantry) on the top, which is used as well by other sub-detectors including the scintillating pad detector, and the preshower [26].
- A support structure for the muon filter on

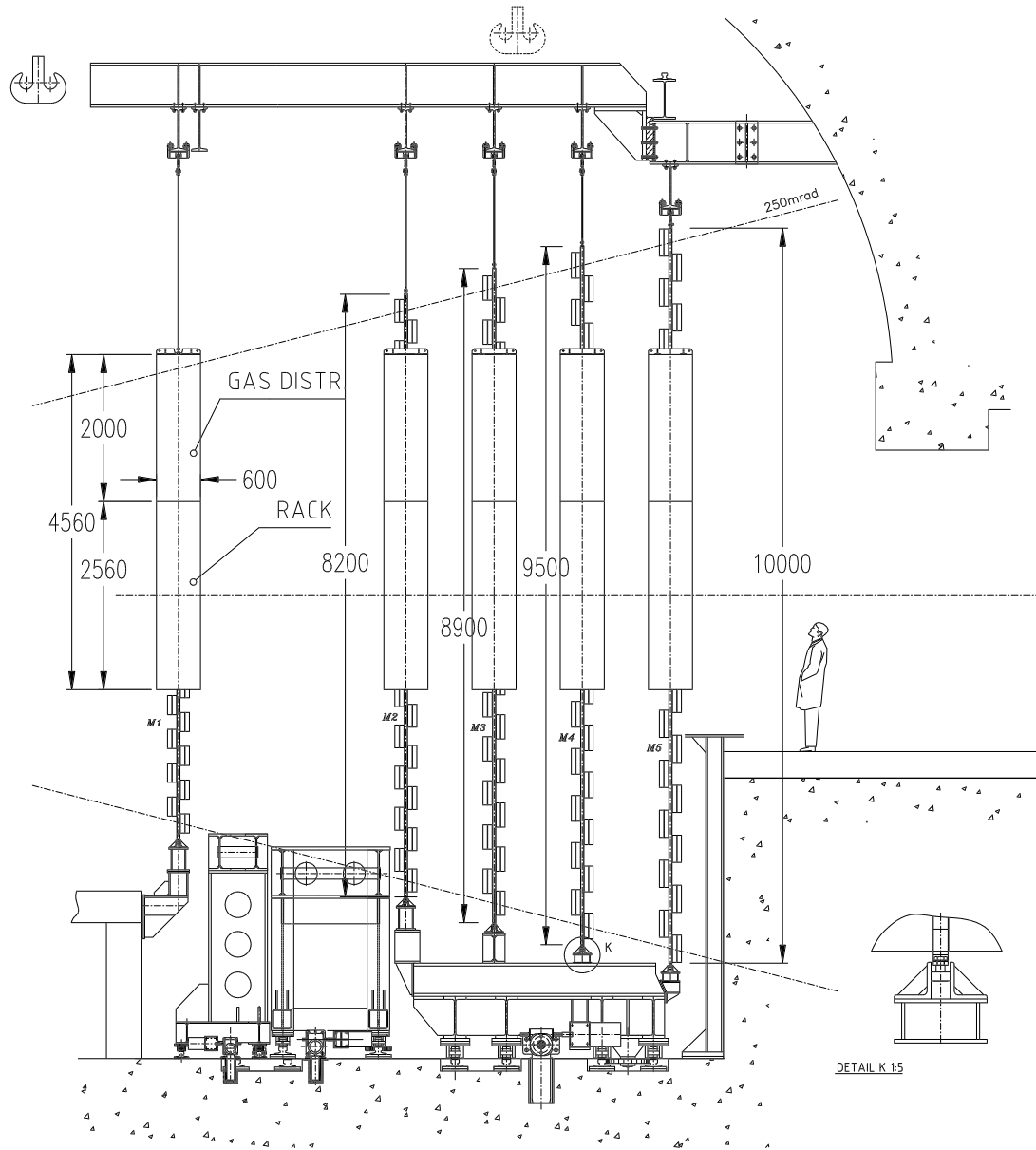


Figure 64 Side view of the Muon system support structures

movable platforms.

The two support structures will be briefly discussed in this section. Details can be found in Ref. [77].

A common requirement for all LHCb sub-detectors is that provision has to be made for access to the LHC beam pipe, for maintenance procedures, in particular for bake-out. For this reason the muon system will be constructed in two halves, so that one side can be withdrawn, allowing access to the beam pipe. The complete retraction of each half station is also important for installation and maintenance of the chambers and their FE-electronics.

5.5.1 Chamber support structures

Each muon station consists of 276 muon chambers. They are arranged in four layers to provide full angular coverage. Two layers are in front and two behind a wall-like support structure hanging from the top. The muon stations must fit into the 40 cm space available between the absorber walls, except for station M1, for which the allocated space is only 37 cm.

5.5.1.1 Requirements and constraints

The muon stations will be constructed in two halves. The possibility to completely retract each half station should be ensured for installation and maintenance of the chambers and their FE-electronics, and to provide access to the beam pipe.

The chambers have to be positioned within each muon station with a precision of about 1 mm in the x and y directions and 5 mm in the z coordinate along the beam axis. Gas pipes and cables to the chambers for readout and HV/LV have to be supported within the allowed thickness for each station. Gas pipes will be routed vertically from the top to the distribution system, while signal and HV/LV-cables will be routed horizontally to the sides, where the readout electronic racks will be placed.

Table 21 summarises the overall dimensions and weights of the five muon stations and the supporting structures for the five muon stations.

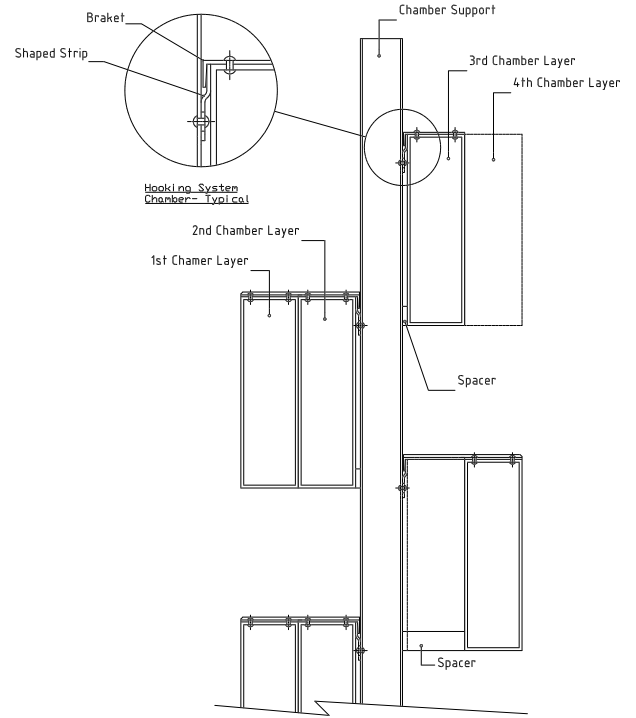


Figure 65 Fixation of chambers to the support structure

5.5.1.2 Wall structure

The support walls are suspended by means of rectangular linking pieces from an iron beam. On the bottom, the walls are guided to prevent accidental contacts with iron absorbers during opening/closing operations and to improve the stability of the station position. Two racks for the electronics are placed at half height on both sides of each muon station. The racks are supported by an independent linking piece and rigidly fixed to the external side of the chamber supporting structure to prevent any relative displacement. A schematic layout is shown in Figure 64.

Each chamber support wall consists of two 1-2 mm thick aluminium sheets, interleaved by a layer of 0.7 mm thick corrugated aluminium. The benefits of this design are a high degree of modularity and full flexibility in chamber positioning. The total thickness of the wall is 42 mm for M1 and 44 mm for M2–M5. Rivets are used to connect the three sheets together. Each half wall is composed of several panels which are connected together by rectangular aluminium tubes. Special

Table 21 Muon station support structure dimensions and weight. The indicated chamber weight is based on honeycomb panels for the MWPCs.

	Station M1	Station M2	Station M3	Station M4	Station M5
Active area (m ²)	49.0 7.7 × 6.4	76.6 9.6 × 8.0	89.2 10.4 × 8.6	102.7 11.1 × 9.3	117.2 11.9 × 9.9
Wall structure area (m ²)	52.1 7.9 × 6.6	80.4 9.8 × 8.2	94.3 10.6 × 8.9	108.3 11.4 × 9.5	121.0 12.1 × 10.0
Total weight of chambers (kg)	3700	5400	6100	4900	5500
Wall structure weight (kg)	471	1223	1369	1564	1742

care has to be taken in designing the junction of the two halves, avoiding any mechanical interference due to the overlapping of chambers.

5.5.1.3 Chamber positioning

The Chambers are attached to horizontal rails on the walls, which allow to move and position the chambers horizontally. The correct vertical positioning is fixed by the position rails. Reference pins will be added to fix the correct horizontal position of the chambers and to be able to reproduce it. The system is sketched in Figure 65.

5.5.1.4 Maintenance

Access to the chambers close to the beam pipe is only possible if a muon station is completely retracted between the iron absorbers by about 4 m for station M1 and about 6 m for station M5. Including about 3 m space for electronics racks and access to them, the required space from the beam line extends to $\simeq 11$ m in station M1 and to $\simeq 15$ m for station M5 (see Figure 66)⁴.

5.5.2 Muon filter

The muon filter is comprised of the electromagnetic and hadronic calorimeters and three iron shields, interleaved between the muon stations. An additional shield immediately behind station M5

⁴The present layout of the LHC cryogenics accommodated at the end of the LHCb experimental area does not leave sufficient space for the maintenance of the muon system. Other options for the positioning of the LHC cryogenics are therefore under investigation in a collaborative effort with the accelerator groups concerned.

Table 22 Muon filter composition

Detector Element	Depth	
Calorimetry	267 cm	$6.8 \lambda_I$
Muon filters 1–3	80 cm	$4.4 \lambda_I$
Total thickness		$20 \lambda_I$

protects this station from machine related background and back splash from nearby LHC beam elements.

The total weight of the muon shield is about 2100 tons. The composition of the muon filter is summarised in table 22.

The material for the muon filter will come from the iron blocks of the West Area Neutrino Facility (WANF). The blocks will become available early in 2002 and have a density of about 7.2 kg/cm^3 and a size of 80 cm and 160 cm in length, 40 cm and 80 cm in width and 20 cm, 40 cm and 80 cm in height. These dimensions match the required absorber thickness of 80 cm. A detailed layout of the absorber walls with the existing blocks has been done [77]. The area around the beampipe will be equipped with special blocks, which give also support to the plugs between the walls.

The movable platforms for the muon filter make use the existing rails in the experimental area, formerly used for the endcap of the DELPHI detector. It is not foreseen that the filters have to be moved independently. Opening of the iron absorbers implies opening the muon stations of that side, since the electronics racks, which are 60 cm wide and permanently connected to the stations, do not allow the opening of the iron walls alone.

In order to ensure static stability in case of seis-

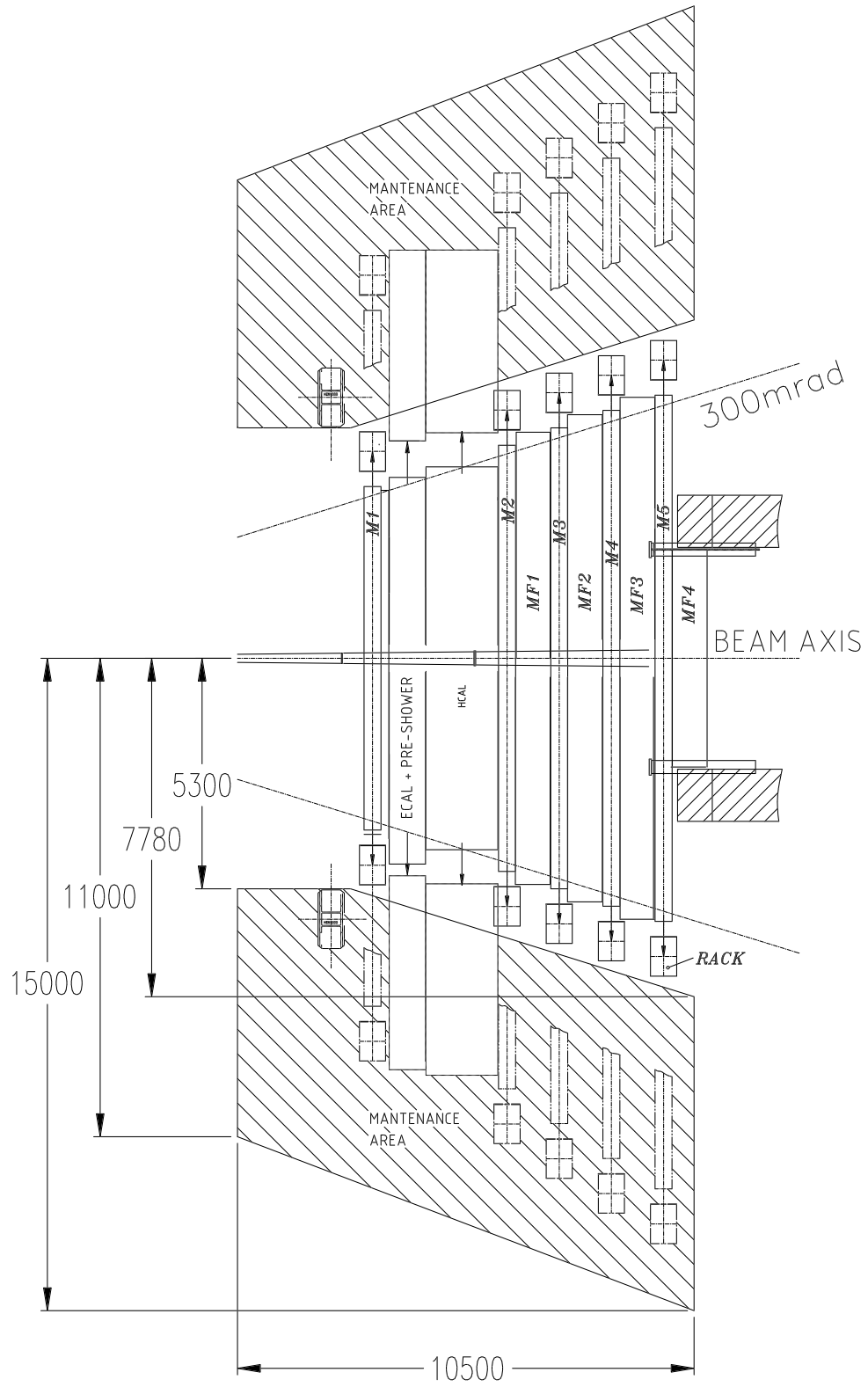


Figure 66 Top view of the Muon system with the stations moved out for maintenance.

mic activity, the iron blocks forming one muon filter are connected by welded joints. Following this procedure, mono blocks of absorbers will be created. In addition, the iron absorbers on the same side of the beam pipe will be connected to one another to enhance further the static stability. The mechanical connections have to be removed every time a station will be retracted for access to the chambers. No moving of the iron wall is foreseen for maintenance of the muon detector.

5.5.3 Beam pipe shielding

Special plugs are foreseen close to the beampipe to protect the chambers from particles which emerge from the beampipe. An optimization of this shielding has been performed [78], taking into account the 1.5 cm required space for bakeout instrumentation of the beampipe. The plugs extend from 12 mrad out to 18 mrad in x projections, and from 12 mrad to 15 mrad in y projection.

5.6 Safety aspects

The Muon detectors of LHCb will follow the CERN safety rules and codes, CERN safety document SAPOCO 42 and European and/or international construction codes for structural engineering as described in EUROCODE 3.

In the following the specific risks, and actions, are summarised, as discussed in the Initial Safety Discussion (ISD) with the CERN Technical Inspection and Safety (TIS) Commission.

1. The chambers differ in dimensions according to their position in the muon system. Depending on their size, the weight of MWPCs differs between $\simeq 5$ kg in region R1 and $\simeq 30$ kg in region R4. The weight of a RPC is $\simeq 20$ kg. The chambers can be handled by 1–2 persons during the installation, following the safety instructions⁵.
2. The final choice of the chamber materials will be done according to the safety instructions⁶, and the use combustible materials

will be minimised. Alternative materials replacing the polystyrene in the RPCs are under investigation.

3. The gas mixtures used in the muon chambers, Ar/CO₂/CF₄ (40:50:10) for the MWPC detector and C₂H₂F₄/C₄H₁₀/SF₆ (95:4:1) for the RPC detector are not flammable. As the detectors will be operated with a maximum overpressure towards the atmosphere of 300 Pa set by high throughput bubblers, the chambers are not classified as pressure vessels⁷.
4. The RPC detectors will be run at 10 kV⁸. The total current for each supply line will be ≤ 1 mA. The low voltage supply to the detector read-out is below 15 V⁹.
5. The high pressure part of the gas systems is located in the surface buildings. The systems will be built according to the appropriate rules¹⁰.
6. The effects of seismic activity will be studied in collaboration with TIS.

⁵Safety code A5

⁶Safety Instructions 41

⁷Safety code D2 Rev.2

⁸H.V.A. as defined in Safety Instructions 33

⁹Safe Extra Low Voltage (S.E.L.V.) as defined in Safety Instructions 33

¹⁰Safety Instruction 42 and Safety Code D2 Rev.2

6 Project Organisation

6.1 Schedule and Milestones

The overall work programme and schedule is summarised in Figure 67. It is split into three parts, the chambers, the electronics and the infrastructure. The schedule covers the period up to the end of 2005 and ensures that the Muon system is fully commissioned and operating together with the other LHCb sub-detectors by this time.

6.1.1 Chambers

6.1.1.1 MWPC detector

The engineering design of the MWPC detector should be finalised and frozen by the end of 2001, based on the experience acquired with the prototype chambers. Moreover, by the end of 2001 the MWPC ageing test should have provided significant results, providing additional information about the long term behaviour of the chamber components under irradiation. In the year 2002 the “module 0” of each of the chambers in the various regions will be constructed and tested with the final tools developed during the year 2001. In parallel, the production lines will be set up. In case panels based on honeycomb will be used, the panel preparation is rather time consuming and should therefore start about 1/2 year in advance of the chamber production. It is foreseen to have four centres for chamber construction, assembling and testing. The time estimated for chamber construction is two years. Therefore, production should have started by January 2003 at the latest. Depending on the complexity of a chamber type, a fully tested chamber should be produced within 1–5 working days. Chamber installation and commissioning of the muon system should start mid 2004 and take about one year. The major milestones for the MWPC detectors are summarised in Table 23.

6.1.1.2 RPC detector

Developments on prototype chambers should be finished by the end of 2001, when the engineering design should be finalised and frozen. The tests planned in 2001 will allow a final decision

on the oil treatment of RPCs in LHCb. In addition, significant results from the RPC ageing test should be available by that time. A “module 0” for each chamber type will then be prepared and tested with a time scale of nine months. In parallel, the production lines will be prepared, consisting of the assembly tools and test setups in the institute laboratories. A period of three months for the production and selection of the bakelite plates, and a period of nine months for the gap production has been estimated. Both productions will be done in industry, receiving prompt feedback from the quality checks performed in the institutes. Chamber assembly should take about 100 working days at the rate of 5 chambers/day. Measurements with cosmic rays will be performed in parallel in two centres and should be completed with a time scale of one year. The chambers will be transported to CERN in the first half of 2004, followed by a period of about one year for installation and commissioning. The major milestones for the RPC detector are summarised in Table 23.

6.1.1.3 Chambers for the inner part of M1

The detector technology for the inner part of station M1 should not be chosen later than January 2003. This leaves two years for finalising the detector design and the construction of the chambers. Installation and commissioning should take place in the first half of 2005.

6.1.2 Electronics

The main tasks for the Muon System FE-electronics and the major milestones are also summarised in Figure 67 and Table 23. A few important aspects are pointed out in the following.

6.1.2.1 Front-end chip

A critical task is the design of the CARIOCA FE-chip. Besides the preamplifier, which shows very satisfying results, the design includes also a fast shaper, a baseline restorer (BLR) and a discriminator. In particular the latter two require more work during the year 2001. In order to obtain final products to be mounted on the FE-boards early in 2003, the design and tests of CARIOCA should

Table 23 Muon Project Milestones

Date	Milestone
January 2002 January 2003 December 2004	MWPC detectors Engineering design completed Begin chamber construction and tests Chamber construction completed
December 2001 January 2002 May 2003 December 2004	RPC detectors Decision on use of linseed oil RPC engineering design completed Begin RPC assembly and tests Chamber construction completed
January 2003 December 2004	Chambers for the inner part of M1 Technology choice Chamber construction completed
March 2002 March 2002 June 2002 October 2002 January 2003 October 2003 December 2004	Electronics CARIOCA design and test completed DIALOG design and test completed SYNC design and test completed Full chain electronics test completed Begin FE-board production Begin IM- SB and ODE-board production Electronics assembly and test completed
December 2003 June 2004 July 2005	Muon filter and support structures Iron filter installation completed Chamber support structures installed Muon System commissioning completed

be completed by March 2002, when the FE-chip status will be reviewed. Assuming that the tests of the full CARIOCA prototype are satisfying, about nine months are left for the engineering run and the production of the chips. In case the tests of CARIOCA reveal severe problems, enough time would be left to switch to the backup solution, the adapted ASDQ chip. The viability of the backup solution will be maintained until the final decision on the FE-chip has been taken. The necessary studies for the ASDQ chip will be carried out during the year 2001.

6.1.2.2 Readout electronics

The basic design of the various components of the readout electronics chain should be completed between mid 2001 and mid 2002, as indicated in Figure 67. This includes in particular the design of the DIALOG and SYNC chips. In order to avoid a delay to the test of the full readout chain, scheduled for autumn 2002, a backup solution integrating the essential functionalities of the SYNC chip inside

an FPGA is envisaged. In parallel to the test of the full electronics chain, radiation tests for the DIALOG and SYNC chips will be carried out to prove their SEU immunity. The tests are followed by a period of two years, during which the engineering design of the various boards will be finalised, and the tendering, production, assembling and testing takes place.

6.1.2.3 Monitoring and control

The preferred solution for the ECS interface of the muon system is based on the CAN-ELMB standard. In order to prove the SEU immunity of this interface and the backup solution (SPECS [79]¹¹) extensive tests are in progress to allow a final choice of the ECS interface for the muon system in autumn 2001. This will be followed by a prototyping and test phase before production of the service boards starts beginning of 2003.

¹¹Serial Protocol for ECS, based upon the ATLAS Calorimeter serial protocol SPAC

6.1.3 Infrastructure

6.1.3.1 Muon Filter

The iron blocks for the muon filter will become available early in 2002. As the muon filters occupy a rather large amount of space, their construction in the experimental area will be delayed until the installation of the LHCC cryolines has been completed in September 2003. The installation of the shields should take about three months.

6.1.3.2 Chamber support structure

The muon system support structures are attached to gantries, which limit the clearance of the crane in the experimental area. In order to maximise the time during which full use of the crane is possible, the installation of the gantries should only be carried out at the beginning of 2004, when the construction of the muon filters and the installation of other heavy equipment is completed. The installation of the support structures will take about three months. The muon detector installation could start in parallel with the LHCC octant test, scheduled from April to September 2004. Since beam tests will be done mainly in the nights, only minimal interference is foreseen, except for the hindrance caused by the beam pipe.

6.1.4 Installation and commissioning

Both MWPC and RPC detectors will undergo installation and commissioning during the second half of 2004 and first half of 2005. Commissioning with other LHCb sub-detectors, using common DAQ will begin in the summer of 2005. Six months of operation in this mode are foreseen to ensure the muon detectors will be ready to take data at nominal LHCb luminosity early in 2006.

6.2 Costs

The total cost for the Muon system is estimated to be 10,830 kCHF. Table 24 shows the cost estimate split according to the system components. For the chambers and electronic boards about 10% of spares have been included. Wherever possible, the cost estimation of components is based on

quotes from industry or recent purchases of similar items.

The iron for the muon filter is a special in-kind contribution from CERN, for which the cost has been estimated to 4,000 kCHF. The remaining cost of 6,830 kCHF for the muon detector system has been estimated under the assumption that the CARIOCA FE-chip can be used for the MWPC detector. The total cost would be higher by about 600 kCHF in case the adapted ASDQ chip would be required.

6.3 Division of responsibilities

Institutes currently working on the LHCb Muon project are: Centro Brasileiro de Pesquisas Físicas CBPF, and Universidade Federal do Rio de Janeiro UFRJ, Rio de Janeiro (Brazil), Universities and INFN of Cagliari, Ferrara, Firenze, Roma “La Sapienza”, Potenza, Roma “Tor Vergata”, Laboratori Nazionali di Frascati LNF (Italy), Petersburg Nuclear Physics Institute PNPI, Gatchina (Russia) and CERN. Work on the Level 0 Muon trigger is carried out by CPPM Marseille in close collaboration with the Muon group.

The sharing of responsibilities for the main Muon Project tasks is listed in Table 25. It is not exhaustive, nor exclusive. Details of the responsibilities for the various system components will be finalised by the time of the engineering design reports, and when precise information of all funding agencies is available.

Software is a major task in the project and not listed in Table 25. It is understood that the Muon group as such is responsible and will have the resources of 6 FTE to provide all muon system specific software. This includes algorithms for simulation, reconstruction and monitoring software for DAQ and controls.

The studies required to maintain the viability of the backup solution for the FE-chip are carried out by the CERN and Rome I groups in close collaboration with the University of Pennsylvania, where the ASDQ chip has been designed.

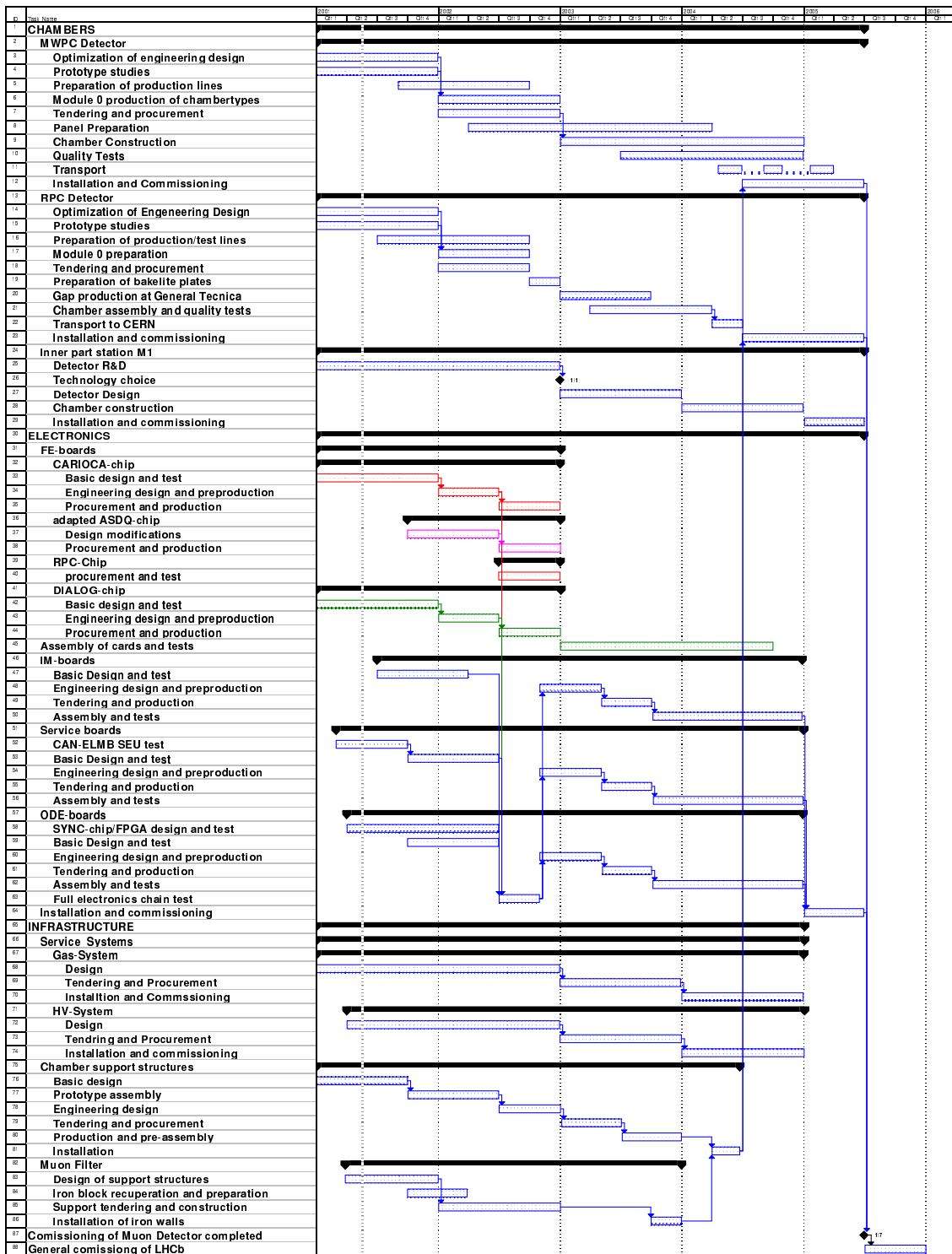


Figure 67 Schedule of Muon project, up to start of LHCb data taking early 2006

Table 24 Muon project cost in 2000 prices (kCHF).

Item	Unit	Number of units	sub-total (kCHF)
MWPC detector:			1220
Panels	m ²	1400	
Special cathodes	m ²	220	
Wire Fixation bars	0.5 m	15000	
Frames	0.3 m	6000	
Spacers	piece	25000	
Wire	km	1215	
HV-boards	board	13000	
Tooling	prod.lines	4	
Assembly	chamber	900	
RPC detector:			260
Bakelite	m ²	1300	
Gas gap production	chamber	500	
Strips	m ²	500	
Foam panels	m ²	500	
HV-Connectors	piece	1000	
Mechanics	chamber	500	
Assembly	chamber	500	
Electronics:			4040
CARIOCA-chip	piece	12500	
DIALOG-chip	piece	8000	
RPC FE-chip	piece	3500	
FE-boards	board	8000	
Spark-Protection-boards	board	8000	
LVDS links	link	1800	
IM-boards	board	180	
Off-Detector-Elec.-boards	board	180	
Service-boards (ECS)	board	160	
Data-Concentrator boards	board	12	
Optical links to L0 trigger	link	1250	
Crates	crate	36	
LV-power supplies/cables	system		
Services:			1310
MWPC Gas System	system	1	
RPC Gas System	system	1	
MWPC HV System	system	1	
RPC HV System	system	1	
Support Structures	module	10	
Muon filter:			4000
Muon System TOTAL			10830

Table 25 Muon project: Sharing of responsibilities.

Task	Institutes
MWPC detectors: Stations M1 – M3, outer part (Construction and Testing) Stations M2 – M5, inner part (Construction and testing)	Ferrara, LNF, PNPI, Rome I / Potenza CBPF, CERN, Ferrara, LNF, UFRJ
RPC detectors: Stations M4 – M5, outer part (Construction and testing)	Firenze, Rome II
Inner part of station M1: (Construction and testing)	Cagliari, LNF
Readout electronics: CARIOCA chip design, production and testing DIALOG chip design, production and testing SYNC chip/FPGA design, production and testing MWPC FE-boards (production and testing) RPC FE-boards (production and testing) IM-boards, design, production and testing Service boards, design, production and testing ODE-boards, design, production and testing	CERN, UFRJ Cagliari Cagliari CBPF, PNPI, Rome I / Potenza, UFRJ Firenze, Rome II LNF Rome I Cagliari, LNF
Services: Gas systems (Design) Monitoring, Control (ECS)	CERN Rome I
Experimental area infrastructure: Chamber support structures Muon filter support structures Muon filter installation	CERN, LNF CERN CERN

References

- [1] LHCb Technical Proposal, CERN/LHCC 98-4.
- [2] P. Colrain *et al.*, “Optimisation of the Muon system Logical Layout”, LHCb 2000–016 Muon.
- [3] M. Adinolfi *et al.*, “Proposal for the RPC Muon Detector of LHCb”, LHCb 2000–53 Muon.
- [4] G. Auriemma *et al.*, “Thin Gap Chambers for the LHCb Muon detector”, LHCb 2000–113 Muon.
- [5] B. Bochín *et al.*, “Wire Pad Chambers and Cathode Pad Chambers for the LHCb Muon System”, LHCb 2000–114 Muon.
- [6] B. Bochín *et al.*, “Wire Pad Chambers for the LHCb Muon System”, LHCb 2000–003 Muon.
- [7] P. Colrain *et al.*, “Performance of a multigap RPC prototype for the LHCb Muon System”, NIM A 456 (2000) 62-66
- [8] N. Saguidova *et al.* “GCALOR Studies of Background in the LHCb Muon chambers”, LHCb 1998-059 Expt; A. Tsaregorodtsev, “Muon System parameterised background – algorithm and implementation”, LHCb 2000–011 Muon.
- [9] P. Colrain, “Upgrade of the Muon System background parameterisation”, LHCb 2001–029 Muon.
- [10] ATLAS muon collaboration, “ATLAS muon spectrometer, Technical Design Report”, CERN/LHCC 97–22
- [11] CMS muon collaboration, “CMS The muon project, Technical Design Report”, CERN/LHCC 97–32
- [12] P. Bartalini *et al.*, “Tuning of multiple interactions generated by PYTHIA”, LHCb 1999–028; LHC SM working group, “B decays at the LHC”, CERN-TH/2000–101
- [13] C. Zeitnitz and T.A. Gabriel, The Geant-Calor interface User’s Guide (1999), <http://www.physik.uni-mainz.de/zeitnitz/gcalor/gcalor.html>
- [14] I. Azhgirey, I. Kurochkin and V. Talanov, “Development of MARS Code Package for Radiation Problems Solution of Electro-Nuclear Installation Design”, in: Proc. of XV Conference on Charged Particles Accelerators, Protvino, October 22–24 (1996)
- [15] R. Le Gac, A. Tsaregorodtsev and V. Talanov, “Particle fluxes in the LHCb Muon System. Comparisons of GCALOR and MARS calculations”, LHCb 1999–036 Muon.
- [16] W. Riegler, “Crosstalk, cathode structure and electrical parameters of the MWPCs for the LHCb muon system” LHCb 2000–061 Muon.
- [17] R. Santonico and R. Cardarelli, NIM 187 (1981) 377.
- [18] R. Cardarelli, A. Di Ciaccio and R. Santonico, NIM A 333 (1993) 399; C. Bacci *et al.*, NIM A352 (1995) 552; R. Cardarelli, V. Makeev, R. Santonico, NIM A 382 (1996) 470.
- [19] M. Adinolfi *et al.*, “Performance of low-resistivity single and dual-gap RPCs for LHCb” NIM A 456 (2000) 95
- [20] W. Riegler, “RPC Simulations”, LHCb 2000–112 Muon.
- [21] J.H. Lopes, “Simulation of chamber inefficiency and noise in the LHCb muon system and study of its effect on the L0 muon trigger performance”, LHBb 2001–060 Muon.
- [22] B. Bochín, *et al.*, “Beam tests of the MCSC prototypes for the LHCb inner tracker”, LHCb 1998–008 IT; O. Fedin, *et al.*, “Study of MCSC with 36 keV monochromatic X-rays”, LHCb 1998–010 IT.
- [23] G. Bencivenni *et al.*, “A triple-GEM detector with pad readout for the inner region of the

- first LHCb muon station”, LHCb 2001–051 Muon.
- [24] J. Christiansen, “Requirements for the L0 front-end electronics”, LHCb 1999–029 Trigger.
- [25] B. Schmidt, “LHCb Muon System by Numbers”, LHCb 2000–089 Muon.
- [26] LHCb Calorimeters Technical Design Report, CERN/LHCC 2000–036 (2000).
- [27] T. Sjöstrand, “High-energy physics event generation with Pythia 5.7 and Jetset 7.4”, Comput. Phys. Commun. 82 (1994) 74.
- [28] H.L. Lai *et al.*, “Improved parton distributions from global analysis of recent deep inelastic scattering and inclusive jet data”, Phys. Rev. D 55 (1997) 1280.
- [29] GEANT Detector Description and Simulation Tool, CERN Program Library Long Writeup W5013 (1994).
- [30] LHCb RICH Technical Design Report, CERN/LHCC 2000–037 (2000).
- [31] LHCb VELO Technical Design Report, CERN/LHCC 2001–011 (2001).
- [32] S. Amato *et al.*, “LHCb muon chamber geometry simulation”, LHCb 2001–033 Muon.
- [33] QQ - the Cleo event generator, <http://www.lns.cornell.edu/public/CLE0/soft/qq>
- [34] G. Barrand *et al.*, “GAUDI: The software architecture and framework for building LHCb data processing applications”, Proc. International Conference on Computing in High Energy and Nuclear Physics, Padua, Italy, 2000, Ed. M. Mazzucato (INFN, Padua, 2000), p. 92.
- [35] G. Corti *et al.*, “LHC-B muon trigger”, Note LHCb 97–001 (1997);
M. Borkovsky *et al.*, “Study of the LHCb muon trigger”, LHCb 1997–007 Muon;
- E. Aslanides *et al.*, “An alternative architecture of the L0(μ) processor”, LHCb 1997–024 Trigger;
E. Aslanides *et al.*, “The L0(μ) processor”, LHCb 1999–008 Trigger.
- [36] E. Aslanides *et al.*, “A synchronous architecture for the L0 muon trigger”, LHCb 2001–010 Trigger.
- [37] E. Aslanides *et al.*, “Performance of the muon trigger algorithm with the muon TDR detector”, LHCb 2001–059 Muon.
- [38] G. Martellotti *et al.*, “Monte-Carlo samples and efficiency definition for the muon system optimisation”, LHCb 2001–007 Muon.
- [39] E. Aslanides *et al.*, “L0(μ) trigger performance with the March 2000 muon system layout”, LHCb 2000–101 Trigger.
- [40] V. Bocci *et al.*, “Time resolution of the muon detector: consequences for trigger performance and detector synchronisation”, LHCb 2001–058 Muon.
- [41] E. Polycarpo and J.R.T. de Mello Neto, “Muon identification in LHCb”, LHCb 2001–009 Muon;
J.R.T. de Mello Neto and E. Polycarpo, “Update on muon identification”, LHCb 2001–061 Muon.
- [42] A.C. Assis Jesus *et al.*, “Multivariate methods for muon identification at LHCb”, LHCb 2001–084 Muon.
- [43] P. Ball *et al.*, “B decays at the LHCb”, Report CERN–TH–2000–101.
- [44] A. Ali, “Flavour Changing Neutral Current processes in B decays”, Nucl. Phys. B (Proc. Suppl.) 59 (1997) 86.
- [45] H. Dijkstra *et al.*, “Study of the sensitivity of the LHCb experiment to the rare decay $B_s^0 \rightarrow \mu^+ \mu^-$ ”, Proc. XXI Brazilian National Meeting on Particle and Field Physics, São Lourenço, Brazil (2000).

- [46] B. Bochin *et al.*, “Beam tests of WPC-7 prototype of the wire pad chambers for the LHCb Muon System”, LHCb 2000–102 Muon.
- [47] A. Kashchuk *et al.*, “Performance study of a MWPC prototype for the LHCb Muon System with the ASDQ chip”, LHCb 2000–062 Muon.
- [48] D. Hutchcroft *et al.*, “Results obtained with the first four gap MWPC prototype chamber”, LHCb 2001–024 Muon.
- [49] B. Bochin *et al.*, “Beam tests of WPC-8 and WPC-9 prototypes of the wire pad chambers for the LHCb Muon System”, LHCb 2001–025 Muon.
- [50] W. Riegler, “Detector physics and performance - simulations of the MWPCs for the LHCb muon system”, LHCb 2000–060 Muon.
- [51] O. Sasaki, “Amplifier-Shaper- Discriminator ICs and ASD Boards”,
<http://online.kek.jp/~sosamu/ASD-PRR.pdf>
- [52] F. Anghinolfi *et al.*, “CARIOCA - a fast binary front-end implemented in 0.25 micron CMOS using a Novel current-mode technique for the LHCb muon detector”, LHCb 2000–093 Muon.
- [53] T. Ferguson *et al.*, “Ageing investigation of CMS EMU prototype chambers”, CMS Note 1999/011
- [54] V. Souvorov *et al.*, “CMS cathode strip chamber ageing test at GIF”, CMS Note (to be published)
- [55] P. Camarri *et al.* NIM A 414 (1998) 317.
- [56] M. Abbrescia *et al.*, NIM A 456 (2000) 143.
- [57] S. Agosteo *et al.*, “A facility for the test of large area muon chambers at high rates”, NIM A 452, (2000) 94.
- [58] G. Aielli *et al.*, “RPC ageing studies”, Proceedings of the 9th Vienna Conference on Instrumentation, Vienna 2001, (to be published in NIM).
- [59] M. Abbrescia *et al.*, “Long term Performance of Double gap Resistive Plate chambers under gamma irradiation”, Proceedings of the 5th International Conference on Position-Sensitive detectors, London, Sept. 1999
- [60] R. Veenhof, “GARFIELD, a drift-chamber simulation program”, W5050 (1999);
<http://consult.cern.ch/writeup/garfield/>
- [61] G. Auriemma *et al.*, “Design and Construction of the Wire Chambers for the LHCb Muon System”, LHCb 2001–026 Muon.
- [62] G. Auriemma, D. Fianza and C. Satriano, “Test results of Chempir Core panels for the MWPC of the LHCb muon system”, LHCb 2001–008 Muon.
- [63] PSPICE analogue circuit simulator, version 8.0x (1998).
- [64] See for details:
<http://www.pi.infn.it/bfactory/IFR/WorkshopJan2001/program.html> and links therein.
- [65] G. Iaselli, Private communication.
- [66] See for details <http://www.pv.infn.it/vitulo/cms/cmsnote1.html> and links therein.
- [67] A. Lai *et al.*, “Muon Front-end Architecture: an update”, LHCb 2001–030 Muon.
- [68] Protocol description:
<http://www.can.bosch.com/docu/can2spec.pdf>
- [69] A. Lai *et al.*, “Muon Front-end Architecture”, LHCb 2000–017 Muon.
- [70] S. Cadeddu, A. Lai, “DIALOG: a chip for the muon detector front-end and logic”, LHCb 2001–062 Muon.

- [71] ELMB technical documentation:
<http://atlasinfo.cern.ch/ATLAS/GROUPS/DAQTRIG/DCS/LMB/SB/index.html>
- [72] S. Cadeddu, L. Impagliazzo, A. Lai, “The SYNC chip in the muon ODE system” LHCb 2001–063 Muon.
- [73] V. Talanov, “Estimation of absorbed dose levels at possible locations for LHCb detector electronics”, LHCb 2000–015 Muon.
- [74] “The LHCb Experimental Controls System”,
<http://lhcb.cern.ch/computing/controls/default.htm>
- [75] F. Hahn, S. Haider and R. Lindner, “LHCb Muon Gas system proposal” LHCb 2001–023 Muon.
- [76] S. Haider, R. Barillère, “Proposal for Gas Control Systems for the LHC experiments gas systems”,
<http://itcowww.cern.ch/jcop/subprojects/GASControl/slides/gcs-proposal.pdf>
- [77] J. André *et al.*, “LHCb Muon Detector Mechanical Support Structure”, LHCb 2001–032 Muon.
- [78] W. Bonivento, “Beampipe and shielding optimisation for the LHCb muon system”, LHCb 2001–028 Muon.
- [79] R. Bernier *et al.*, “SPAC: Serial Protocol for the ATLAS Calorimeter”, ATL-AL-ES-0005 1999.